

**The Low Temperature Oxidation of 2,7-Dimethyloctane  
in a Pressurized Flow Reactor**

A Thesis

Submitted to the Faculty

of

Drexel University

by

Farinaz Farid

in partial fulfillment of the  
requirements for the degree

of

Doctor of Philosophy

November 2015



© Copyright 2015

Farinaz Farid. All Rights Reserved.

## **Dedications**

This work is dedicated to my parents.

## Acknowledgements

First and foremost, I would like to express my sincere appreciation and gratitude to my advisors, Dr. Nicholas P. Cernansky and Dr. David L. Miller, for their tremendous support, constant encouragement and valuable guidance during my PhD studies. This work would have not been possible without their generous contributions on many levels.

I would like to give special thanks to my lab mate, Julius Corrubia, for his significant contributions to the experimental work. I would also like to express my sincere appreciation to Michael Stichter and Yulei Li for all of their help and support. I want to thank Dr. Alan C. W. Lau for all of his guidance throughout my years at Drexel.

My sincere thanks and appreciation goes to my parents, Guita and Farhad, for their unconditional love and support. I would like to highly thank my sister, Farnoush, for bringing the much needed laughter and joy to my graduate student life and for always being there for me. I would like to thank my wonderful grandmother, Mahbanoo, for her love and encouragement. Last, but not least, I would like to thank my dearest aunt and uncle, Fariba and Geoff, for always keeping me positive and being there for me.

I would like to acknowledge the Air Force Office of Scientific Research for their greatly appreciated funding under Grant Numbers FA9550-08-1-0040 and FA9550-11-1-0217.

## Table of Contents

LIST OF TABLES .....	vii
LIST OF FIGURES .....	viii
ABSTRACT.....	xiii
CHAPTER 1 : INTRODUCTION.....	1
1.1 Motivation .....	1
1.2 Objectives.....	2
1.3 Approach .....	3
CHAPTER 2 : LITERATURE REVIEW .....	6
2.1 Introduction .....	6
2.2 Branched Alkane Component of Real Fuels .....	8
2.3 Previous studies on lightly branched Alkane Component of Real Fuels .....	10
2.4 Closure .....	12
CHAPTER 3 : EXPERIMENTAL SETUP AND METHODOLOGIES.....	13
3.1 Introduction .....	13
3.2 The Pressurized Flow Reactor Facility .....	13
3.3 Pressurized Flow Reactor Experimental Methodologies .....	16
3.3.1 Oxidation Experiments Methodology .....	16
3.3.2 Pyrolysis Experiments Methodology.....	18
3.3 Closure .....	20
CHAPTER 4 : CHEMICAL KINETIC MODELS USED FOR COMPARATIVE ANALYSIS OF EXPERIMENTAL DATA.....	21
4.1 Introduction .....	21
4.2 Chemical Kinetic Models Used for Validation Against Experimental Data .....	22

4.2.1 The Lawrence Livermore National Laboratory Mechanism .....	22
4.2.2 The JetSurf v 1.0 Model and the Optimized JetSurf Model .....	24
4.2.3 The Li <i>et al.</i> Model for 2,7-Dimethyloctane .....	25
4.3 The Simulation of Chemical Kinetic Models and Post-Processing of Results in CHEMKIN-PRO Software.....	28
4.4 Closure .....	30
CHAPTER 5 : LOW-TEMPERATURE OXIDATION OF 2,7-DIMETHYLOCTANE AND <i>N</i> -DECANE.....	
5.1 Introduction .....	32
5.2 Experimental Conditions.....	33
5.3 Experimental Results.....	34
5.3.1 Oxidation of 2,7-Dimethyloctane .....	34
5.3.2 Oxidation of <i>n</i> -Decane and Comparisons with 2,7-Dimethyloctane.....	41
5.4 Details of the Model Calculations .....	44
5.5 Modeling Results and Comparison with Experiments .....	46
5.6 Initial Comparison of and Updated 2,7-Dimethyloctane Model with the PFR Data .....	68
5.7 Closure .....	77
CHAPTER 6 : THE PYROLYSIS OF <i>N</i> -DECANE OVER THE TEMPERATURE RANGE OF 850 – 1000 K.....	
6.1 Introduction .....	80
6.2 Experimental Conditions.....	83
6.3 Experimental Results.....	84
6.4 Details of the Model Calculations.....	86
6.4 Modeling Results, Comparisons with Experiments, and Discussion.....	87
6.5 Closure .....	105

CHAPTER 7 : CONCLUDING REMARKS AND RECOMMENFATIONS FOR FUTURE WORK.....	108
LIST OF REFERENCES .....	112
APPENDIX A: PFR FACILITY UPGRADES, MAINTENANCE, AND TROUBLESHOOTING.....	119
Appendix A.1 MS Operating Parameters, GC Method Temperature Program, Maintenance and Replacement of Parts for the GC/MS/FID System and Associated Equipment.....	119
Appendix A.2 Calibration and Replacement of Parts for the Ultramat 23 Gas Analyzer .....	125
Appendix A.3 The Modeling Computer Upgrade and Troubleshooting of Several Common CHEMKIN-PRO Errors .....	127
VITA.....	129

**LIST OF TABLES**

Table 5-1: Test conditions for 2,7-DMO oxidation, residence time $120 \pm 10$ ms.....	33
Table 5-2: List of species identified and their quantified values, determined by the average of three 2,7-DMO experiments at nearly identical conditions with uncertainties being $\pm 1$ standard deviation.....	40
Table 5-3: The notation used in Li <i>et al.</i> model for several key species. ....	46
Table 6-1: Test conditions for <i>n</i> -decane pyrolysis, residence time $168 \pm 10$ ms.....	84
Table 6-2: Speciation of the stable intermediated from <i>n</i> -decane pyrolysis at 1000 K; pressure 8 atm, residence time $168 \pm 10$ ms, initial fuel molar fraction $856 \pm 39$ ppm. ....	85
Table A- 1: GC temperature ramping profile and column carrier gas flow .....	120
Table A- 2: GC/MS/FID field service visits from November 2010 to November 2015.	122



## LIST OF FIGURES

Figure 2-1: Constituents of JP-8, S-8, and Camelina Hydro-Treated Jet Fuels.....	9
Figure 3-1: The schematic of the pressurized flow reactor (PFR) facility. ....	16
Figure 3-2: The effect of residence time on formation of C <sub>2</sub> – C <sub>6</sub> alkenes during the pyrolysis of <i>n</i> -decane at 1000 K and 8 atm.....	20
Figure 5-1: Reactivity and 2,7-DMO profiles for replicate oxidation experiments; 8 atm; 120 ms; average initial fuel fraction 843 ± 13 ppm. CO <sub>2</sub> not recorded during Expt 1. Uncertainties: ± 25 ppm for CO and CO <sub>2</sub> ; ± 1250 ppm for O <sub>2</sub> . ....	38
Figure 5-2: Class analysis for 2,7-DMO oxidation. The classes shown account for ≥ 1% of total carbon input. ....	38
Figure 5-3: Major C <sub>2</sub> -C <sub>7</sub> alkenes produced during the oxidation of 2,7-DMO. ....	39
Figure 5-4: Major aldehydes produced during the oxidation of 2,7-DMO.....	39
Figure 5-5: Fuel, CO, and O <sub>2</sub> profiles during <i>n</i> -decane oxidation; 8 atm; 120 ms; initial fuel fraction 592 ± 19 ppm. CO <sub>2</sub> not recorded during the experiment. Experimental uncertainties: ± 25 ppm for CO and ± 1250 ppm for O <sub>2</sub> . ....	43
Figure 5-6: Carbon fraction for CO during the oxidation of <i>n</i> -decane and the average carbon fraction for CO during the replicate oxidation runs with 2,7-DMO. .	43
Figure 5-7: Predicted molar fraction of major alkenes produced during the oxidation of <i>n</i> -decane vs. measured alkenes at 715 K sample temperature; Model: LLNL 2011; 592 ppm initial <i>n</i> -decane molar fraction; residence time 120 ms, pressure 8 atm. ....	44
Figure 5-8: Labeling of carbon sites in the structure of 2,7-DMO. ....	45
Figure 5-9: CO and CO <sub>2</sub> during the oxidation of 2,7-DMO: experiments versus the computations of Li <i>et al.</i> model. For simulations, the averaged reactants' composition of 843 ppm 2,7-DMO / 42,100 ppm O <sub>2</sub> / 957,057 ppm N <sub>2</sub> was used. ....	47
Figure 5-10: Molar fraction of 2,7-DMO during the oxidation run: Averaged data from three replicate experiments vs. the predictions of Li <i>et al.</i> model. ....	47

Figure 5-11: Molar fraction of C <sub>2</sub> -C <sub>4</sub> alkenes produced during the oxidation of 2,7-DMO: Averaged data from three replicate experiments vs. the predictions of Li <i>et al.</i> Model.....	49
Figure 5-12: Molar fraction of 3-methyl-1-butene produced during the oxidation of 2,7-DMO: Averaged experimental data vs. the predictions of Li <i>et al.</i> model.....	50
Figure 5-13: Molar fraction of formaldehyde and acetaldehyde produced during the oxidation of 2,7-DMO: Averaged data from three replicate experiments vs. the predictions of Li <i>et al.</i> model.....	50
Figure 5-14: Molar fraction of acetone produced during the oxidation of 2,7-DMO: Averaged data from replicate experiments vs. the predictions of Li <i>et al.</i> model.....	51
Figure 5-15: Normalized Rates of Production for reactions affecting the molar fraction of CO at selected inlet temperatures: Li <i>et al.</i> model for 2,7-DMO. ....	53
Figure 5-16: Normalized Rates of Production for reactions affecting the molar fraction of CO <sub>2</sub> at selected inlet temperatures: Li <i>et al.</i> model for 2,7-DMO. ....	54
Figure 5-17: Normalized Rates of Production for reactions affecting the molar fraction of ethene at selected inlet temperatures: Li <i>et al.</i> model for 2,7-DMO.....	56
Figure 5-18: Normalized Rates of Production for reactions affecting the molar fraction of propene at selected inlet temperatures: Li <i>et al.</i> model for 2,7-DMO. ....	57
Figure 5-19: Normalized Rates of Production for reactions affecting the molar fraction of <i>iso</i> -butene at selected inlet temperatures: Li <i>et al.</i> model for 2,7-DMO. ....	58
Figure 5-20: Normalized Rates of Production for reactions affecting the molar fraction of 2-butene at selected inlet temperatures: Li <i>et al.</i> model for 2,7-DMO.....	59
Figure 5-21: Reaction flux analysis for 2,7-DMO oxidation with an emphasis on reactions leading to the formation of iC <sub>5</sub> H <sub>11</sub> COCH <sub>2</sub> radical and acetone; Li <i>et al.</i> model, inlet temperature 670 K, pressure 8 atm, residence time 120 ms.....	62
Figure 5-22: Reaction flux during 2,7-DMO oxidation with an emphasis on reactions leading from iC <sub>5</sub> H <sub>11</sub> COCH <sub>2</sub> to CO, CO <sub>2</sub> , formaldehyde, acetaldehyde; Li <i>et al.</i> model, inlet temperature 670 K, pressure 8 atm, residence time 120 ms.....	63
Figure 5-23: The most sensitive reactions with respect to CO <sub>2</sub> ; inlet temperature 680 K; pressure 8 atm, residence time 120 ms; Li <i>et al.</i> model.....	64

- Figure 5-24: Sensitive reactions with respect to ethene at inlet temperatures of 680 K and 750 K; pressure 8 atm, residence time 120 ms; Li *et al.* model..... 66
- Figure 5-25: Normalized A-factor sensitivities for the most sensitive reactions with respect to propene at inlet temperature of 680 K and 750 K; pressure 8 atm, residence time 120 ms; Li *et al.* model for 2,7-DMO..... 67
- Figure 5-26: CO and CO<sub>2</sub> profiles during the oxidation of 2,7-DMO: Experiment, Li *et al.* model, and modified Li *et al.* model. .... 72
- Figure 5-27: Molar fraction of 2,7-DMO during the oxidation run: Averaged data from three replicate experiments vs. the predictions of the original as well as the modified Li *et al.* model..... 73
- Figure 5-28: C<sub>2</sub>-C<sub>4</sub> alkene intermediates profiles during the oxidation of 2,7-DMO: Experiment, Li *et al.* model, and modified Li *et al.* model..... 74
- Figure 5-29: Molar fraction of 3-methyl-1-butene produced during the oxidation of 2,7-DMO: Experiment, Li *et al.* model, and modified Li *et al.* model..... 75
- Figure 5-30: Molar fractions of formaldehyde and acetaldehyde during the oxidation of 2,7-DMO: Experiment, Li *et al.* model, and modified Li *et al.* model..... 76
- Figure 5-31: Molar fraction of 2,7-DMO during the oxidation run: Averaged data from three replicate experiments vs. the predictions of the original as well as the modified Li *et al.* model..... 77
- Figure 6-1: Demonstration of high-pressure limit (i.e. no dependence on pressure) for a sample pyrolysis run with *n*-dodecane using LLNL 2011 model; plug flow reactor module; initial fuel mole fraction 800 ppm, residence time 90 ms. .. 81
- Figure 6-2: Demonstration of the effect of water addition to reactants' mixture on enhancing the rate of fuel decomposition for an example pyrolysis run with *n*-dodecane using the Optimized JetSurf model; homogeneous batch reactor module..... 82
- Figure 6-3: Major species from *n*-decane pyrolysis over the temperature range of 850 – 1000 K; pressure 8 atm, residence time 168 ± 10 ms, initial fuel mole fraction 990 ± 46 ppm. .... 86
- Figure 6-4: Carbon fractions for major species measured during the pyrolysis of *n*-decane: experiment vs. models; temperature range 850 – 1000 K; pressure 8 atm, residence time 168 ms, initial fuel molar fraction 990 ppm. .... 89
- Figure 6-5: ROP of *n*-decane at select inlet temperatures under pyrolysis conditions;

pressure 8 atm, residence time 168 ms, initial fuel molar fraction 990 ppm, LLNL 2011. ....	90
Figure 6-6: ROP of <i>n</i> -decane at select inlet temperatures under pyrolysis conditions; pressure 8 atm, residence time 168 ms, initial fuel molar fraction 990 ppm, JetSurf v 1.0. ....	91
Figure 6-7: ROP of <i>n</i> -decane at select inlet temperatures under pyrolysis conditions; pressure 8 atm, residence time 168 ms, initial fuel molar fraction 990 ppm, Optimized JetSurf. ....	92
Figure 6-8: The change of log (K) with temperature for hydrogen mediated H-abstraction from <i>n</i> -decane to produce 2-decyl radical. Model: JetSurf v 1.0.....	93
Figure 6-9: Normalized A-factor sensitivities for significant reactions affecting the molar fraction of <i>n</i> -decane at inlet temperature of 1000 K; pressure 8 atm, residence time 168 ms, and initial fuel molar fraction 990 ppm. Model: LLNL 2011..	97
Figure 6-10: Normalized A- factor sensitivities for significant reactions affecting the molar fraction of <i>n</i> -decane at inlet temperature of 1000 K; pressure 8 atm, residence time 168 ms, and initial fuel molar fraction 990 ppm. Model: JetSurf v1.0. ....	97
Figure 6-11: Normalized A- factor sensitivities for significant reactions affecting the molar fraction of <i>n</i> -decane at inlet temperature of 1000 K; pressure 8 atm, residence time 168 ms, and initial fuel molar fraction 990 ppm. Model: Optimized JetSurf. ....	98
Figure 6-12: ROP of ethene at select inlet temperatures under pyrolysis conditions; pressure 8 atm, residence time 168 ms, initial <i>n</i> -decane molar fraction 990 ppm, LLNL 2011 model. ....	99
Figure 6-13: ROP of ethene at select inlet temperatures under pyrolysis conditions; pressure 8 atm, residence time 168 ms, initial <i>n</i> -decane molar fraction 990 ppm, JetSurf v 1.0 model. ....	100
Figure 6-14: ROP of ethene at select inlet temperatures under pyrolysis conditions; pressure 8 atm, residence time 168 ms, initial <i>n</i> -decane molar fraction 990 ppm, Optimized JetSurf model. ....	101
Figure 6-15: Reaction flux analysis for <i>n</i> -decane pyrolysis at 1000 K with an emphasis on reactions leading to the formation of ethene; LLNL 2011 model, pressure 8 atm, residence time 168 ms.....	102

- Figure 6-16: Normalized A-factor sensitivities for significant reactions affecting the molar fraction of ethene at inlet temperature of 1000 K; pressure 8 atm, residence time 168 ms, and initial *n*-decane molar fraction 990 ppm. Model: LLNL 2011. .... 104
- Figure 6-17: Normalized A-factor sensitivities for significant reactions affecting the molar fraction of ethene at inlet temperature of 1000 K; pressure 8 atm, residence time 168 ms, and initial *n*-decane molar fraction 990 ppm. Model: JetSurf v1.0. .... 104
- Figure 6-18: Normalized A-factor sensitivities for significant reactions affecting the molar fraction of ethene at inlet temperature of 1000 K; pressure 8 atm, residence time 168 ms, and initial *n*-decane molar fraction 990 ppm. .... 105
- Figure A- 1: MS operating parameters according to a sample tune report. .... 121

**ABSTRACT**

The Low Temperature Oxidation of 2,7-Dimethyloctane in a Pressurized Flow Reactor

Farinaz Farid

Dr. Nicholas P. Cernansky and Dr. David L. Miller

The complexity of real fuels has fostered the use of simple mixtures of hydrocarbons whose combustion behavior approximates that of real fuels in both experimental and computational studies to develop models of the combustion of the real fuel. These simple mixtures have been called surrogates. Lightly branched paraffins are an important class of constituents in gasoline, diesel and aviation turbine fuels and therefore are primary candidates for use as a component in a surrogate. Unfortunately, fundamental studies on combustion characteristics of high molecular weight mono- and di-methylated iso-paraffins are scarce. Therefore, this study was designed to investigate the low-temperature oxidation of 2,7-dimethyloctane (2,7-DMO) ( $C_{10}H_{22}$ ), a lightly branched isomer of decane.

Replicate 2,7-DMO oxidation experiments were conducted in a pressurized flow reactor (PFR) over the temperature range of 550 – 850 K, at a pressure of 8 atm and an equivalence ratio of 0.3 in 4.21% oxygen / nitrogen. The reactivity was mapped by continuous monitoring of CO, CO<sub>2</sub>, and O<sub>2</sub> using a non-dispersive infrared (NDIR) carbon monoxide / carbon dioxide analyzer and an electrochemical oxygen sensor. For examining the underlying reaction chemistry, detailed speciation of samples was performed at selected temperatures using a gas chromatograph with a flame ionization detector coupled to a mass spectrometer. Comparable oxidation experiments for *n*-decane were carried out to examine the unique effects of branching on fuel reactivity and distribution of major stable intermediates. For both isomers, the onset of negative temperature coefficient (NTC) region was observed near 700 K, with the reactivity decreasing with increasing the temperature. The flow reactor study of *n*-decane oxidation confirmed that the isomerization reduces the amount of CO produced at peak reactivity. In addition to reaction inhibition, branching affected the distribution of C<sub>2</sub>-C<sub>4</sub> olefin intermediates. While the oxidation of *n*-decane

resulted primarily in the formation of ethene near the NTC start, propene and isobutene were the major olefins produced from 2,7-DMO. A comparative analysis of experimental data with respect to a detailed chemical kinetic model for 2,7-DMO was performed and discrepancies were noted. Based on these results, a collaborative effort with Dr. Charles Westbrook (Lawrence Livermore National Laboratory) was initiated to refine the model predictions in the low temperature and NTC regimes. The effort resulted in an updated version of the 2,7-DMO mechanism, improving some of the key features such as calculated CO<sub>2</sub> profile and final yields of *iso*-butene over the studied range of temperature.

Fuel pyrolysis in the intermediate temperature regime, 850 – 1000 K, also was investigated for the first time in the PFR facility. However, preliminary *n*-decane experiments measured only a small amount of fuel decomposition, indicating that higher temperature operation would be beneficial. The major species produced from *n*-decane decomposition, in descending order of molar fraction, were ethene, propene, and 1-butene. These results were compared with the predictions of two existing chemical kinetic models and the sources of variations between the experiments and the models as well as among the mechanisms were investigated. At 1000 K, the mechanisms predicted higher levels of fuel depletion and ethene production. Also, while the mechanisms were similar in their predicted pathways for fuel depletion and formation of ethene, inconsistencies were observed in relative contribution of these pathways to the final yields as well as the rate parameter determination for several sensitive reactions with respect to *n*-decane and ethene.

Overall, the research aided in achieving a data set quantifying the oxidation characteristics of 2,7-DMO (and *n*-decane for comparison) as well as an elucidation of critical reaction pathways based on experimental results. Preliminary pyrolysis experiments were carried out using *n*-decane and the limitations on companion 2,7-DMO pyrolysis experiments were established. The data was compared with the predictions of several chemical kinetic mechanisms and, using tools such as rate of production analysis and sensitivity analysis, the sources of deviations from experimental

data as well as possible areas of improvement were identified. The findings from 2,7-DMO study was directly used to refine an existing chemical kinetic model for 2,7-DMO, in line with the ultimate goal of feeding the much needed experimental database for validation and refinement of kinetic models of jet fuel surrogates.





## CHAPTER 1 : INTRODUCTION

### 1.1 Motivation

The United States Department of Defense (DoD) Directive 4140.25 mandates JP-8 as the primary fuel to be used by military land-based, air and ground forces in all theaters of operation [1]. In addition, DoD is seeking to expand its feedstock options by adopting an alternative fuel initiative to test and certify kerosene-type non-petroleum jet fuel candidates that can be feasibly used as “drop-in” replacements for conventional petroleum-derived JP-8 (e.g., see [2-7]). Lastly, much attention is given to new combustion modes such as diesel low-temperature combustion (LTC) where the suppression of local combustion temperatures and premixing fuel with the in-cylinder charge before ignition allow for reduced emissions of nitrogen oxides (NO<sub>x</sub>) and particulate matter (soot) [8, 9].

Alternative combustion modes are typically associated with low-temperature chemistry where the high-temperature reaction mechanisms normally employed are not adequate for simulation of combustion and emission behavior. In addition, molecular structure and reactants’ chemical composition have significant influence on ignition chemistry in different temperature regimes. An increasingly important component in the development of optimized engine designs and advanced fuels is computational fluid dynamic modeling of the combustion event which requires appropriate chemical kinetic models. This presents unique challenges, in part since real fuels contain hundreds to thousands of distinct hydrocarbon components in a diverse range of carbon numbers (C<sub>9</sub>-C<sub>16</sub>) and chemical classes (from *n*-, *iso*-, and *cyclo*- paraffins to aromatics). This

complexity has fostered the concept of using surrogate fuels to develop chemical kinetic models to accurately predict the oxidation and pyrolysis characteristics of real fuels [10-12]. Surrogates are mixture containing a handful of components, typically 1 – 10, that are formulated to mimic the targeted properties and behavior of the fully blended fuel. In this context, knowledge of the oxidation and pyrolysis characteristics of representative components of relevant chemical classes is essential to the development of adequate chemical kinetic models for combustion simulations.

Branched paraffins are an important chemical class in gasoline, diesel and aviation turbine fuels from both fossil-derived and synthetic sources. The *iso*-paraffins in typical fuels have carbon numbers of 10 –14; In addition, measurements have shown that most of the identified jet fuel *iso*-paraffins are either mono- or di-methylated [11]. Unfortunately, fundamental studies on combustion characteristics of high molecular weight mono- and di-methylated *iso*-paraffins are scarce. Previous studies have been primarily focused on combustion properties of heavily branched primary reference fuels (PRFs) and C<sub>4</sub>-C<sub>7</sub> paraffin isomers (see [13-20] for sample studies), with C<sub>8</sub> paraffin isomers receiving attention in recent years (e.g., [21-24]). A review paper by Pitz and Mueller [25] regarding the development of diesel surrogate fuels identifies the considerable gap in combustion knowledge for large (i.e. C<sub>8</sub> and greater) lightly branched *iso*-paraffins and recommends the inclusion of these components in models and experimental investigations.

## 1.2 Objectives

The first objective of this study was to investigate the low-temperature ( $T < 850$  K) oxidation of 2,7-dimethyloctane (2,7-DMO) (C<sub>10</sub>H<sub>22</sub>), a representative of lightly branched

*iso*-paraffin component of jet fuel surrogates. The second objective was to examine the effect of isomerization on fuel reactivity through a study of the oxidation of *n*-decane, the straight chain analog of 2,7-DMO, at comparable conditions. As a component of the ultimate goal to validate and refine the chemical kinetic models for fuel combustion, the third objective was to use the experimental data as a benchmark to refine the low-temperature chemistry pathways of an existing detailed chemical kinetic model for 2,7-DMO. Finally, the last objective was to explore, for the first time, the capabilities of the facility to perform experiments under pyrolysis conditions and in the intermediate temperature regime ( $T > 900$  K).

### 1.3 Approach

In this study, the pressurized flow reactor (PFR) at Drexel University was used to examine the oxidation of 2,7-DMO over the temperature range of 550-850 K, at a pressure of 8 atm and a lean equivalence ratio of 0.3 in 4.2% oxygen/nitrogen. Fuel reactivity was mapped by continuous monitoring of carbon monoxide (CO), carbon dioxide (CO<sub>2</sub>) and oxygen (O<sub>2</sub>). Detailed speciation of collected samples was performed at selected temperatures. Furthermore, oxidation data for *n*-decane in the same flow reactor facility at a comparable experimental condition was used to identify the unique effects of branching on fuel reactivity, the onset of NTC region, and distribution of some key stable intermediates. Fuel pyrolysis in the intermediate temperature regime, 850-1000 K, also was investigated for the first time in the PFR facility. Specifically, the completed research achievements are divided into the following parts:

1. Investigate the oxidation of 2,7-DMO in the low temperature and Negative Temperature Coefficient (NTC) regime (Chapter 5, Section 5.3.1). The sub-tasks

- included: a) performing three replicate oxidation experiments with 2,7-DMO over the temperature range of 550 – 850 K, b) mapping fuel reactivity by continuous monitoring of CO, CO<sub>2</sub> and O<sub>2</sub>, and c) conducting detail speciation of stable intermediates extracted at five selected temperatures throughout the studied temperature range. For this purpose, a gas chromatograph (GC) coupled to a flame ionization detector (FID) and a mass spectrometer (MS) was used.
2. Examine the unique effects of isomerization on fuel reactivity and distribution of some key stable intermediates near peak reactivity (Chapter 5, Section 5.3.2). The sub-tasks included: a) Comparing the reactivity data for 2,7-DMO to those of *n*-decane, the straight-chain analog, at comparable experimental conditions, and b) evaluating features such as fuel conversion and distribution of C<sub>2</sub> – C<sub>4</sub> alkenes for straight-chain structure by analysis of a sample collected near peak reactivity (i.e. at 715 K) during the oxidation of *n*-decane.
  3. Compare the PFR data with an existing chemical kinetic model for 2,7-DMO. Use the findings to collaborate with model developers to refine the model details for low-temperature oxidation chemistry.
  4. Perform a comparative analysis of experimental data with respect to an available chemical kinetic model for 2,7-DMO (Chapter 5, Section 5.5). The sub-tasks included: a) Comparing the predictions Li *et al.* model [26] for 2,7-DMO with the PFR oxidation data and identifying the discrepancies, b) Performing analysis of model details for the low-temperature chemistry to identify inter-workings of the model, and c) highlighting possible areas for model improvement based on the experimental measurements.

5. Initiate a collaborative effort with Dr. Charles Westbrook (Lawrence Livermore National Laboratory) to refine the low-temperature reaction classes in the Li *et al.* model (Chapter 5, Section 5.6). The sub-tasks included: a) Supplying the PFR data and modeling analysis to Dr. Westbrook, b) Performing an extensive refinement to the majority of low-temperature reaction classes as well as tuning the model predictions for CO<sub>2</sub> levels (done by Dr. Westbrook), c) Comparing the PFR data for 2,7-DMO with calculations of the modified Li *et al.* mechanism, and d) identifying the improvements as well as some additional areas for further model refinement.
6. Investigate, for the first time in this experimental facility, fuel pyrolysis in the intermediate temperature regime (Chapter 6, Section 6.3). The sub-tasks included: a) Establishing the currently maximum achievable temperature and residence time with the PFR, b) Performing preliminary investigation of *n*-decane pyrolysis over the temperature range of 850 – 1000 K, and c) Identifying the extent of fuel depletion as well as distribution of pyrolysis products at 1000 K, using the GC-MS-FID.
7. Compare the experimental data with predictions of two existing detailed chemical kinetic models for *n*-decane pyrolysis and analyze the discrepancies (Chapter 6, Section 6.4). The sub-tasks included: a) Comparing PFR data with predictions of the Lawrence Livermore National Laboratory (LLNL) model by Sarathy *et al.* [21] as well as two variations of JetSurf mechanism (Sirjean *et al.* [27] and Banerjee *et al.* [28]) and b) investigating the possible sources of variations between the experiments and the models as well as among the mechanisms.

## CHAPTER 2 : LITERATURE REVIEW

### 2.1 Introduction

The foundation of modern interpretation of hydrocarbon oxidation is based on acceptance of free radicals, followed by the Semenov theory of chain reactions [29]. Essentially, the associated chemical reactions are categorized into the following types [29]:

- 1) Primary initiation reaction which involves the formation of radicals from parent molecules
- 2) Chain propagation reactions in which the number of radicals doesn't change
- 3) Chain termination reactions which involve the removal of radicals
- 4) Branching reactions in which the number of radical products is more than the number of radical reactants
- 5) Secondary initiation (or degenerate branching) reactions, where new radicals are formed from a stable intermediate species.

The number and type of radicals formed during combustion reactions are largely a function of temperature. It is therefore, a common practice to divide the regimes of hydrocarbon combustion into distinct temperature regimes. Each temperature regime is dominated by different radicals and consequently, by distinct key reaction pathways. It should be noted that the temperature limits shift with pressure; at higher pressures the transition from one temperature regime to another occurs at higher temperatures. The detailed general scheme of hydrocarbon combustion for propane and larger alkanes has been developed through extensive experimental testing and kinetic modeling and is

widely accepted (e.g., see [30-34] ). The low temperature regime is controlled by alkylperoxy radical, denoted by  $\cdot\text{RO}_2$ . Specifically, in the critical pathway for low temperature oxidation, the parent fuel (RH) undergoes hydrogen (H) abstraction to form an alkyl radical ( $\cdot\text{R}$ ). Addition of molecular oxygen ( $\text{O}_2$ ) to alkyl radical will produce the alkylperoxy radical. The alkylperoxy radical can follow a number of possible pathways. The main fate of this radical in the low temperature regime is to go through an internal isomerization to form an alkylhydroperoxy radical,  $\cdot\text{QOOH}$ . The  $\cdot\text{QOOH}$  radical may undergo a cyclization, throwing out an OH molecule and produce a cyclic ether. Alternatively, it may undergo an additional oxygen addition reaction to produce a peroxyalkylhydroperoxy radical,  $\cdot\text{O}_2\text{QOOH}$ . Isomerization of this radical, followed by a subsequent decomposition produces ROOH molecule and hydroxyl (OH). ROOH is a degenerate branching agent whose thermal decomposition is the branching step in the mechanism. The multiplication in the number of radicals and production of OH is needed for the runaway for first-stage ignition. The termination steps which impede this pathway are placed earlier in the mechanism. Specifically, in the higher end of the low temperature regime, instead of following pathways to produce highly reactive radicals, particularly hydroxyl radicals, the reaction proceeds to produce less reactive species including hydroperoxy radicals ( $\cdot\text{HO}_2$ ) and alkenes. This translates into a decrease in reactivity with an increase in the temperature, known as NTC behavior. At even higher temperatures, moving through the NTC region into the intermediate and high temperature regimes, pathways lead from hydroperoxy radical to form two hydroxyl radicals. The turnover to hydroxyl radical control of reactivity and heat release signifies the transition to the high temperature reaction regime and hot ignition.



More detailed description of low temperature combustion chemistry, the target temperature range of present work, is provided in numerous resources (e.g., see [29]). This chapter is focused on providing an overview of previous combustion research related to lightly-branched (i.e. mono- and di-methylated) and heavily-branched alkane component of hydrocarbon fuels. Section 2.2 provides references to some previous studies of heavily branched alkanes, specifically *iso*-octane and *iso*-cetane. In Section 2.3, the previous experimental investigation and model development related to oxidation and pyrolysis of mono- and di-methylated alkanes are discussed. A closure will be presented in Section 2.4.

## **2.2 Branched Alkane Component of Real Fuels**

JP-8 and alternative Jet fuels contain hundreds to thousands of distinct hydrocarbon components in a diverse range of carbon numbers ( $C_9$ - $C_{16}$ ) and chemical classes (from *n*-, *iso*-, and *cyclo*- paraffins to aromatics). Among these classes, alkanes are the dominant class found in JP-8 and synthetic jet fuels (see Figure 2-1). The ratio between straight-chain and branched alkane component varies from one feedstock to another. For example, more than 80 % of S-8 POSF 4734, a synthetic paraffinic jet aviation fuel, is composed of mono- and di-methylated alkanes [35]. Despite the significance of these lightly branched components and the increasingly recognized need for their inclusion in formulation of surrogate blends for real fuels, studies on their combustion characteristics are scarce.

## JP-8 and major alternative jet fuels

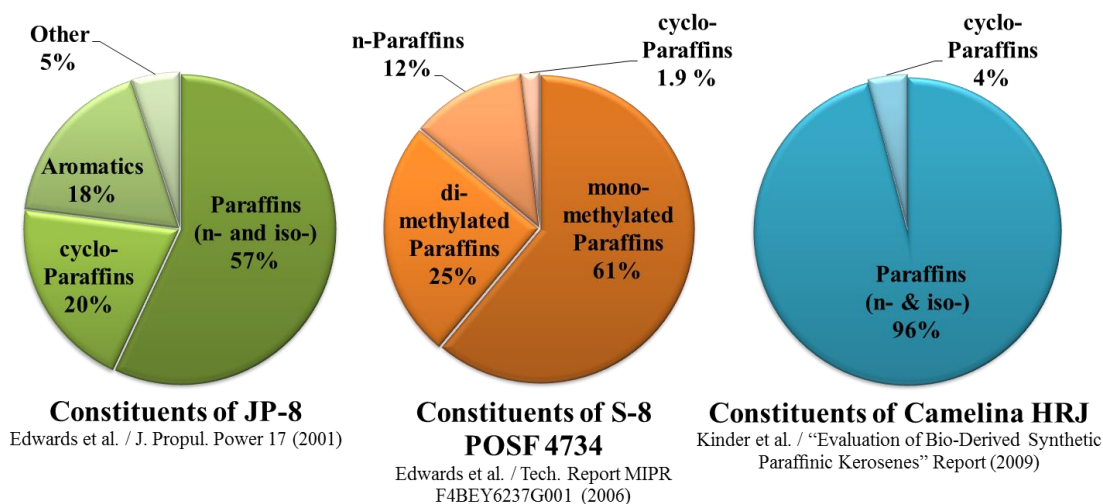


**Figure 2-1: Constituents of JP-8, S-8, and Camelina Hydro-Treated Jet Fuels.**

It must be noted that the cost of producing high purity weakly branched large *iso*-paraffins is high; this constraint alone is an impediment to performing large-scale experimental studies over a wide range of conditions for these compounds. On the other hand, in comparison to the limited studies on high molecular-weight lightly branched *iso*-paraffins, a large body of literature exists on combustion behavior of *iso*-octane (2,2,4-trimethylpentane) (e.g., [36-41]), a primary reference fuel (PRF) for gasoline octane rating and a widely accepted surrogate fuel component (e.g., see [42, 43]). There are also a number of studies on characterizing the combustion properties of *iso*-cetane (2,2,4,4,6,8,8-heptamethylnonane), a PRF for diesel cetane rating (e.g., see [44-47]). While the use of heavily branched *iso*-paraffins in surrogate formulation is more feasible in terms of economic considerations and availability, recent studies increasingly favor the inclusion of large mono- and di-methylated *iso*-paraffins as representative of the *iso*-paraffin component in surrogate formulation to more accurately capture key design characteristics such as volatility and ignition quality [25, 48-50]. The next section will

provide an overview of previous experimental studies and kinetic modeling work on lightly branched alkanes.

### **2.3 Previous studies on lightly branched Alkane Component of Real Fuels**

Previous efforts for investigation and modeling of combustion characteristics of lightly methylated alkanes have been primarily focused on singly-methylated as well as di-methylated C<sub>8</sub> and smaller paraffins (e.g., see [22, 23, 51, 52]). The Lawrence Livermore National Laboratory (LLNL) model by Sarathy *et al.* [21] was developed for oxidation and pyrolysis of 2-methylalkanes from C<sub>7</sub> to C<sub>20</sub> and was comprehensively validated using experimental data from various experimental setups (see Section 4.2.1 for additional details on the mechanism). The authors concluded that the addition of methyl group to the hydrocarbon structure resulted in longer ignition delay times and decreased low-temperature reactivity. To reasonably simulate the effect of methyl branch location and number, the necessity of extending the model to other higher molecular weight lightly branched paraffins (e.g. 3-methylalkanes and di-methylalkanes) was emphasized. Recently, Sarathy *et al.* [24] used the LLNL model for 2-methylalkanes in developing a comprehensive chemical kinetic mechanism for low and high temperature oxidation of 2,5-dimethylhexane (C<sub>8</sub>H<sub>18</sub>) (2,5-DMH). The model was validated using shock tubes, a rapid compression machine and a jet-stirred reactor. The speciation data from jet-stirred reactor indicated that under ideal conditions, the oxidation of di-methylated paraffin produced more propene and *iso*-butene in comparison to mono-methylated alkanes. In addition, the importance of propene chemistry in higher temperatures was demonstrated through production of large quantities of propene during the shock tube ignition delay time measurements of 2,5-DMH.

Very few studies, all of them being recent, have investigated the oxidation and pyrolysis characteristics of 2,7-DMO, a C<sub>10</sub> symmetric di-methylated alkane.

Slavinskaya *et al.* [53] measured the ignition delay of stoichiometric 2,7-DMO / air mixture in a shock tube at a pressure of ~ 16-17 atm and over a temperature range 650 – 1500 K. A detailed chemical kinetic model with a new sub-mechanism for 2,7-DMO, consisting of a high-temperature mechanism and a lumped reaction scheme for the low-temperature chemistry, was used for comparisons with the experimental data. Another study by Liu *et al.* [47] reported on ignition characteristics of several C<sub>8</sub> and C<sub>10</sub> di-methylated paraffins. Using a non-premixed counter-flow flame configuration, Liu *et al.* measured the ignition temperatures of atmospheric flames of octane (C<sub>8</sub>) and decane (C<sub>10</sub>) isomers, where decane isomers included *n*-decane and 2,7-DMO. The study concluded that increasing the degree of fuel branching decreases the reactivity and inhibits the ignition. In addition, it was shown that increasing the branching notably increases the concentration of *iso*-butene, a major intermediate during the oxidation of branched isomers and known to be remarkably stable. To simulate the experimental data, a high-temperature model consisting of 826 species and 4725 reactions was developed based on the high-temperature oxidation model for 2,5-DMH by Sarathy *et al.* [23], supplemented by sub-mechanisms for *n*-nonane, *n*-decane, and 2-methyloctane [21] and with new pathways added for 2,6-dimethylheptane and 2,7-DMO. The model predictions were in good agreement with the ignition temperature data. Li *et al.* [26] measured the shock tube ignition delay time of 2,7-DMO over the temperature range 666 – 1216 K, pressure range 12 – 27 atm, and equivalence ratios of 0.5 and 1. In addition, the fuel and C<sub>2</sub>H<sub>4</sub> species time histories data were recorded for pyrolysis of 2000 ppm 2,7-DMO,

diluted in argon, over the temperature range 1126 K – 1455 K and at pressures near 16 and 35 atm. A novel comprehensive detailed chemical kinetic model for 2,7-DMO was developed to simulate the experimental data. Some of its features included refinements to the high-temperature model used by Liu *et al.* for 2,7-DMO [47] as well as addition of a new low-temperature kinetic scheme. The model is described in more details in Section 4.2.3. Comparisons between the mechanism and the experimental data indicated that the model was successful in qualitative prediction of trends over the tested range of conditions. However, the model's deficiency in predicting ignition delay times under lean conditions and intermediate temperatures suggested the need for additional investigation of aspects such as important reaction pathways as well as the accuracy of thermochemistry values of important radicals pertinent to low-temperature and NTC regimes.

## 2.4 Closure

This chapter provided an overview of the importance of lightly branched alkanes, as a major component of real fuels. In addition, a brief overview of previous and ongoing combustion research and modeling efforts related to heavily branched alkanes, C<sub>8</sub> and smaller lightly branched alkanes, and C<sub>10</sub> di-methylated alkanes was provided. In general, prior studies on oxidation of C<sub>10</sub> and larger di-methylated alkanes are scarce, signifying the need for expanding the database for branched alkanes to longer carbon chain lengths. The primary focus of this study, therefore, was to provide high-quality data for the oxidation of 2,7-DMO, a symmetric di-methylated isomer of decane, in the low temperature and NTC regimes using the Drexel pressurized flow reactor. The next chapter will describe the experimental facility and methodologies in details.

## CHAPTER 3 : EXPERIMENTAL SETUP AND METHODOLOGIES

### 3.1 Introduction

In this chapter, the Drexel pressurized flow reactor (PFR) facility, the chemical analysis protocols, and experimental methods are explained. The PFR was the primary apparatus used to examine the oxidation and pyrolysis reactions of the target hydrocarbon components. The progress of these reactions was measured with gas analysis instrumentation consisting of a gas chromatograph (GC) with a flame ionization detector (FID) coupled to a mass spectrometer (MS). For oxidation studies, the chemical reactivity was continuously mapped using an online non-dispersive infrared (NDIR) gas analyzer for continuous carbon monoxide (CO) and carbon dioxide (CO<sub>2</sub>) measurements and an electrochemical cell for molecular oxygen (O<sub>2</sub>) measurements. Section 3.2 describes the PFR facility and the analytical instruments. While the overall experimental set up and the operating procedure remained the same for both pyrolysis and oxidation studies, some parameters such as maximum reaction temperature and residence time differ between the two. These differences as well as the experimental methodologies are described in Section 3.2. A closure to this chapter is presented in Section 3.3.

### 3.2 The Pressurized Flow Reactor Facility

Figure 3-1 shows a schematic of the experimental equipment and setup. Detailed description of the facility, PFR design, system characterization, analytical instrumentation, sample collection, and sample analysis can be found elsewhere (e.g., see [54-56]); the following provides a summary of the important characteristics of the PFR and the analytical instruments as well as a highlight of the sample collection and analysis

procedures. The PFR is a tubular turbulent flow reactor developed to study the chemistry of hydrocarbon oxidation (and recently to examine the pyrolysis conditions) at temperatures up to 1000 K and pressures up to 20 atm (2.0 MPa), with relative isolation from fluid mechanics and large temperature gradients. The reaction chamber inside the PFR consists of a 2.2 cm ID, 40 cm long quartz reactor tube, contained within a stainless steel pressure vessel. The volume between the quartz reactor tube and the pressure vessel forms an annulus that is at the same pressure as the reaction chamber.

An upgrade to the system included the installation of four Alicat Scientific mass flow controllers (MFC) which replaced the previously used Porter MFCs. The upgrade aimed to reduce the experimental uncertainty in the measurements by providing more accurate control. The Alicat Scientific MFCs offer a high accuracy calibration option of 0.4% of reading  $\pm$  0.2% of full scale. It should be, however, noted that while the reactor itself can withstand pressures as high as 20 atm, the higher pressure limit is currently constrained by the maximum pressure of the MFC units, 9.86 atm.

For measurement of intermediate species that are produced from the reactions, two primary instrumentations were used. CO, CO<sub>2</sub>, and O<sub>2</sub> were measured continuously, using Siemens Ultramat 23 gas analyzers. The uncertainty in measurements of CO and CO<sub>2</sub> was  $\pm$  25 ppm and the uncertainty in O<sub>2</sub> measurements was  $\pm$  1250 ppm. The gas analyzer was calibrated prior to each oxidation experiment. The instructions on how to calibrate the gas analyzer as well information on the replaced components (i.e. the electrochemical O<sub>2</sub> sensor and the pump) during the course of this research can be found in Appendix A.1. The identification and quantification of other stable intermediates was performed using a Thermo Finnigan TraceGC gas chromatograph with flame ionization

detection (GC/FID) and the gas chromatograph coupled to a Thermo Finnigan TraceDSQ mass spectrometer (GC/MS). All product documentation can be found from <http://gc-gcms-customersupport.com/> (listed under product names: “TRACE GC/ULTRA” and “DSQ SERIES”), the product support webpage that is provided by Thermo Fisher Scientific. Additional information on maintenance and replacement of parts for the GC/MS/FID and its associated software and computer can be found in Appendix A.2. The appendix also includes information on the GC program method with associated temperature ramping profile that was used to separate the gas sample components.

The GC is equipped with a 100-m polydimethylsiloxane-based capillary column (Sigma Aldrich Petrocol DH, 0.25 mm ID, 0.5  $\mu\text{m}$  film thickness) with a carrier gas flow of helium. The flow is split between the MS and FID after the capillary column using an SGE Analytical Science MS/FID Splitter kit with a restrictor set for 0.25mm ID columns. For identification of species, NIST/EPA/NIH Mass Spectral Library (version 2.0 f) was used. Where calibration standards were available, GC retention time matching was used for supplementary identification. Quantification of species was primarily performed using the FID. Calibration curves were established with standards of gas-phase hydrocarbons at 15, 100, and 1000 ppm. When a calibration standard was not available for a particular compound, the species was quantified with correction factors of FID signal for a similar molecule [57]. Formaldehyde was identified with the MS. The linear relationship observed between the MS and FID signals for acetaldehyde was used to determine a theoretical formaldehyde FID signal from the formaldehyde MS signal [58].



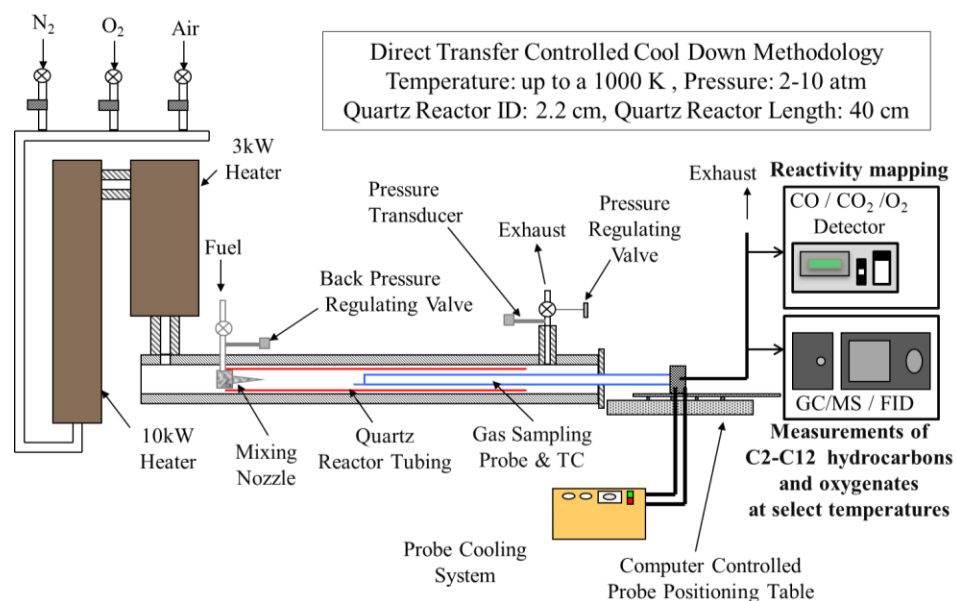


**Figure 3-1: The schematic of the pressurized flow reactor (PFR) facility.**

### 3.3 Pressurized Flow Reactor Experimental Methodologies

The PFR facility was used to perform the oxidation and pyrolysis experiments. Section 3.3.1 describes the general procedure for an oxidation experiment. Section 3.3.2 describes the pyrolysis experiments and highlights the differences between an oxidation and a pyrolysis run.

#### 3.3.1 Oxidation Experiments Methodology

Nitrogen (purity = 99.9%, Airgas) and oxygen (purity = 99.994%, Airgas) are mixed to produce synthetic, contaminant-free air. This synthetic air is heated to the maximum desired reaction temperature, typically 850 K, using 3 KW and 10 KW circulation heaters. Upon reaching the maximum reaction temperature, high-purity fuel is injected in the centerline of a heated nitrogen stream about 1 m from the reactor inlet to ensure complete vaporization. The synthetic air at reaction temperature and pre-vaporized fuel/nitrogen are rapidly mixed (<1.5 ms) in an opposed jet annular mixing nozzle at the

inlet of the reactor. The fuel concentration is kept low to minimize the temperature rise from heat release during exothermic chemical reactions. Equivalence ratios are usually set very lean to limit heat release. To further maximize temperature uniformity along the PFR length, three independently controlled surface bead heaters maintain the inlet, test, and outlet sections at desired initial gas temperature.

A direct transfer controlled cool down (DT-CCD) operational procedure was used to map reactivity as a function of temperature at a selected reaction time of 120 ms. The reactor is stabilized at its highest temperature and is allowed to cool. A water-cooled, borosilicate glass-lined, stainless steel probe with an integral type-K sample thermocouple continuously extracts and quenches a gas sample from the centerline of the reactor tube. The quenching time, defined as the time from sampling until the sample temperature is below 473 K, is less than or approximately 1 ms. The sampling probe position is adjusted as the reactor cools down, to maintain the selected residence time over a temperature range of 550 – 850 K and at a constant pressure of 8 atm. Upon exiting the gas sampling probe, samples flow at 0.025 L/s to a three-way heated valve via a heated glass-lined transfer line. From the three-way valve, the flow is directed to an online non-dispersive infrared (NDIR) gas analyzer for continuous carbon monoxide (CO) and carbon dioxide (CO<sub>2</sub>) measurements (uncertainty  $\pm$  25 ppm) and an electrochemical cell for oxygen measurements (uncertainty  $\pm$  1250 ppm). For detailed analysis of gas samples, a gas chromatograph with a flame ionization detector coupled to a mass spectrometer (GC-MS-FID) is used. When a sample is desired for analysis of stable intermediate species, the reactor temperature is held constant and the three-way valve is switched to rapidly fill a heated, evacuated 1-ml stainless steel GC sample loop

to 76 kPa. The 3-way valve is then switched back to directing the flow to the permanent gas analyzers and the contents of the GC sample loop are introduced into the GC column. While the GC-MS-FID analysis is performed on the first sample, the PFR temperature is decreased to the next desired sample temperature.

### 3.3.2 Pyrolysis Experiments Methodology

Prior to this study, the PFR facility had only been used to investigate the low to intermediate temperature (typically 550 – 850 K) oxidation of hydrocarbons and jet fuels. For pyrolysis runs, the high temperature limit was raised to 1000 K, after performing several initial characterization runs. The maximum achieved reaction temperature was 1000 K. The experiments reported in this research covered a temperature range of 850 – 1000 K and were run at a residence time of 168 ms. Sample collection procedure during the pyrolysis experiments was identical to that of oxidation tests. The collected samples were analyzed with the GC/MS/FID using the same GC program method for oxidation experiments (see Appendix A.2) as well as identification and quantification techniques as described in section 3.2.

The maximum operable temperature and residence time for pyrolysis studies were determined by performing several characterization runs. It was concluded that the PFR could safely operate at temperatures as high as ~ 1025 K. In addition, the effect of residence time on fuel decomposition was investigated in a pyrolysis experiment with *n*-decane, at five selected residence times covering the range of 90 -168 ms, at a temperature of 1000 K and at a pressure of 8 atm. The range of residence time that can be achieved in the current setup, is primarily limited by two parameters: the reactor geometry and the flow rate specifications for safe operation of the 10 KW and 3 KW

heaters. The maximum residence time of 168 ms was achieved by reducing the flow rate set point for the Nitrogen-Oxidizer mass flow controller to the determined minimum safe mass flow rate of 120 stdl / min and by fixating the sample probe at a distance of 38.00 cm from the entrance of quartz reactor tube. As displayed in Figure 3-2, the extent of fuel decomposition as well as the level of pyrolysis products was slightly higher for the sample extracted at the residence time of 168 ms, indicating a minimal effect of residence time on fuel conversion over the studied range of residence times. As mentioned, for the pyrolysis experiments, the residence time was 168 ms; the maximum achievable reaction time while maintaining a safe operation of the PFR facility at 1000 K and 8 atm.

These conditions represent the start of intermediate temperature ( $> 950$  K) regime of hydrocarbon pyrolysis. Increasing the operational temperature beyond the current 1000 K limit requires an upgrade of the PFR heaters and is beyond the scope of this research. Although such upgrade is desired and recommended for future pyrolysis studies, the current investigation does provide some preliminary insight to the pyrolysis characteristics of the studied fuel(s).

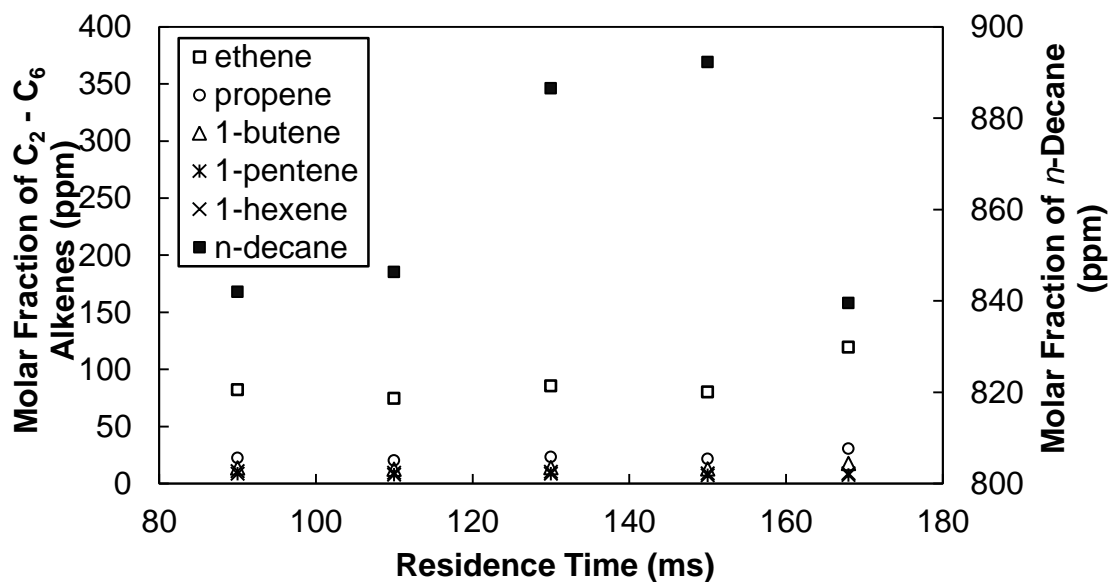


**Figure 3-2: The effect of residence time on formation of C2 – C6 alkenes during the pyrolysis of *n*-decane at 1000 K and 8 atm.**

### 3.3 Closure

This chapter described the experimental facility used for investigation of oxidation and pyrolysis of selected fuel components. The main components of the system, including the PFR and the analytical chemistry instrumentation, were explained. In addition, the experimental methodologies as well as sampling collection and analysis procedures were presented. Additional information about the maintenance, replacement of parts, and calibration of the analytical chemistry equipment, which included the GC/MS/FID system and the CO/CO<sub>2</sub>/O<sub>2</sub> detector, is presented in the appendices. The next chapter presents chemical kinetic models used for comparative analysis of experimental data as well as the model conditions used in CHEMKIN-PRO environment to simulate the flow reactor data.

## CHAPTER 4 : CHEMICAL KINETIC MODELS USED FOR COMPARATIVE ANALYSIS OF EXPERIMENTAL DATA

### 4.1 Introduction

The PFR data was used to validate several existing chemical kinetic models for oxidation and pyrolysis of *n*-decane and 2,7-DMO. These models included 1) the Lawrence Livermore National Laboratory (LLNL) mechanism for oxidation and pyrolysis of C<sub>8</sub> – C<sub>16</sub> *n*-alkanes and C<sub>7</sub> – C<sub>20</sub> 2-methylalkanes [21] (referred to as LLNL 2011 in this text), 2) the JetSurf v 1.0 model [27], 3) an optimized version of JetSurf 1.0 model [28], and 4) the Li *et al.* model for oxidation and pyrolysis of 2,7-DMO [26]. The LLNL 2011 and the JetSurf mechanisms were used for the purpose of validation against *n*-decane oxidation and pyrolysis data. Only the Li *et al.* model included low temperature chemistry pathways for 2,7-DMO. As it was mentioned in Chapter 2, two additional models for 2,7-DMO, one by Liu *et al.* [47] and one by Slavinskaya *et al.* [53], have been developed. However, the Liu *et al.* model for 2,7-DMO is a high-temperature mechanism and its brief examination indicated no reactivity at PFR conditions. Also, the mechanism by Slavinskaya *et al.* has yet to be made available for external use. Consequently, neither was examined in this study.

Section 4.2 provides an overview of the used mechanisms for validation against the PFR data. In Section 4.3, the conditions used to exercise the models in CHEMKIN-PRO software code are explained. In addition, this section will provide information regarding the post-processing of simulation results. A closure to this chapter will be presented in Section 4.4.

## 4.2 Chemical Kinetic Models Used for Validation Against Experimental Data

### 4.2.1 The Lawrence Livermore National Laboratory Mechanism

The experimental data from the oxidation and pyrolysis tests with *n*-decane were compared against the predictions of a comprehensive Lawrence Livermore National Laboratory (LLNL) mechanism by Sarathy *et al.* (2011) for oxidation and pyrolysis of *n*-alkanes from C<sub>8</sub> to C<sub>16</sub> and 2-methylalkanes from C<sub>7</sub> to C<sub>20</sub> [21]. The LLNL 2011 model is based on a comprehensive detailed *n*-heptane (C<sub>7</sub>H<sub>16</sub>) chemical kinetic mechanism, previously developed by Curran *et al.* (1998) [59] and later extended by Westbrook *et al.* (2009) [60] to describe the oxidation and pyrolysis of *n*-alkanes up to C<sub>16</sub>. The term “comprehensive” is used in this context to emphasize the fact that these mechanisms have been validated using a variety of experimental inputs such as those from flow reactors, rapid compression machines, laminar flames, and shock tubes.

Using a modular form for mechanism construction, the LLNL 2009 model contains 25 reaction classes for the low temperature regime that is initiated by  $\cdot R + O_2$  reactions and 9 reaction classes for the high temperature regime where major alkyl radicals decompose thermally into a smaller alkyl radical and an olefin species. Each reaction class consists of all reactions that have the same functional groups. This generally translates into shared similarities in the shape of the potential energy surfaces along the reaction pathways. The *n*-decane sub-mechanism contains 940 species and 3878 reactions. The LLNL 2009 mechanism was later updated by Sarathy *et al.* [21] and was included as a sub-mechanism in LLNL model for 2-methylalkanes from C<sub>7</sub> up to C<sub>20</sub> (2011). The modifications to the LLNL 2009 mechanism included updates to the core chemistry mechanism (i.e. the detailed *n*-heptane model) and important rate rules as well

as addition of new reaction classes, e.g. addition of concerted elimination of hydroperoxy radical ( $\cdot\text{HO}_2$ ) from alkylperoxy radical ( $\cdot\text{RO}_2$ ) (i.e. class 16) to the low temperature reaction classes. The mechanism contains 20 reaction classes for the low temperature regime and 10 reaction classes for the high temperature regime. The high temperature reaction classes are numbered 1 to 10. The low temperature reaction classes are numbered 11 to 30. The low temperature reaction classes are the same for the LLNL 2011 mechanism and the Li *et al.* model. These classes are listed in Section 4.2.3.

It should be noted that the entire LLNL 2011 mechanism contains 7171 species and 31669 reactions, large enough that the default integer type in CHEMKIN-PRO would not allow for solving the problem when the sensitivity analysis was turned on. This issue will be further explained in Appendix A.3. To overcome this constraint, for simulation of *n*-decane experiments, a sub-mechanism of LLNL 2011, i.e. the sub-mechanism for *n*-alkanes and 2-methylalkanes up to  $\text{C}_{12}$ , was used. This sub-mechanism will be referred to as LLNL 2011 throughout the text. The use of this sub-mechanism which contains 2755 species and 11173 reactions allowed for reduced computational time and for performing the sensitivity analysis when needed.

In general, it is advised in the mechanism documentation that for high temperature runs, the reaction classes for low temperature chemistry can be discarded. The defining line between the two regimes depends on pressure to a large extent. For the pressure of 8 atm, the cutting edge is around 900 K. The entire mechanism as well as the herein used sub-mechanism can be downloaded from <https://combustion.llnl.gov/mechanisms/alkanes/2-methyl-alkanes-and-n-alkanes> (last retrieved in November 2015).



#### 4.2.2 The JetSurf v 1.0 Model and the Optimized JetSurf Model

The PFR pyrolysis data for *n*-decane was also compared with two variations of the Jet Surrogate Fuel Model: the un-optimized JetSurf v 1.0 from Wang and co-workers at the University of Southern California (Sirjean *et al.*, 2009) and the optimized JetSurf (Banerjee *et al.*, 2015). JetSurf v 1.0 is a detailed mechanism primarily focused on high temperature oxidation and pyrolysis of *n*-alkanes up to *n*-dodecane (C<sub>12</sub>). The mechanism can be downloaded from

<http://web.stanford.edu/group/haiwanglab/JetSurF/> (last retrieved in October 2015).

JetSurf v 1.0 consists of 194 species and 1459. For simulation of oxidation chemistry in the low temperature and NTC regimes, the mechanism employs 4 species, 12-step lumped low temperature model based on the work of Bikas and Peters [61] on modeling the combustion of *n*-decane. Although supplemented by this lumped reaction set, the JetSurf mechanism has shown to be inadequate for simulation of the PFR oxidation data of this study. The model predicted no *n*-decane reactivity at PFR conditions. It was therefore, only pursued for comparisons with the pyrolysis data.

In addition to JetSurf v 1.0, a recently developed optimized version of JetSurf v 1.0 [28], with 196 species and 1478 reactions, was examined. Denoted as Optimized JetSurf, this mechanism is a tuned version of JetSurf v 1.0, in which a method known as Method of Uncertainty Minimization Using Polynomial Chaos Expansion (MUM-PCE) has been used to improve the fidelity and to decrease the uncertainty bands. For optimization targets, several sets of experimental data for *n*-dodecane obtained from shock tubes and laminar flame configurations were used. Comparisons of the Optimized model with

experimental data sets which were not directly used for optimization targets also indicated an improvement in predictions of ignition delay data as well as reactivity profiles for *n*-dodecane. The CHEMKIN input files for the Optimized JetSurf model are available as supplementary material to [28]. It should be noted that in the reaction mechanism files, *n*-decane (C<sub>10</sub>H<sub>22</sub>) is denoted as NC10H22. Also, the five possible decyl radicals of 1-decyl, 2-decyl, 3-decyl, 4-decyl, and 5-decyl are referred to as PXC10H21, SXC10H21, S2XC10H21, S3XC10H21, and S4XC10H21, respectively.

#### 4.2.3 The Li *et al.* Model for 2,7-Dimethyloctane

The only available 2,7-DMO model with low temperature kinetic pathways is the recently developed detailed chemical kinetic model by Li *et al.* [26]. The predictions of this model were compared with the PFR oxidation data. The 2,7-DMO mechanism extends the comprehensive chemical kinetic model for 2-methylheptane (2-MHP), 3-methylheptane (3-MHP), and 2,5-dimethylhexane (2,5-DMH) by LLNL and King Abdullah University of Science and Technology (KAUST) [21, 24, 47] to include high temperature pathways as well as new low temperature kinetic schemes for 2,7-DMO.

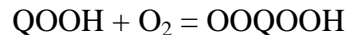
The oxidation model contains 20 reaction classes for the low and negative temperature coefficient (NTC) regimes and 10 reaction classes for the high temperature regime. For the low temperature and NTC regimes, these reaction classes (denoted as classes 11 – 30) are:

11) Addition of molecular oxygen (O<sub>2</sub>) to alkyl radicals ( $\cdot R$ ) to form alkylperoxy radicals ( $\cdot RO_2$ ):  $R + O_2 = RO_2$

12) Addition of alkyl radical with alkylperoxy radical to form two RO molecules:  
 $R + RO_2 = RO + RO$

- 13) Addition of alkyl radical with hydroperoxy radical ( $\cdot\text{HO}_2$ ) to form RO and hydroxyl radical ( $\cdot\text{OH}$ ):  $\text{R} + \text{HO}_2 = \text{RO} + \text{OH}$
- 14) Reaction of alkyl radical with  $\text{CH}_3\text{O}_2$  to form RO and  $\text{CH}_3\text{O}$ :  $\text{R} + \text{CH}_3\text{O}_2 = \text{RO} + \text{CH}_3\text{O}$
- 15) Isomerization of alkylperoxy radical to alkyl hydroperoxide (QOOH):  $\text{RO}_2 = \text{QOOH}$
- 16) Concerted (i.e. direct) elimination of hydroperoxy radical from alkylperoxy radical:  $\text{RO}_2 = \text{alkene} + \text{HO}_2$
- 17) Bi-molecular reaction between alkylperoxy radical and hydroperoxy radicals to form ROOH and OH:  $\text{RO}_2 + \text{HO}_2 = \text{ROOH} + \text{OH}$
- 18) Bi-molecular reaction between alkylperoxy radical and hydrogen peroxide ( $\text{H}_2\text{O}_2$ ) to form ROOH and  $\text{HO}_2$ :  $\text{RO}_2 + \text{H}_2\text{O}_2 = \text{ROOH} + \text{HO}_2$
- 19) Bi-molecular reaction between alkylperoxy radical  $\text{CH}_3\text{O}$ :  $\text{RO}_2 + \text{CH}_3\text{O} = \text{RO} + \text{CH}_3\text{O} + \text{O}_2$
- 20) Addition of two alkyl radicals to form two RO molecules and  $\text{O}_2$ :  $\text{RO}_2 + \text{RO}_2 = \text{RO} + \text{RO} + \text{O}_2$
- 21) Decomposition of ROOH:  $\text{ROOH} = \text{RO} + \text{OH}$
- 22) RO decomposition
- 23) Formation of cyclic ether:  $\text{QOOH} = \text{cyclic ether} + \text{OH}$
- 24) Decomposition of QOOH radicals with a radical site  $\beta$  to OOH group:  $\text{QOOH} = \text{alkene} + \text{HO}_2$
- 25) Decomposition of QOOH radicals with a radical site  $\gamma$  to OOH group:  $\text{QOOH} = \text{alkene} + \text{carbonyl} + \text{OH}$

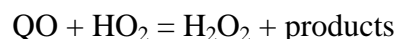
26) Addition of O<sub>2</sub> to QOOH to form peroxyalkyl hydroperoxide (OOQOOH):



27) Isomerization of OOQOOH and formation of carbonylhydroperoxide and OH

28) Decomposition of carbonylhydroperoxide to form oxygenated radical species and OH

29) Cyclic ether reactions with OH and HO<sub>2</sub>: QO + OH = H<sub>2</sub>O + products and



30) Decomposition of large carbonyl species and carbonyl radicals

The overall mechanism consists of 1571 species and 6833 reactions. The rate constants for the reactions that belong to the low and negative temperature coefficient (NTC) regimes are taken from the 2,5-dimethylhexane mechanism by Sarathy *et al.* (2014), as the 2 and 7 H-abstraction sites in the structure of 2,7-dimethyloctane were considered far away enough to allow for the assumption that the rate data in 2,5-dimethylhexane model could also be used for 2,7-dimethyloctane.

Although containing both low and high temperature chemistry reaction schemes, the mechanism was developed mainly to simulate the high temperature shock tube ignition delay time measurements for 2,7-DMO (see Chapter 2 for additional details). In that study, the model's deficiency in predicting the ignition delay times under lean conditions and intermediate temperatures was evident and suggested the need for additional investigation of aspects such as the accuracy of thermochemistry values of important radicals pertinent to low temperature and NTC regions.

An on-going effort by Westbrook and co-workers is currently focused on upgrading the Li *et al.* model for 2,7-DMO. The details of the upgrades, particularly those involving

the low temperature reactions classes for 2,7-DMO, will be provided in Chapter 5, Section 5.6.

### **4.3 The Simulation of Chemical Kinetic Models and Post-Processing of Results in CHEMKIN-PRO Software**

To run the models in CHEMKIN-PRO (release 15131, July 2013) software code, the plug flow reactor module with one inlet stream and one outlet stream under adiabatic conditions (problem type: solve energy equation) was used. The inputs included the reactor geometry (i.e. ending axial position of 40 cm and diameter of 2.2 cm), temperature range, pressure (8 atm for this study), axial velocity (333.33 cm/s for oxidation runs, corresponding to a residence time of 120 ms and 238.095 cm/s for pyrolysis runs, corresponding to a residence time of 168 ms), and molar fraction of the reactants. For simulation of 2,7-DMO oxidation experiments, the input fuel concentration was an average of three experiments. For both pyrolysis and oxidation cases, a parameter study for temperature was set with oxidation runs covering the temperature range of 550 – 850 K and pyrolysis runs covering the temperature range of 850 – 1100 K. Unless otherwise specified, the simulations were run at 10 K intervals. Absolute and relative tolerance values were set to  $1.0 \times 10^{-14}$  and  $1.0 \times 10^{-12}$ , respectively. Also, the input chemistry set only includes a “Gas-Phase Kinetics” file and a “Thermodynamics Data” file. The surface reactions and transport effects are negligible with the PFR methodology, eliminating the need for appending a “Surface Kinetics” file and a “Gas Transport Data” file.

Here, it should be emphasized that in plug flow reactor model, the fluid is essentially modeled as flowing through the reactor as a series of infinitesimally thin “plugs” with

zero volume. The residence time of each plug is a function the distance it has traveled within the reactor, starting from  $x = 0$  to  $x$  equal to the ending axial position (40 cm in the case of Drexel PFR). In fact, if the temperature and pressure are held constant, the data can be simulated using the 0-D closed homogeneous batch reactor setup in CHEMKIN-PRO with “constrained pressure and temperature” condition, where the input file will contain only one specified value for pressure and one specified value for temperature.

In addition to calculation of species profiles as a function of parameters such as temperature and reaction time, the software provide tools to investigate the underlying chemistry in details. The key pathways leading to production of a specific species can be investigated using the rate of production analysis (ROP) analysis and reaction flux analysis. One can start with species “ $x$ ” and back-track the key pathways and source species for it. For example, the conversion of parent fuel to CO can be investigated by specifying the fuel as start species and CO as end species. The software will demonstrate the key pathways and their relative contributions for the conversion of fuel to CO. This can be extended to various species and combinations of preferences. In addition, sensitivity analysis provides information on sensitive reactions with respect to any species in the mechanism. For a sensitive reaction, a change in the rate coefficient will cause a significant change in the overall reaction rate. A positive sensitivity value for a reaction with respect to a species is indicative of a reaction that enhances the production of that species, while a negative value corresponds to a reaction that inhibits the production. To generate the ROP analysis and sensitivity analysis, both the “reaction path analyzer” and the “plot results” options in “analyze results” panel of the project tree in CHEMKIN-PRO was used. The “reaction path analyzer” feature uses provides a

graphical interface to investigate the relative importance of reaction pathways that lead to the formation of a select species. The feature can also be used for performing the sensitivity analysis for any selected species at a specified condition (that is defined by temperature, pressure, and residence time). The only export for the “reaction path analyzer” is one to a raster based still image in PNG format. There is no option to export to scalar vector graphics format. However, the data used by the reaction path analyzed is also available from the normal solution post-processor. Selecting the “plot results” option activates a post-processor panel to plot or export the generated solution files. The generated solution can be exported in a variety of ways depending on the need of the user. Additional information about the visualization features in CHEMKIN-PRO, the graphical post-processor and other post-processing alternatives can be found in CHEMKIN visualization manual.

To increase the computational capabilities when running larger mechanisms, the modeling computer was upgraded to a Dell T3610 workstation in May 2014. Additional information can be found in Appendix A.3. The appendix will also include information about troubleshooting of errors encountered while exercising larger mechanisms in CHEMKIN-PRO.

#### **4.4 Closure**

This chapter provided a brief overview of several existing detailed chemical kinetic models used for comparisons against the PFR data. In addition, some key input parameters to implement the reactor model in CHEMKIN-PRO environment were presented. The chapter also described the use of tools such as ROP analysis and sensitivity analysis that are utilized in the post-processing stage to understand the inner-

workings of the studied chemical kinetic models and to identify the sources of variations between the experiments and the models as well as among the mechanisms. The results of 2,7-DMO and *n*-decane oxidation experiments and the associated model analysis will be presented in Chapter 5.



## CHAPTER 5 : LOW-TEMPERATURE OXIDATION OF 2,7-DIMETHYLOCTANE AND *N*-DECANE

### 5.1 Introduction

This phase of the study focused on the oxidation of 2,7-DMO over the temperature range of 550 – 850 K. The reactivity of 2,7-DMO was mapped over the low temperature and NTC regime by continuous monitoring of CO, CO<sub>2</sub>, and O<sub>2</sub>. Full speciation of stable intermediates from the oxidation was performed at selected sample temperatures. To explore the effect of isomerization on some key oxidations characteristics, the PFR was also used to oxidize *n*-decane, the straight chain analog to 2,7-DMO, at comparable testing conditions.

The findings from PFR oxidation experiments with 2,7-DMO were compared with the calculations of Li *et al.* model [26]. The possible sources of variations were investigated. In addition, a collaborative effort was initiated with the model developers and in particular, with Dr. Charles Westbrook (LLNL) to refine the low temperature chemistry reactions and their associated rate coefficients. The computations by the refined model were compared with the PFR data and the improvements as well as some remaining discrepancies were noted.

Section 5.2 discusses the experimental conditions. Section 5.3 discusses the results of the three replicate oxidation experiments with 2,7-DMO as well as the comparisons with *n*-decane oxidation study. The details of the model calculations and species naming methodology are presented in Section 5.4. Section 5.5 presents the comparison between the PFR data and calculations of Li *et al.* model for 2,7-DMO. In addition, the possible sources of discrepancies between the experimental measurements and the model

predictions are discussed in this section. The updates made by Dr. Westbrook to the low temperature reaction classes of the Li *et al.* model are briefly discussed in Section 5.6. The section also presents the comparisons between the modified mechanism with the original mechanism as well as with the experimental data, pointing out the improvements as well as the remaining areas for model refining. A closure to this chapter is presented in Section 5.7.

## 5.2 Experimental Conditions

Three replicate DT-CCD experiments for 2,7-DMO were conducted. The experimental conditions and the uncertainties are shown in Table 5-1. The initial fuel molar fraction was 843 ppm with an uncertainty of one standard deviation being equal to  $\pm 13$  ppm, determined by GC-MS analysis of a fuel calibration sample (fuel and N<sub>2</sub>). The composition of the reactants corresponds to a lean equivalence ratio of 0.31 ( $\pm 0.05$ ).

**Table 5-1: Test conditions for 2,7-DMO oxidation, residence time 120 $\pm$ 10 ms.**

Parameter	Expt 1	Expt 2	Expt 3	Avg	Uncertainty
2,7-DMO, ppm	843	856	830	843	$\pm 13$
O <sub>2</sub>	42,100	42,100	42,100	42,100	$\pm 1250$
N <sub>2</sub>	Balance	Balance	Balance	Balance	-
Equivalence Ratio ( $\phi$ )	0.30	0.32	0.31	0.31	$\pm 0.05$
Temperature, K	550 – 850	550 – 850	550 – 850	550 – 850	-
Pressure, atm	8.000	8.000	8.000	8.000	$\pm 0.025$
Residence Time (ms)	120	120	120	120	$\pm 10$

The reported *n*-decane experiment was conducted with a lower initial fuel molar fraction of  $592 \pm 19$  ppm (corresponding to  $\phi = 0.22$ ) to account for the effect of isomerization on reactivity and the expected higher CO production levels during the oxidation of the corresponding straight chain C<sub>10</sub> alkane. The experiment was conducted over the temperature range of 550 – 850 K, at a pressure of 8 atm, and a residence time of 120 ms. It should be noted that a number of studies covering an equivalence ratio range of 0.17 – 0.22 was conducted with the PFR and similar trends were observed. Also, the residence time of 120 ms and the pressure of 8 atm used in 2,7-DMO and *n*-decane experiments are consistent with previous PFR studies of jet fuels and their surrogate components (e.g., see [56]). The PFR was allowed to naturally cool at a rate of 2 – 5 K/min. The CO was continuously recorded. For 2,7-DMO, the DT-CCD methodology allowed for collection of samples at several desired temperatures, the natural cooling during *n*-decane oxidation only allowed for collection of a few samples. Several samples were collected at fuel calibration point to allow for determination of uncertainty in fuel measurement during each experiment. A sample was extracted at 715 K and analyzed with the GC-MS-FID. While the speciation data for this sample doesn't directly compare to speciation data from 2,7-DMO, it provides a qualitative understanding of the distribution of the major intermediate species near the start of NTC region.

## **5.3 Experimental Results**

### **5.3.1 Oxidation of 2,7-Dimethyloctane**

2,7-DMO exhibited classical NTC behavior as indicated by the data shown in Figure 5-1. It should be noted that the sample temperature refers to the temperature of the products at the 120 ms residence time sampling location in the quartz reactor and thus

includes temperature rise due to heat release in experiments. In model simulations, the temperature rise is accounted for by the difference in calculated end point temperature and the input inlet temperature. The experimental sample temperature is analogous to the calculated end point temperature by the model. Therefore, for the plots comparing the experimental data with the model predictions, a common “sample temperature” term is used. The Peak reactivity and the low temperature limit of the NTC regime, characterized by maximum O<sub>2</sub> consumption and CO production, is near 695 K with a measured CO molar fraction of approximately 800 ppm, accounting for approximately 10% of total carbon in the unreacted mixture. The NTC behavior was manifested through a decrease in CO levels with increasing the temperature over the temperature range of 695 K – 780 K. No reactivity was observed at temperatures above ~ 780 K. The lowest fuel molar fraction was measured at 699 K sample point, with over 90% of 2,7-DMO being converted to intermediate species. Because of an instrument error, CO<sub>2</sub> was not recorded during experiment 1. The CO<sub>2</sub> data from experiments 2 and 3 showed that CO<sub>2</sub> trend was similar to that for CO. The maximum CO<sub>2</sub> concentration was approximately 240 ppm at 695 K.

For detailed speciation, five samples were extracted at sample temperatures of 837 K, 749 K, 699 K, 646 K, and 546 K, which represent points near peak reactivity, points near the start and end of reactivity, and points where no reactivity was observed. Seventy-three stable intermediate species (including the parent fuel) were identified and measured using the techniques described in Section using the techniques described in Section 3.2. Together with CO and CO<sub>2</sub>, these measured stable intermediates accounted for 85% -

105% of total carbon in the reactants. The minimum carbon balance of 85% occurred at 646 K sample point. Oxygen balances were 100% -106%.

Table 5-2 lists all species with measured quantities and Figure 5-2 organizes the chemical classes measured at each temperature. Alkenes peaked during the NTC region, accounting for 11% of total carbon input at 749 K sample point. At 749 K, the major alkenes produced in descending order were *iso*-butene ( $\text{iC}_4\text{H}_8$ ), propene ( $\text{C}_3\text{H}_6$ ), 5-methyl-1-hexene ( $\text{C}_7\text{H}_{14}$ ), ethene ( $\text{C}_2\text{H}_4$ ), and 3-methyl-1-butene ( $\text{C}_5\text{H}_{10}$ ) were the major alkenes produced. Figure 5-3 plots the major  $\text{C}_2$ - $\text{C}_7$  alkenes produced from 2,7-DMO oxidation. It should be noted that although the peaks for all butene isomers (1-, 2-, and *iso*-) are expected to co-elute, the mass spectra matching of the corresponding peak did not positively identify 1-butene and 2-butene. Production of *iso*-butene (2-methyl-1-propene) in major quantities during the oxidation of branched alkenes such as *iso*-cetane ( $\text{C}_{16}\text{H}_{34}$ ) and *iso*-octane ( $\text{C}_8\text{H}_{18}$ ) has been widely reported in the literature. In addition, the high stability of *iso*-butene is known to play an important role in decreased reactivity of branched alkanes (e.g., see [22, 47]). Therefore, on the virtue of mass spectra matching as well as the existing literature, it is believed that for this experimental study, a significant fraction (if not all) of the quantified  $\text{C}_4\text{H}_8$  species is *iso*-butene. Nevertheless, to account for the possible existence of all of these isomers, the quantification and model predictions will be shown together as one data series. The model calculations for *iso*-butene only, will be also included. Still, Table 5-2 only lists *iso*-butene as the identified  $\text{C}_4\text{H}_8$  alkene.

As shown in Figure 5-4, among aldehydes, formaldehyde was produced in large quantities, particularly at peak reactivity, i.e. at 699 K, and accounted for 36% of total carbon in the reactants. Other key aldehydes, in descending order of molar fraction at

699 K sample point, included acetaldehyde, 2-methyl-2-propenal, hexanal, *iso*-butanal, and *iso*-pentanal. In general, the molar fraction of major aldehydes displayed a close dependence on NTC behavior, reaching peak production at the 699 K sample point.

Ketones displayed a similar trend, contributing to 13% of carbon balance at the sample temperature of 699 K. Acetone was the dominant ketone measured. At 699 K,  $207 \pm 25$  ppm of acetone was produced, accounting for about 7.5 % of total carbon input. At immediately adjacent sample points, i.e. at 646 K and 749 K, acetone accounted for 5.5 % and 3.5 % of total carbon input, respectively. Previous oxidation studies of *n*-dodecane by Kurman *et al.* [58] and the herein reported oxidation study of *n*-decane in the low temperature regime, did not identify acetone as an intermediate species. The production of high quantities of acetone, therefore, is concluded to be a direct result of the branched structure of 2,7-DMO. Methyl vinyl ketone (butenone) was the second dominant ketone, reaching a molar fraction of 13 ppm at 699 K sample point.

Ethers, particularly several tetrahydrofurans with attached methyl (CH<sub>3</sub>) group(s) in the structure, were also among the key classes of species produced during the oxidation of 2,7-DMO. A species identified as 5-Sec-butyl-2,2-dimethyltetrahydrofuran (C<sub>10</sub>H<sub>20</sub>O) accounted for about 6 % of total carbon input at peak production, i.e. at 749 K sample point. The next major ether, 2-Methyl-5-pentyltetrahydrofuran (C<sub>10</sub>H<sub>20</sub>O), contributed to about 2 % of carbon balance at this sample temperature.

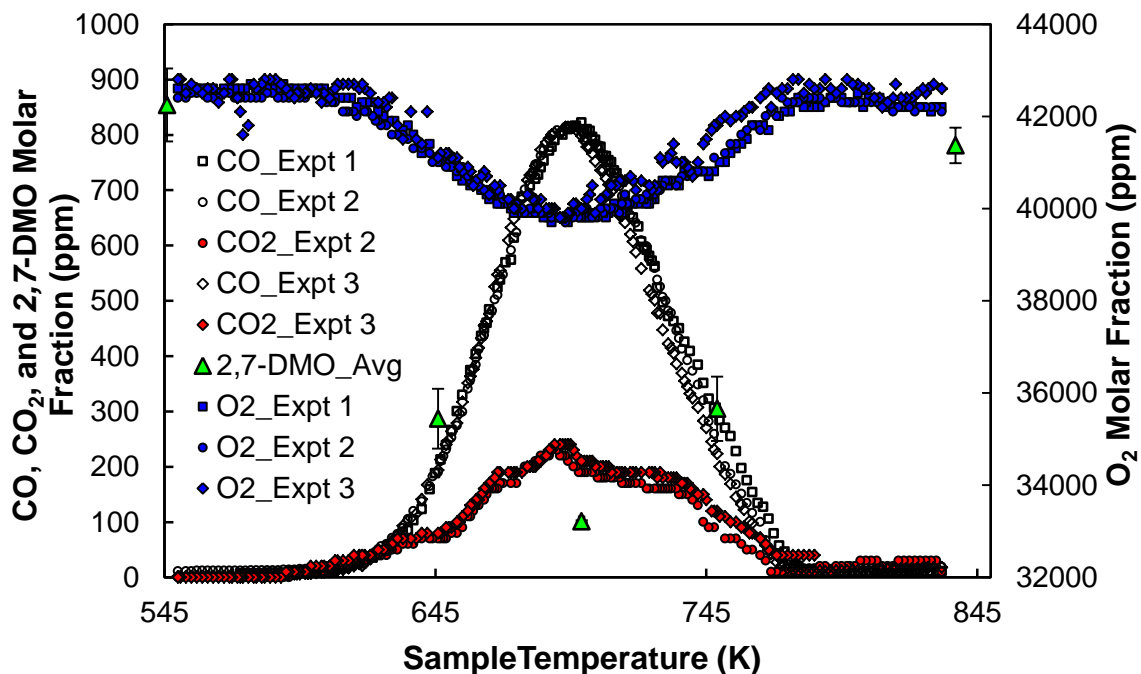


**Figure 5-1: Reactivity and 2,7-DMO profiles for replicate oxidation experiments; 8 atm; 120 ms; average initial fuel fraction  $843 \pm 13$  ppm.  $\text{CO}_2$  not recorded during Expt 1. Uncertainties:  $\pm 25$  ppm for CO and  $\text{CO}_2$ ;  $\pm 1250$  ppm for  $\text{O}_2$ .**

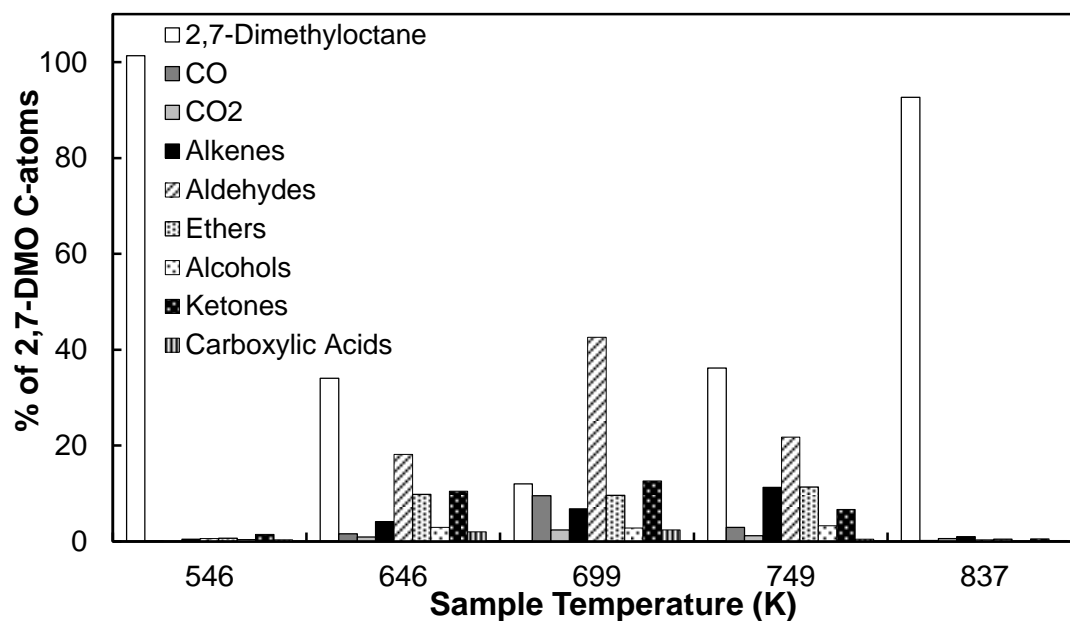


**Figure 5-2: Class analysis for 2,7-DMO oxidation. The classes shown account for  $\geq 1\%$  of total carbon input.**

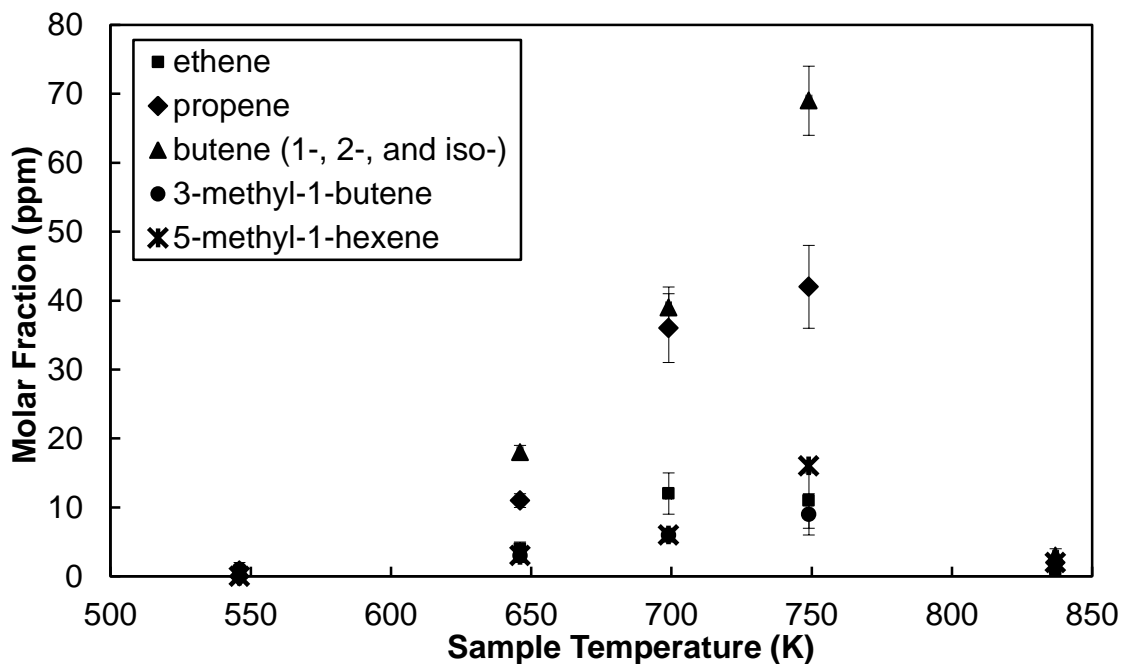


Figure 5-3: Major C<sub>2</sub>-C<sub>7</sub> alkenes produced during the oxidation of 2,7-DMO.

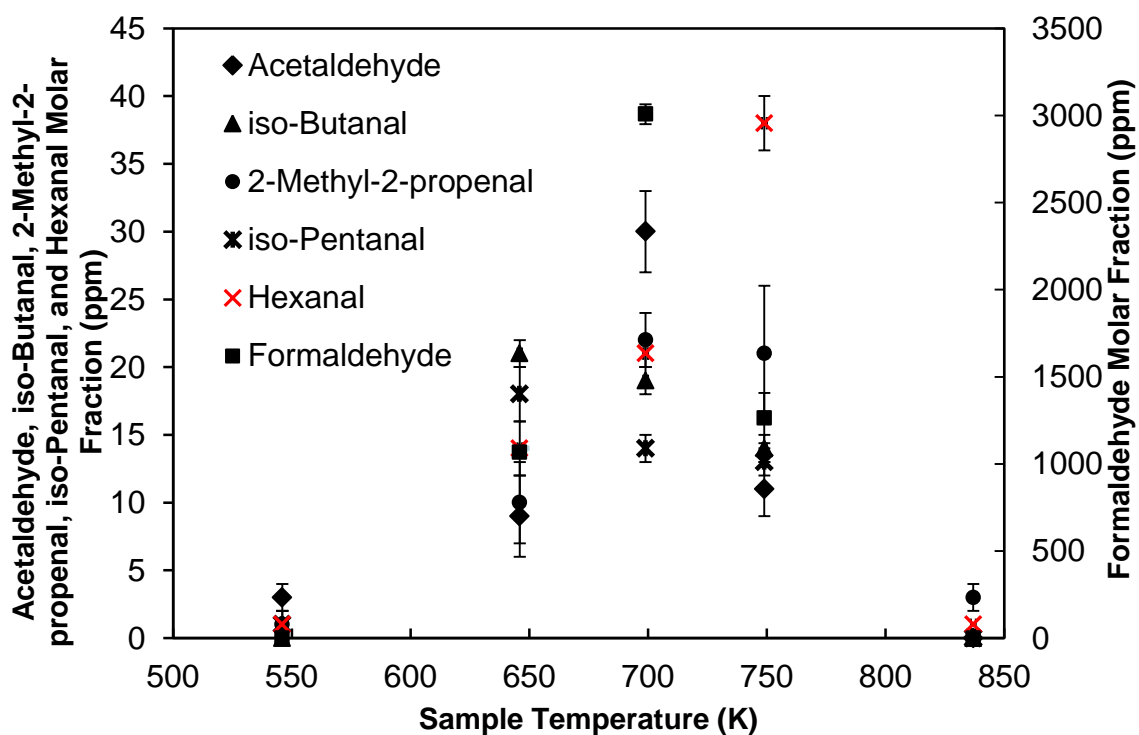


Figure 5-4: Major aldehydes produced during the oxidation of 2,7-DMO.



**Table 5-2: List of species identified and their quantified values, determined by the average of three 2,7-DMO experiments at nearly identical conditions with uncertainties being  $\pm 1$  standard deviation.**

Species	Molecular formula	546 K	646 K	699 K	749 K	837 K
2,7-dimethyloctane (parent fuel)	C <sub>10</sub> H <sub>22</sub>	854 ± 66	287 ± 54	101 ± 2	305 ± 58	781 ± 32
Ethene	C <sub>2</sub> H <sub>4</sub>	0	4 ± 1	12 ± 3	11 ± 4	1 ± 1
Formaldehyde	CH <sub>2</sub> O	0	1066 ± 31	3008 ± 57	1263 ± 145	0
Propene	C <sub>3</sub> H <sub>6</sub>	0	11 ± 1	36 ± 5	42 ± 6	2 ± 1
Acetaldehyde	C <sub>2</sub> H <sub>4</sub> O	3 ± 1	9 ± 3	30 ± 3	11 ± 2	0
iso-Butene	C <sub>4</sub> H <sub>8</sub>	1 ± 1	18 ± 1	39 ± 3	69 ± 5	3 ± 1
3-Methyl-1-butene	C <sub>5</sub> H <sub>10</sub>	1 ± 0	3 ± 1	6 ± 1	9 ± 1	2 ± 1
2-Propenal	C <sub>3</sub> H <sub>4</sub> O	1 ± 1	5 ± 1	10 ± 1	9 ± 1	3 ± 1
Acetone	C <sub>3</sub> H <sub>6</sub> O	2 ± 1	154 ± 14	207 ± 25	100 ± 11	0
1-Pentene	C <sub>5</sub> H <sub>10</sub>	1 ± 0	4 ± 2	5 ± 1	3 ± 1	1 ± 1
Trans-2-pentene	C <sub>5</sub> H <sub>10</sub>	1 ± 0	2 ± 0	3 ± 0	3 ± 1	1 ± 0
2-Methyl-1,3-butadiene	C <sub>5</sub> H <sub>8</sub>	1 ± 0	1 ± 0	3 ± 1	3 ± 0	1 ± 0
iso-Butene oxide / 2,2-Dimethyloxirane#	C <sub>4</sub> H <sub>8</sub> O	0	6 ± 1	5 ± 0	1 ± 0	0
iso-Butanal	C <sub>4</sub> H <sub>8</sub> O	0	21 ± 1	19 ± 1	14 ± 1	0
2-Methyl-2-propenal	C <sub>4</sub> H <sub>6</sub> O	1 ± 1	10 ± 3	22 ± 2	21 ± 5	3 ± 1
Methyl vinyl ketone	C <sub>4</sub> H <sub>6</sub> O	1 ± 0	3 ± 1	13 ± 1	4 ± 0	2 ± 1
Acetic acid	C <sub>2</sub> H <sub>4</sub> O <sub>2</sub>	2 ± 1	10 ± 3	15 ± 3	3 ± 1	2 ± 1
1-Hexene	C <sub>6</sub> H <sub>12</sub>	0	1 ± 0	1 ± 0	1 ± 0	0
2-Methylfuran	C <sub>5</sub> H <sub>6</sub> O	1 ± 1	3 ± 0	7 ± 1	3 ± 2	0
tert-Butyl alcohol / 2-methyl-2-propanol#	C <sub>4</sub> H <sub>10</sub> O	0	1 ± 0	3 ± 0	1 ± 0	0
(2E)-4-Methyl-2-pentene	C <sub>6</sub> H <sub>12</sub>	0	3 ± 1	2 ± 1	1 ± 0	0
iso-Pentanal / 3-Methylbutanal#	C <sub>5</sub> H <sub>10</sub> O	1 ± 1	18 ± 2	14 ± 1	13 ± 1	0
3,4-Dimethyl-2,5-dihydrofuran	C <sub>6</sub> H <sub>10</sub> O	1 ± 0	10 ± 2	4 ± 1	3 ± 0	0
Methyl vinyl ether	C <sub>3</sub> H <sub>6</sub> O	1 ± 1	4 ± 1	4 ± 0	3 ± 1	0
5-Methyl-1-hexene	C <sub>7</sub> H <sub>14</sub>	0	3 ± 1	6 ± 0	16 ± 2	2 ± 0
2-Methoxy-1-propene	C <sub>4</sub> H <sub>8</sub> O	0	0	3 ± 0	1 ± 0	0
1-Heptene	C <sub>7</sub> H <sub>14</sub>	0	1 ± 0	1 ± 0	1 ± 0	0
2,2-Dimethyltetrahydrofuran	C <sub>6</sub> H <sub>12</sub> O	0	1 ± 0	5 ± 1	5 ± 1	1 ± 0
5-Methyl-3-hexen-2-one	C <sub>7</sub> H <sub>12</sub> O	0	2 ± 0	3 ± 0	4 ± 1	0
4-Methyl-2-pentanone	C <sub>6</sub> H <sub>12</sub> O	0	4 ± 1	3 ± 1	1 ± 0	0
4-Methyl-4-penten-2-one	C <sub>6</sub> H <sub>10</sub> O	1 ± 0	1 ± 0	2 ± 0	2 ± 0	1 ± 0
Methyl acetate	C <sub>3</sub> H <sub>6</sub> O <sub>2</sub>	0	1 ± 0	7 ± 2	0	0
Hexanal	C <sub>6</sub> H <sub>12</sub> O	1 ± 0	14 ± 2	21 ± 1	38 ± 2	1 ± 0
3-Methyl-2-butenal	C <sub>5</sub> H <sub>8</sub> O	1 ± 1	6 ± 1	8 ± 1	4 ± 0	4 ± 0
4-Isopropyl-2,3-dihydrofuran	C <sub>7</sub> H <sub>12</sub> O	0	2 ± 0	2 ± 0	2 ± 1	0
1-(Isopentyloxy)ethylene	C <sub>7</sub> H <sub>14</sub> O	1 ± 1	1 ± 0	1 ± 0	1 ± 0	1 ± 1
4-Methyl-3-pentenal	C <sub>6</sub> H <sub>10</sub> O	1 ± 0	2 ± 0	3 ± 0	2 ± 1	0
3-Ethyl-2-pentanone	C <sub>7</sub> H <sub>14</sub> O	1 ± 1	8 ± 2	6 ± 1	3 ± 0	0
2-Isopropylloxirane	C <sub>5</sub> H <sub>10</sub> O	0	5 ± 0	8 ± 1	4 ± 0	3 ± 2
2-Hexenal	C <sub>6</sub> H <sub>10</sub> O	0	0	2 ± 1	1 ± 0	0
5-Methyl-2-hexanone	C <sub>7</sub> H <sub>14</sub> O	1 ± 1	3 ± 1	2 ± 0	1 ± 0	1 ± 0
5-Methylhexanal	C <sub>7</sub> H <sub>14</sub> O	1 ± 0	6 ± 2	5 ± 1	5 ± 1	0
5-Methyl-5-hexen-2-one	C <sub>7</sub> H <sub>12</sub> O	0	1 ± 0	3 ± 0	3 ± 0	0
Trans-7-methyl-3-octene	C <sub>9</sub> H <sub>18</sub>	0	1 ± 0	1 ± 0	2 ± 1	0
2-Methyl-1-octene	C <sub>9</sub> H <sub>18</sub>	1 ± 0	2 ± 1	2 ± 0	2 ± 0	0
2,7-Dimethyl-2-octene	C <sub>10</sub> H <sub>20</sub>	1 ± 0	4 ± 1	4 ± 0	7 ± 1	1 ± 0
Cis-4,6-dimethylcyclohexane-1,3-dione	C <sub>8</sub> H <sub>12</sub> O <sub>2</sub>	3 ± 1	5 ± 1	7 ± 1	5 ± 1	3 ± 2
3-Isopropyl-1-methyl-1-cyclohexene	C <sub>10</sub> H <sub>18</sub>	1 ± 0	2 ± 1	2 ± 1	1 ± 0	1 ± 0
3-Ethyl-2,2-dimethyloxirane	C <sub>6</sub> H <sub>12</sub> O	0	5 ± 2	6 ± 1	3 ± 0	0
2,7-Dimethyl-1-octene	C <sub>10</sub> H <sub>20</sub>	0	7 ± 1	7 ± 1	21 ± 4	2 ± 0
4-Methyl-3-pentenoic acid	C <sub>6</sub> H <sub>10</sub> O <sub>2</sub>	4 ± 1	25 ± 4	29 ± 5	5 ± 2	2 ± 1
5-Sec-butyl-2,2-dimethyltetrahydrofuran	C <sub>10</sub> H <sub>20</sub> O	1 ± 1	30 ± 2	34 ± 2	54 ± 5	1 ± 1
2-Methoxy-4-methyl-bicyclo[3.2.1]oct-2-ene	C <sub>10</sub> H <sub>16</sub> O	1 ± 0	7 ± 3	2 ± 0	1 ± 0	0
(1-Methoxy-pentyl)-cyclopropane	C <sub>9</sub> H <sub>18</sub> O	0	3 ± 0	2 ± 0	2 ± 1	0
2-Ethyl-4,6-dimethyltetrahydropyran	C <sub>9</sub> H <sub>18</sub> O	0	2 ± 0	2 ± 0	4 ± 1	0
2,5-Dipropyltetrahydrofuran	C <sub>10</sub> H <sub>20</sub> O	0	5 ± 1	4 ± 0	2 ± 1	0
1,1,2,3-Tetramethylcyclohexane	C <sub>10</sub> H <sub>20</sub>	0	1 ± 0	2 ± 0	2 ± 0	0
2,6-Dimethyl-7-octen-3-ol	C <sub>10</sub> H <sub>20</sub> O	0	2 ± 0	2 ± 0	5 ± 1	0

**Table 5-2: (continued)**

Species	Molecular formula	546 K	646 K	699 K	749 K	837 K
2-Nonanone	C <sub>9</sub> H <sub>18</sub> O	1 ± 0	2 ± 1	3 ± 1	2 ± 1	0
2-Acetylcyclohexanone	C <sub>8</sub> H <sub>12</sub> O <sub>2</sub>	1 ± 1	5 ± 2	7 ± 1	4 ± 1	0
2-Isopropyl-5-methylcyclohexanol	C <sub>10</sub> H <sub>20</sub> O	1 ± 1	4 ± 1	3 ± 0	3 ± 1	0
2,5-Diethyltetrahydrofuran	C <sub>8</sub> H <sub>16</sub> O	0	1 ± 0	2 ± 1	2 ± 0	0
2-Methyl-5-pentyltetrahydrofuran	C <sub>10</sub> H <sub>20</sub> O	1 ± 1	16 ± 2	14 ± 1	18 ± 2	0
(5-Methyltetrahydro-2-furanyl)methanol	C <sub>6</sub> H <sub>12</sub> O <sub>2</sub>	1 ± 0	23 ± 1	22 ± 2	22 ± 4	0
4,4-Dimethylhexanal	C <sub>8</sub> H <sub>16</sub> O	1 ± 0	6 ± 1	3 ± 0	2 ± 0	0
1-Decyn-4-ol	C <sub>10</sub> H <sub>18</sub> O	1 ± 0	4 ± 1	3 ± 1	4 ± 0	0
3-Methylcyclohexanol	C <sub>7</sub> H <sub>14</sub> O	1 ± 1	1 ± 0	2 ± 0	3 ± 1	1 ± 1
2-Hydroxy-8-methyl-nona-2,8-dien-4-one	C <sub>10</sub> H <sub>16</sub> O <sub>2</sub>	0	3 ± 0	2 ± 1	1 ± 0	0
2,2'-Bioxepane	C <sub>12</sub> H <sub>22</sub> O <sub>2</sub>	1 ± 0	5 ± 2	3 ± 1	1 ± 0	0
2,6-Dimethyl-3-heptanone	C <sub>9</sub> H <sub>18</sub> O	1 ± 1	2 ± 0	1 ± 0	1 ± 0	0
2,7-Dimethyl-3,5-octanedione	C <sub>10</sub> H <sub>18</sub> O <sub>2</sub>	1 ± 0	4 ± 2	1 ± 0	1 ± 1	0
3,3,6-Trimethyl-2,5-heptanedione	C <sub>10</sub> H <sub>18</sub> O <sub>2</sub>	1 ± 1	4 ± 1	4 ± 1	2 ± 1	0
2-Methyl-3-octanone	C <sub>9</sub> H <sub>18</sub> O	1 ± 0	3 ± 1	3 ± 1	1 ± 0	0
Carbon monoxide	CO	6 ± 5	134 ± 9	802 ± 12	248 ± 43	14 ± 3
Carbon dioxide	CO <sub>2</sub>	0	80 ± 14	200 ± 14	100 ± 14	50 ± 71
Oxygen	O <sub>2</sub>	42,600 ± 200	41,233 ± 351	39,900 ± 100	41,333 ± 493	42,200 ± 173
Water	H <sub>2</sub> O	144 ± 31	2200 ± 512	4989 ± 795	3132 ± 541	379 ± 87

### 5.3.2 Oxidation of *n*-Decane and Comparisons with 2,7-Dimethyloctane

The measured CO profiles during the experiment with *n*-decane are shown in Figure 5-5. In Figure 5-6, the measured CO profile in terms of the fraction of total carbon input are depicted for the *n*-decane experiment and three replicate 2,7-DMO experiments. The study revealed that *n*-decane is clearly more reactive than 2,7-DMO at tested conditions. The measurements indicated that during the oxidation of *n*-decane, CO peaks near 698 K, where it accounts for ~18% of total carbon input. For 2,7-DMO, the contribution of CO to total carbon balance at peak reactivity, i.e. the start of NTC, was only ~ 10%. As CO production is known to be an indicator of reactivity in the studied temperature regime, it is concluded that the branching does in fact inhibit the fuel reactivity to a considerable extent. Nevertheless, the start of reactivity and the onset of NTC for both isomers of decane occurred at only slightly different temperatures, approximately 695 K and 698 K for 2,7-DMO and *n*-decane, respectively.

Several studies of C<sub>7</sub> and smaller alkanes have shown that for branched structures, the NTC regime starts at lower temperatures and that the temperature range of NTC is wider

[62, 63]. The observations from the current PFR study suggests otherwise, indicating that the effect of branching on the start of NTC regime is almost negligible for larger lightly branched alkane. It was also observed that the temperature range for NTC regime is larger for *n*-decane. While 2,7-DMO was not reactive at temperatures higher than 780 K, the reactivity of *n*-decane continued until approximately 820 K.

For *n*-decane, samples were collected and speciated near peak reactivity and near the start and end of reactivity. A sample was collected and speciated at 715 K. While the speciation data for this sample doesn't directly compare to speciation data from 2,7-DMO at 699 K sample point, it still provides a qualitative understanding of distribution of C<sub>2</sub>-C<sub>4</sub> alkenes near peak reactivity and the start of NTC region. The GC-MS-FID analysis of a sample collected at 715 K indicated that ~ 94 % of *n*-decane was consumed at this temperature. At this temperature, ethene was the most abundant alkene with a molar fraction of 68 ppm. Propene and butene levels were considerably lower at 23 ppm and 10 ppm, respectively. The observation confirmed that isomerization reverses the distribution of C<sub>2</sub>-C<sub>4</sub> alkenes. Trace amounts of pentene and hexene were identified at 3 ppm and 2 ppm, respectively. Acetone was not detected as an intermediate species, confirming that its production is a unique result of branching in the fuel structure. Figure 5-7 presents the experimental measurement of C<sub>2</sub>– C<sub>4</sub> alkenes at 715 K sample point. The molar fractions of these species were negligible for sample temperatures near the start and end of reactivity. The figure also demonstrates the computed profiles of these species by LLNL 2011 model over the temperature range of 600 – 850 K.

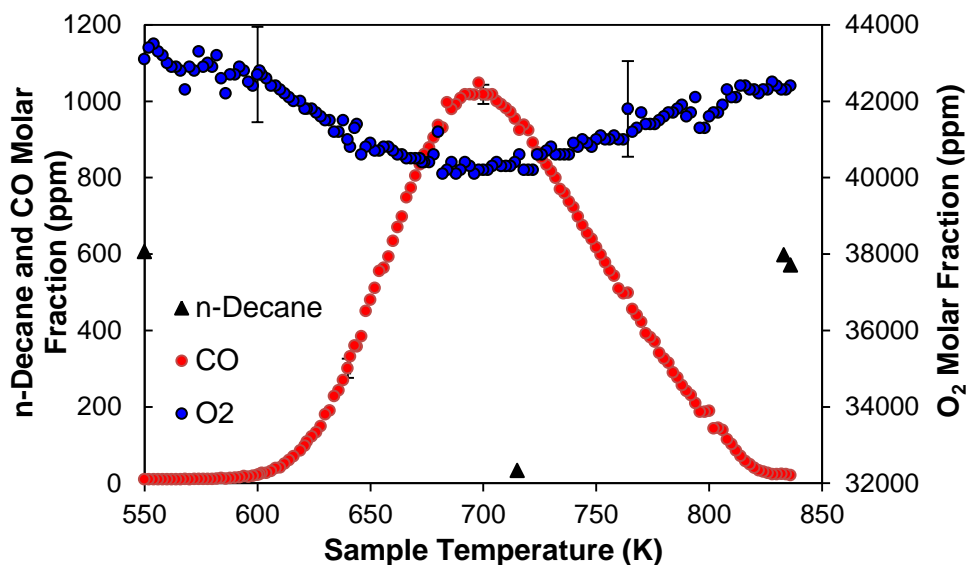


Figure 5-5: Fuel, CO, and O<sub>2</sub> profiles during *n*-decane oxidation; 8 atm; 120 ms; initial fuel fraction  $592 \pm 19$  ppm. CO<sub>2</sub> not recorded during the experiment. Experimental uncertainties:  $\pm 25$  ppm for CO and  $\pm 1250$  ppm for O<sub>2</sub>.

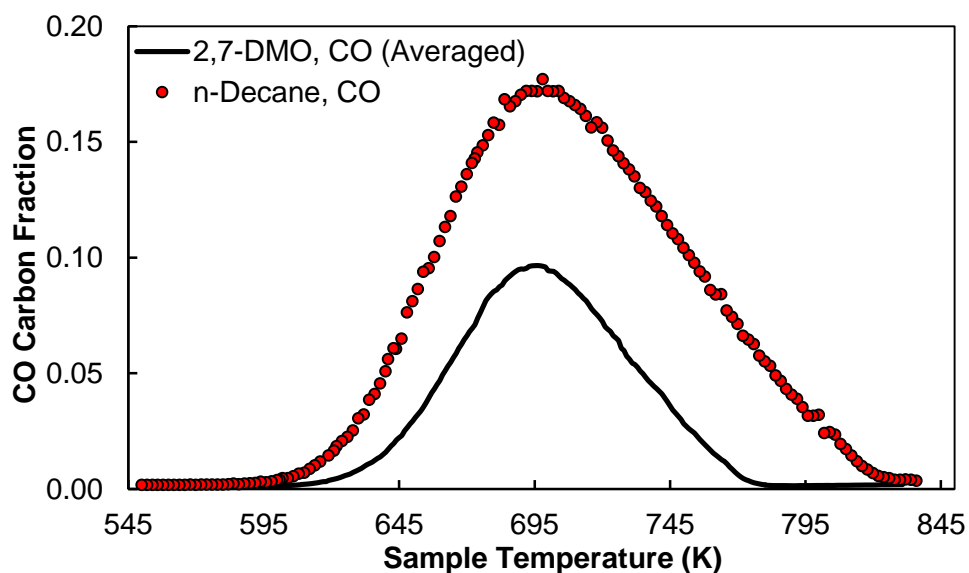
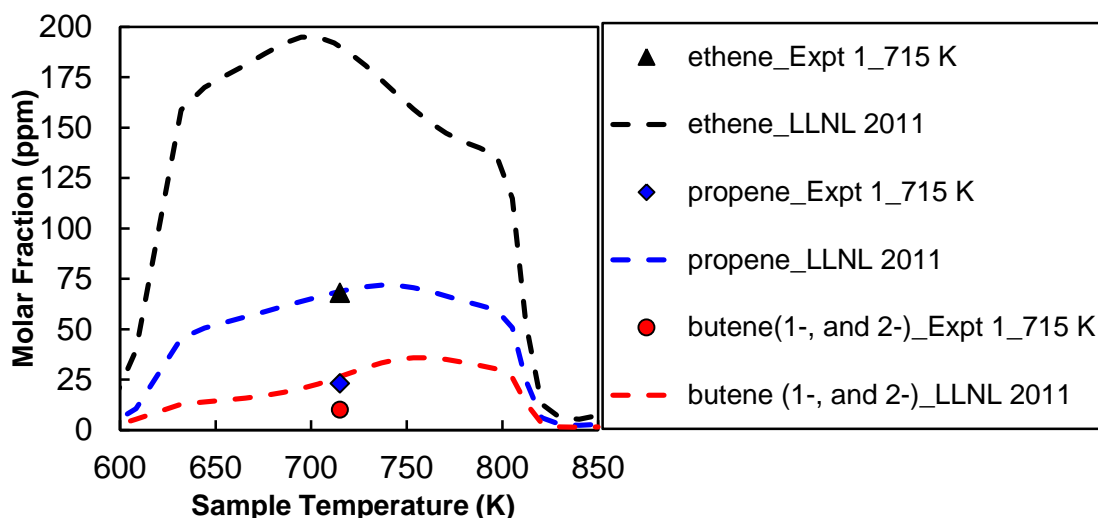


Figure 5-6: Carbon fraction for CO during the oxidation of *n*-decane and the average carbon fraction for CO during the replicate oxidation runs with 2,7-DMO.



**Figure 5-7: Predicted molar fraction of major alkenes produced during the oxidation of *n*-decane vs. measured alkenes at 715 K sample temperature; Model: LLNL 2011; 592 ppm initial *n*-decane molar fraction; residence time 120 ms, pressure 8 atm.**

#### 5.4 Details of the Model Calculations

The PFR oxidation data for 2,7-DMO was compared against the computations of Li *et al.* model (see Section 5.5). Details about the mechanism can be found in Section 4.2.

Unless otherwise noted, simulations were run at 10 K intervals over the inlet temperature range of 550 – 850 K. The model was exercised in CHEMKIN-PRO using the plug flow reactor module. An ROP analysis was performed for CO, CO<sub>2</sub>, ethene, propene, 2-butene and *iso*-butene at inlet temperatures of 630, 680, 740, and 840 K. Normalized ROP's of at least  $\pm 0.01$  were considered significant for this analysis. The reaction numbers refer to the sequence in the input files and can be looked up in the “gas-phase kinetics output” file. In addition to a numbered list of species and reactions, the file will contain the pre-exponential factor ( $A$ ), temperature exponent ( $\beta$ ), and activation energy ( $E$ ) values for each Arrhenius equation.

The sensitivity analysis was performed for CO<sub>2</sub>, ethene, and propene at selected inlet temperature(s). For sensitivity analysis figures in section 5.5, the “maximum sensitivities” number under the “preferences” tab in reaction path analyzer was set to 16, meaning that only the reactions with 16 largest normalized A-factor sensitivities will be displayed. Additional details on input parameters for simulations in CHEMKIN-PRO can be found in Section 4.3.

The Li *et al.* model uses a conventional naming methodology, also used in various LLNL mechanisms, to name the species. The four possible carbon sites, shown in Figure 5-8, are denoted alphabetically by a, b, c, and d. The alkyl radicals are named based on the H-abstraction site. For example, an H-abstraction from carbon site “a” will produce 2,7-dimethyl-1-octyl radical. Similarly, 2,7-dimethyl-3-octyl radical is formed by H-abstraction from carbon site “c” in the fuel structure. Table 5-3 shows the notation used in the model to call for various 2,7-dimethyloctyl radicals as well as several major intermediate species that are frequently referred to in section 5.5.

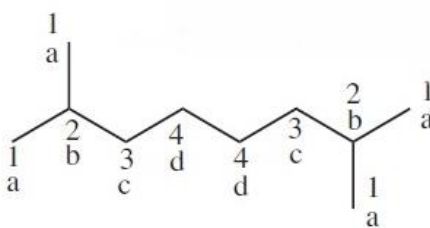


**Figure 5-8: Labeling of carbon sites in the structure of 2,7-DMO.**

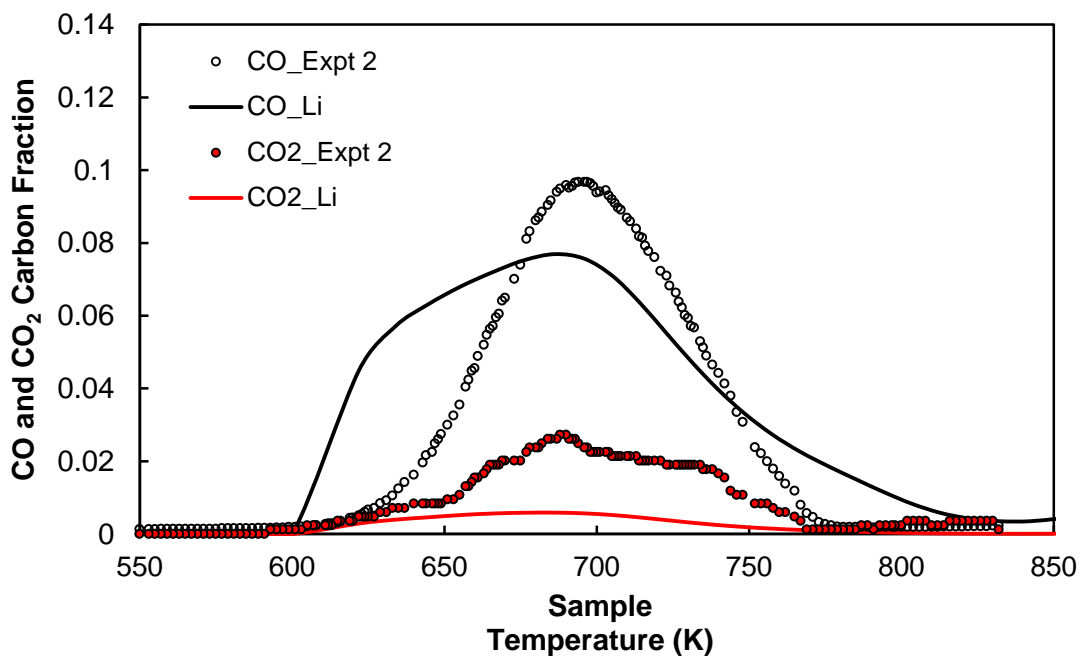
**Table 5-3: The notation used in Li *et al.* model for several key species.**

Species Name	Chemical Formula	Notation Used in Li <i>et al.</i> Model
Formaldehyde	CH <sub>2</sub> O	ch <sub>2</sub> o
Acetaldehyde	C <sub>2</sub> H <sub>4</sub> O	ch <sub>3</sub> cho
Acetone	C <sub>3</sub> H <sub>6</sub> O	ch <sub>3</sub> coch <sub>3</sub>
Ethene	C <sub>2</sub> H <sub>4</sub>	c <sub>2</sub> h <sub>4</sub>
Propene	C <sub>3</sub> H <sub>6</sub>	c <sub>3</sub> h <sub>6</sub>
1-Butene	C <sub>4</sub> H <sub>8</sub>	c <sub>4</sub> h <sub>8</sub> -1
2-Butene	C <sub>4</sub> H <sub>8</sub>	c <sub>4</sub> h <sub>8</sub> -2
iso-Butene	C <sub>4</sub> H <sub>8</sub>	ic <sub>4</sub> h <sub>8</sub>
3-Methyl-1-butene	C <sub>5</sub> H <sub>10</sub>	cc <sub>5</sub> h <sub>10</sub>
2,7-DMO	C <sub>10</sub> H <sub>22</sub>	c <sub>10</sub> h <sub>22</sub> -27

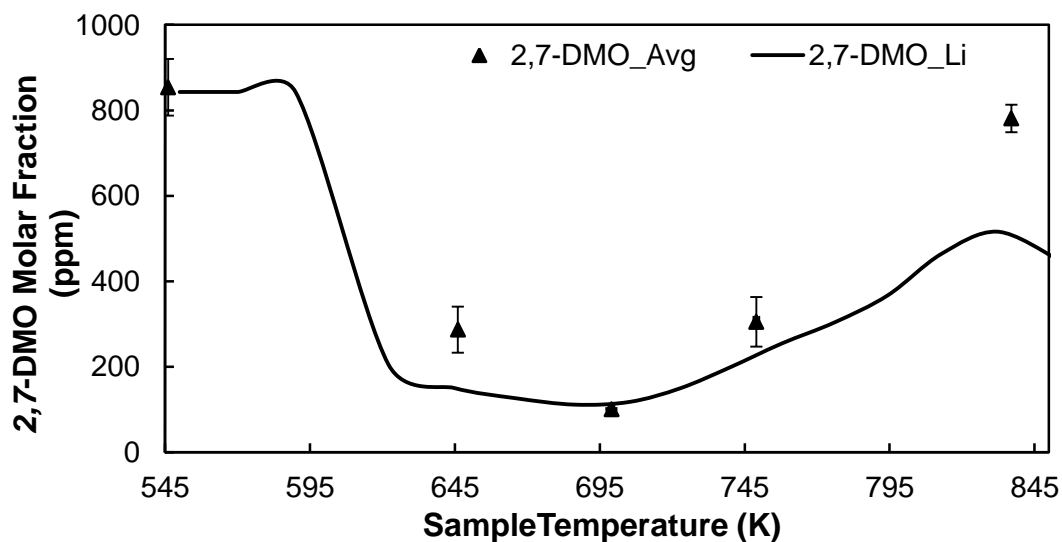
### 5.5 Modeling Results and Comparison with Experiments

Figure 5-9 displays the comparison between the data from Expt 2 and predictions of the Li *et al.* model. The start of NTC region at 685 K agreed fairly well with the measurements, with a calculated CO molar fraction of approximately 650 ppm, accounting for ~ 8% of the carbon input. The model predicted an earlier start of CO production and much higher levels in the lower temperature regime than seen in the experiments. A large disparity was observed between the measured and calculated CO<sub>2</sub> profile, where the model under-predicted the maximum CO<sub>2</sub> level by a factor of ~ 5. The model performed well in capturing the fuel consumption profile, as seen in Figure 5-10

with the exception of 837 K sample temperature, where experimental measurements indicated complete fuel recovery and cease of reactivity.



**Figure 5-9: CO and CO<sub>2</sub> during the oxidation of 2,7-DMO: experiments versus the computations of Li *et al.* model. For simulations, the averaged reactants' composition of 843 ppm 2,7-DMO / 42,100 ppm O<sub>2</sub> / 957,057 ppm N<sub>2</sub> was used.**



**Figure 5-10: Molar fraction of 2,7-DMO during the oxidation run: Averaged data from three replicate experiments vs. the predictions of Li *et al.* model.**



As displayed in Figure 5-11, the model deviated in calculating the profiles of C<sub>2</sub>-C<sub>4</sub> alkenes produced from the oxidation of 2,7-DMO. While measurements indicated that alkenes peak during the NTC region, the model predicted the peak production to occur at temperatures close to or before the start of this regime. In addition, the computed levels significantly deviated from the measurements. The mechanism over-predicted the propene and butene peak production levels by factors of ~ 3 and ~ 2, respectively. The model significantly over-predicted the peak production of ethene, i.e. by a factor of ~ 9. The calculated order of peak molar fraction of C<sub>2</sub>-C<sub>4</sub> alkenes was propene > butene > ethene. The measured order of peak molar fraction of these species was butene > propene > ethene. The unsatisfactory performance of the mechanism in predicting the trends and levels in the studied regime suggests that an alternative description of low temperature C<sub>2</sub>-C<sub>4</sub> chemistry is required. Figure 5-11 also plots the calculated *iso*-butene and 2-butene profiles to show the relative contribution each isomer to the overall calculated levels for butene. The calculated 1-butene levels were negligible. As shown, 2-butene accounted for about 67 % of total C<sub>4</sub> alkene mole fraction at peak production, i.e. at sample temperature of 620 K. Only at temperatures higher than 800 K, *iso*-butene levels were higher than those for 2-butene.

Figures 5-12 through 5-14 present the comparisons between measured and calculated profiles for 3-methyl-1-butene, formaldehyde, acetaldehyde, and acetone. Formaldehyde and acetaldehyde profiles are shown together. Also, to reduce the computational time, simulations were run at 20 K intervals. The model captured the trends for 3-methyl-1-butene and acetone fairly well. Formaldehyde was the dominant intermediate measured during the experiments, accounting for about 36 % of carbon balance at 699 K sample

temperature. At peak production, i.e. near 700 K, the Li *et al.* model predicted a level ~ 7 times lower. In contrast, the acetaldehyde levels were over-predicted by a factor of ~ 5.

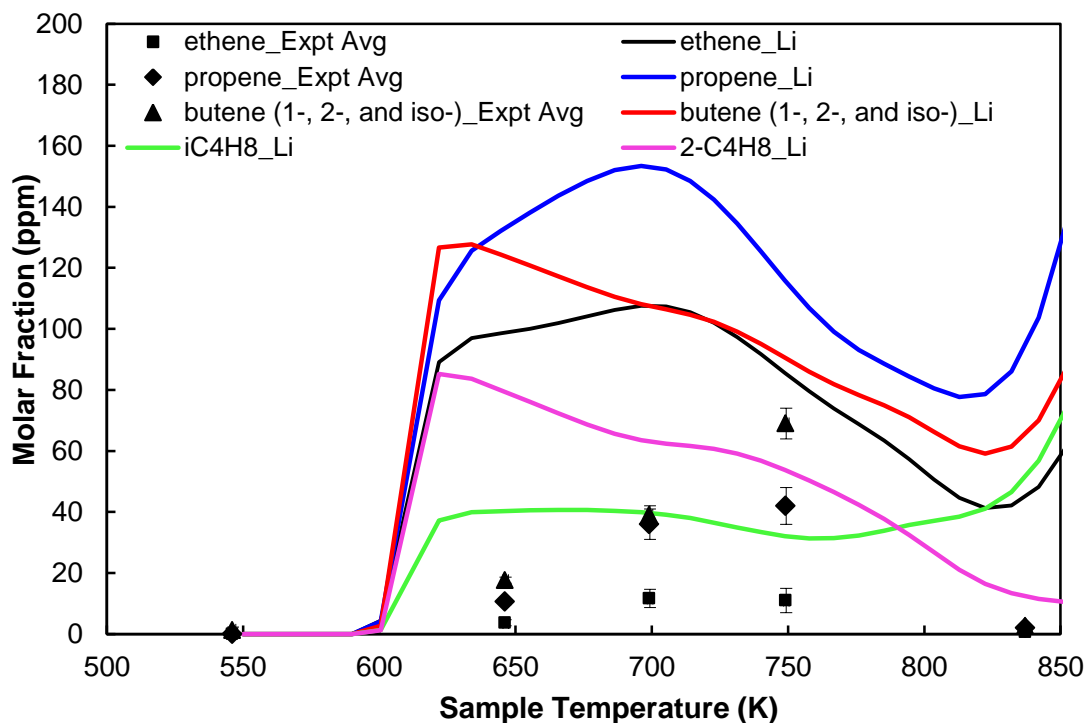


**Figure 5-11: Molar fraction of C<sub>2</sub>-C<sub>4</sub> alkenes produced during the oxidation of 2,7-DMO: Averaged data from three replicate experiments vs. the predictions of Li *et al.* Model.**

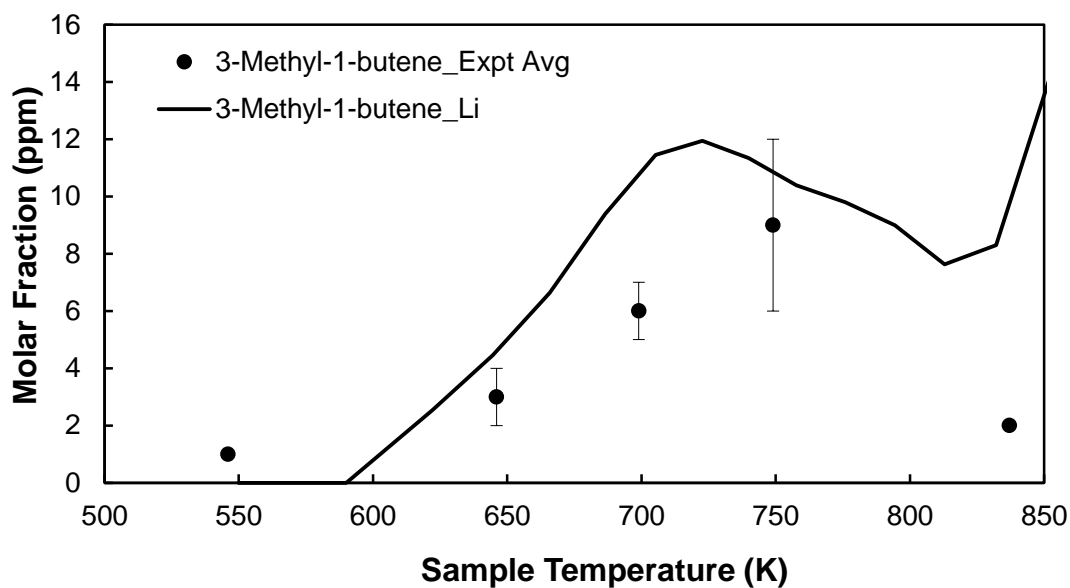


**Figure 5-12: Molar fraction of 3-methyl-1-butene produced during the oxidation of 2,7-DMO: Averaged experimental data vs. the predictions of Li *et al.* model.**

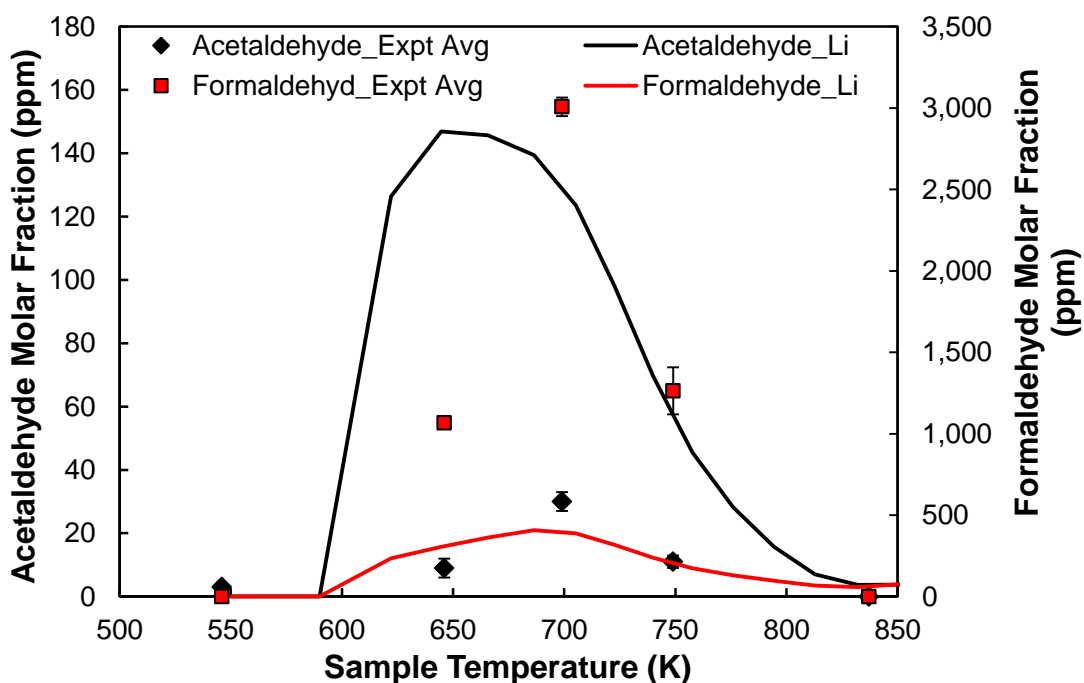


**Figure 5-13: Molar fraction of formaldehyde and acetaldehyde produced during the oxidation of 2,7-DMO: Averaged data from three replicate experiments vs. the predictions of Li *et al.* model.**

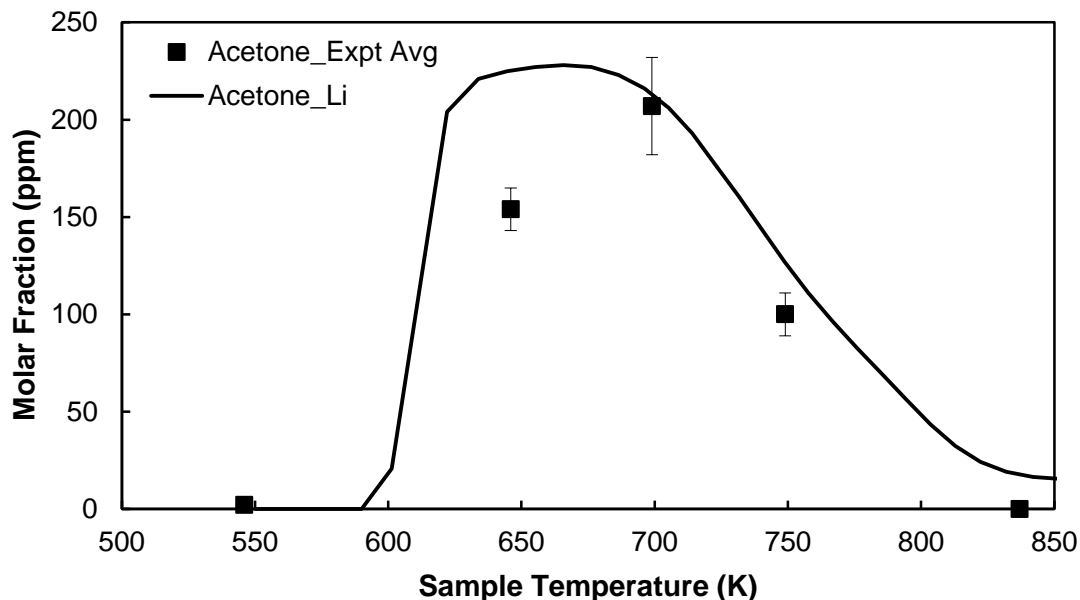


**Figure 5-14: Molar fraction of acetone produced during the oxidation of 2,7-DMO: Averaged data from replicate experiments vs. the predictions of Li *et al.* model.**

An ROP analysis was performed for CO, CO<sub>2</sub>, ethene, propene, 2-butene and *iso*-butene. The ROP analysis was conducted at inlet temperatures of 630, 680, 740, and 840 K. The calculated end point temperatures are: 645, 696, 749, and 842 K, closely representing four of the sample extraction temperatures. The highest temperature rise occurs for inlet temperature of 680 K with a calculated CO molar fraction of 637 ppm. An ROP analysis was not conducted at the 550 K, since the concentration of stable intermediates is insignificant at this temperature and therefor, an ROP analysis will not be valuable.

The results of ROP analysis for CO are shown in Figure 5-15. The y-axis presents the significant reactions that produce or consume CO. The x-axis shows the normalized ROP values for these reactions at the studied temperatures. At each temperature point, for a reaction that produced CO, the normalized ROP value was calculated by dividing the rate

of production of CO (in mol/cm<sup>3</sup>.s) by its total rate of production (also in mol/cm<sup>3</sup>.s). Likewise, for a reaction that consumed CO, the normalized ROP value was calculated by dividing the rate of consumption of CO in that reaction by the overall rate of consumption of CO. Therefore, the normalized ROP values range from -1 to 1. The analysis revealed that the reaction of formyl (HCO) with O<sub>2</sub> to produce CO and hydroperoxy (HO<sub>2</sub>) (i.e. R31) had the highest normalized positive ROP value at all the studied temperatures, reaching a value of 0.51 at the inlet temperature of 680 K. Decomposition of acetyl (CH<sub>3</sub>CO) radical to a methyl (CH<sub>3</sub>) radical and CO (i.e. R257) is the second most significant reaction that produces CO at inlet temperatures of 630, 680, and 740 K. At all of the studied temperatures, the main reaction depleting CO was the reaction of CO with hydroxyl (OH) radical to produce CO<sub>2</sub> and H (i.e. R27/28). The normalized ROP value of this reaction was in the range of -0.92 to -0.77. Reaction R31 was also identified as the main reaction producing CO during the oxidation of *n*-decane, based on an examination of LLNL 2011 model at identical conditions. For the latter mechanism, the second key reaction that produced CO was addition of O<sub>2</sub> to vinyloxy (CH<sub>2</sub>CHO) radical to produce formaldehyde (CH<sub>2</sub>O), CO, and hydroxyl (OH). This reaction (i.e. R273) was insignificant in Li *et al.* model for 2,7-DMO. In both mechanisms, reaction R27/28 was the dominant reaction consuming CO. Still, as displayed in Figure 5-16, this reaction was not the primary source of CO<sub>2</sub> formation at the studied temperatures. Among the handful of key reactions affecting the molar fraction of CO<sub>2</sub>, oxidization of HCCO to produce CO and CO<sub>2</sub> (i.e. R293) had a significant normalized positive ROP value at all the studied temperatures. The only reaction that accounted for depletion of CO<sub>2</sub> was the reaction of CH<sub>2</sub> with CO<sub>2</sub> to form formaldehyde

and CO, which has an almost negligible associated absolute rate of production when compared with the reactions producing CO<sub>2</sub> (e.g.  $-7.58 \times 10^{-17}$  mol/cc.sec at 680 K versus  $7.54 \times 10^{-9}$  mol/cc.sec for reaction R43 at 680 K).

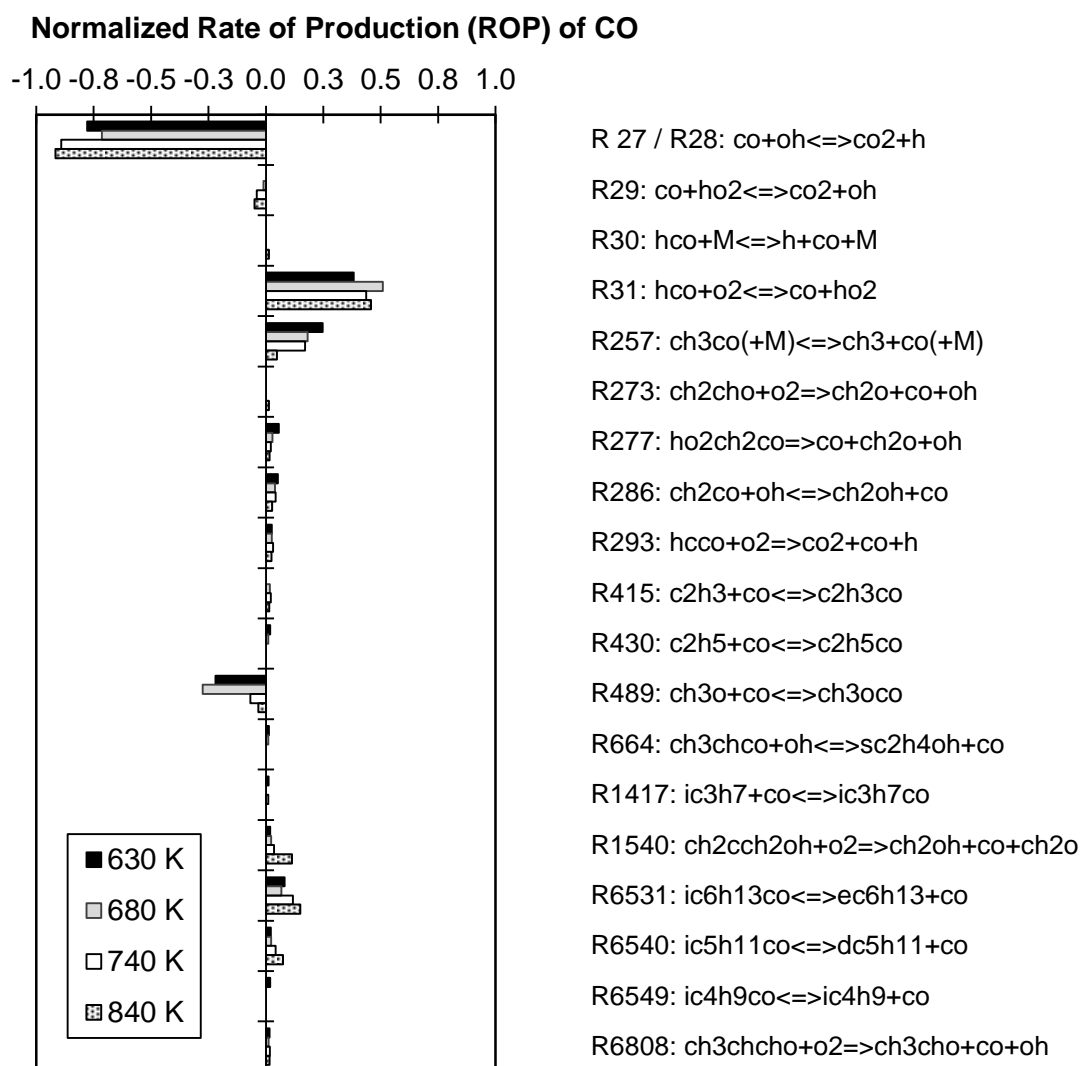


**Figure 5-15: Normalized Rates of Production for reactions affecting the molar fraction of CO at selected inlet temperatures: Li *et al.* model for 2,7-DMO.**

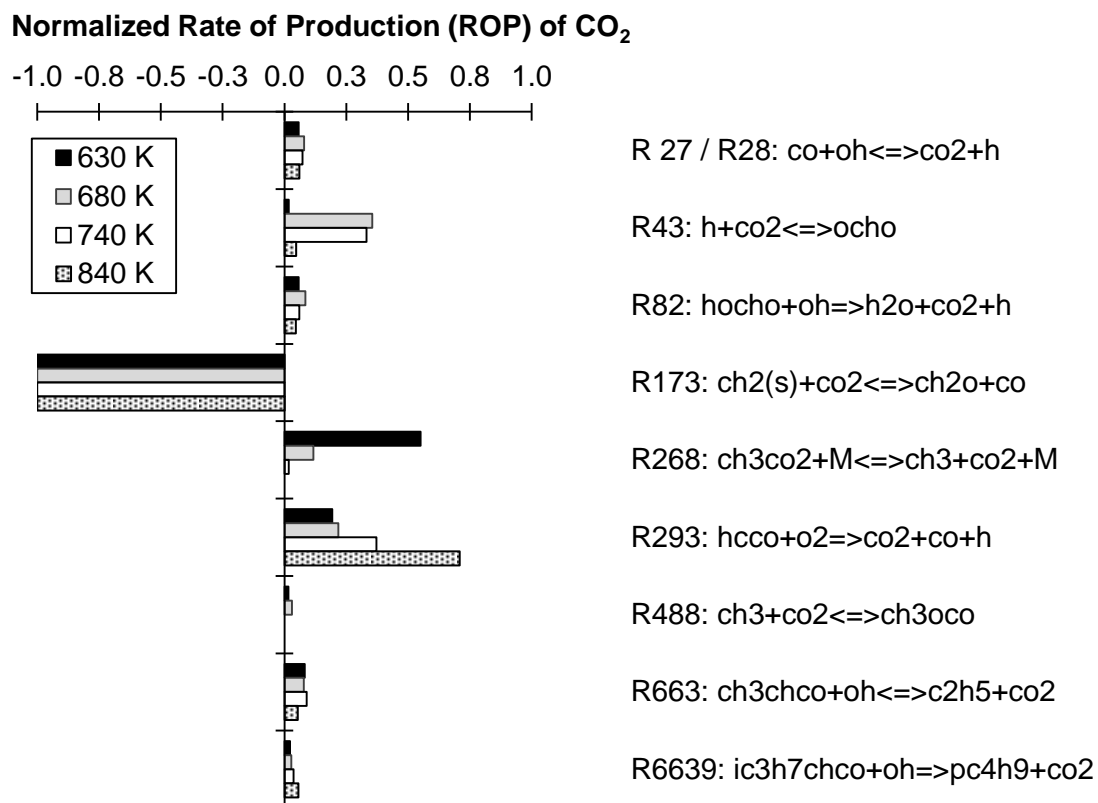


**Figure 5-16: Normalized Rates of Production for reactions affecting the molar fraction of CO<sub>2</sub> at selected inlet temperatures: Li *et al.* model for 2,7-DMO.**

As shown in Figures 5-17 through 5-20, several  $\beta$  scission reactions of C<sub>5</sub> and C<sub>6</sub> alkyl radicals significantly contributed to the formation of C<sub>2</sub> – C<sub>4</sub> alkenes. A beta-scission reaction is one in which a carbon-carbon bond breaks at the second bond site from the radical site. As depicted in Figure 5-19,  $\beta$  scission reaction of bC<sub>6</sub>H<sub>13</sub> radical (i.e. R6707) to generate *iso*-butene and ethyl radical had a normalized ROP value as high as 0.56 at the inlet temperature of 630 K. At all the studied temperature, 2-butene was primarily produced from  $\beta$  scission reaction of cC<sub>5</sub>H<sub>11</sub> radical, i.e. R6682, also forming methyl radical. For ethene, the recombination reaction of C<sub>2</sub>H<sub>5</sub> radical with O<sub>2</sub> (i.e. R222) as well decomposition of ethylperoxy (C<sub>2</sub>H<sub>5</sub>O<sub>2</sub>) (i.e. R228) also contributed

significantly to the formation of this species. For these alkenes, recombination reactions with OH, H, O, and HO<sub>2</sub> radicals constituted the key consumption pathways.

At the inlet temperature of 840 K, the reactions  $C_2H_4 + CH_3 \rightleftharpoons C_2H_3 + CH_4$  and  $C_3H_6 + CH_3 \rightleftharpoons iC_4H_9$  accounted for 29 % of formed ethene and 25 % of formed propene, respectively. At the same temperature, 70 % of *iso*-butene was produced through  $\beta$  scission reaction of C<sub>10</sub>H<sub>21</sub>-27b radical (i.e. R5962), also producing eC<sub>6</sub>H<sub>13</sub> radical. These reactions are the likely reason for the sudden increase in ethene, propene, and *iso*-butene levels at temperatures higher than 820 K. The species 5-methyl-1-hexene was among the key alkenes measured at 749 K sample temperature, suggesting that the  $\beta$  scission reaction of C<sub>10</sub> alkyl radical is also significant at lower temperatures and during the NTC region.



### Normalized Rate of Production (ROP) of Ethene

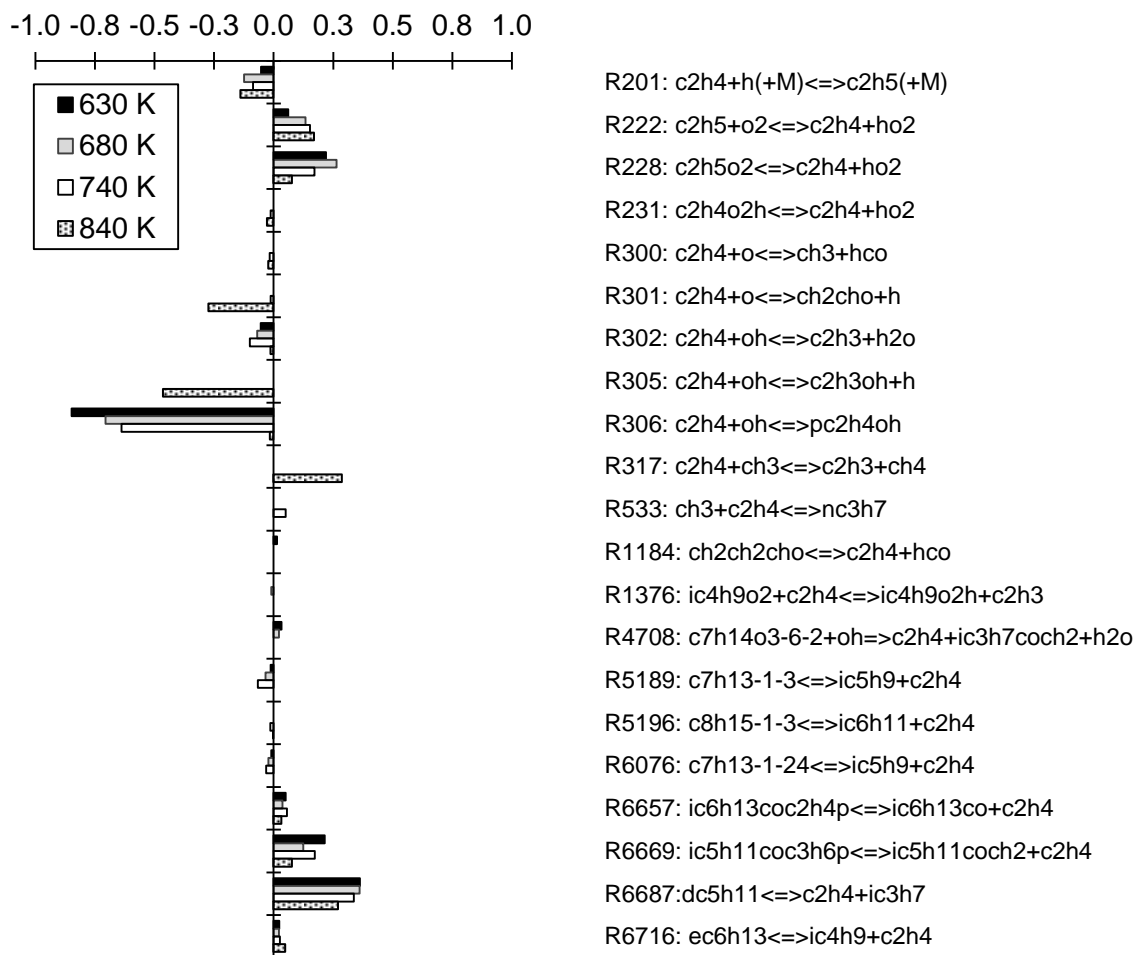


**Figure 5-17: Normalized Rates of Production for reactions affecting the molar fraction of ethene at selected inlet temperatures: Li *et al.* model for 2,7-DMO.**

### Normalized Rate of Production (ROP) of Propene

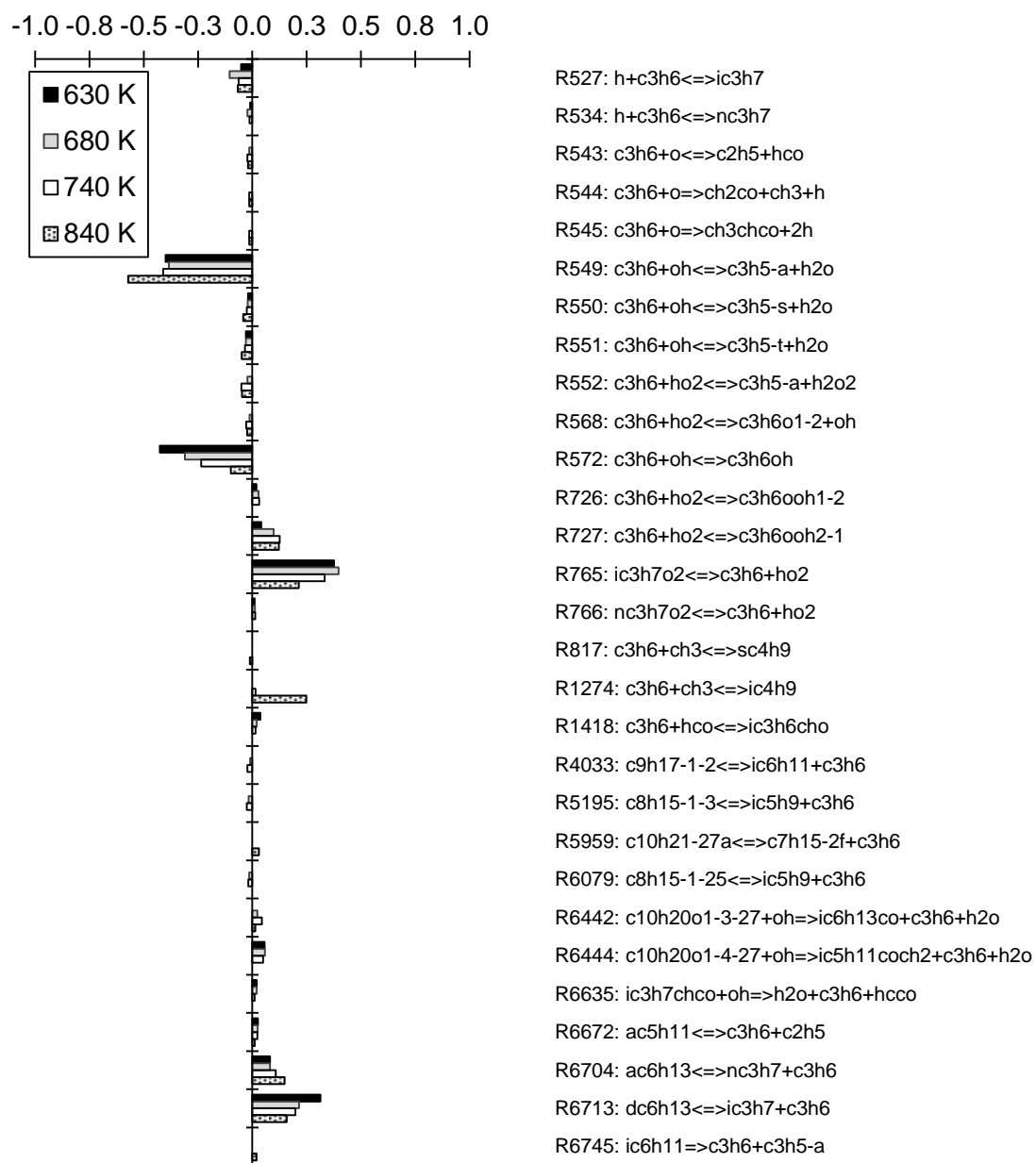


**Figure 5-18: Normalized Rates of Production for reactions affecting the molar fraction of propene at selected inlet temperatures: Li *et al.* model for 2,7-DMO.**

### Normalized Rate of Production (ROP) of *iso*-Butene

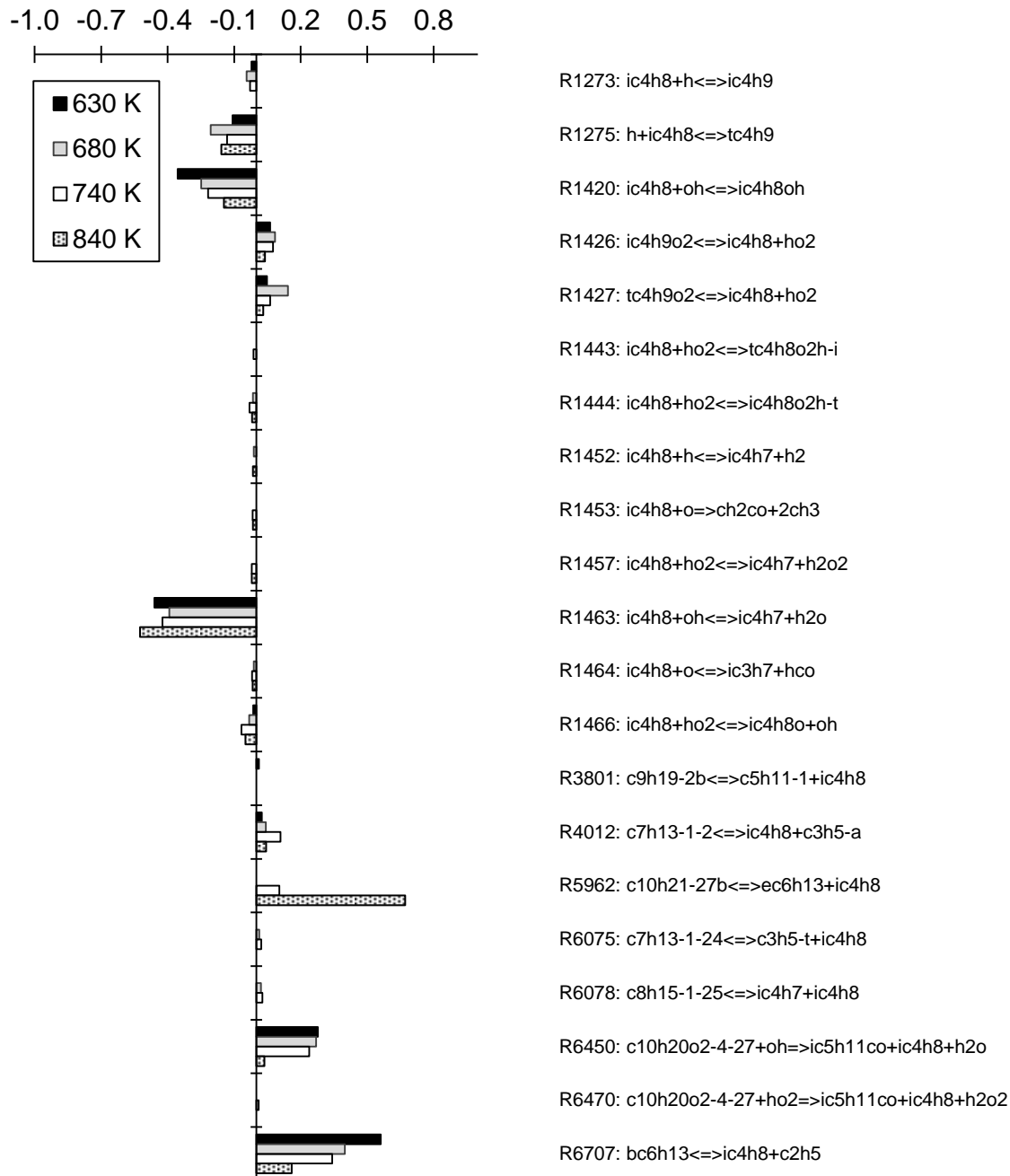


**Figure 5-19: Normalized Rates of Production for reactions affecting the molar fraction of *iso*-butene at selected inlet temperatures: Li *et al.* model for 2,7-DMO.**

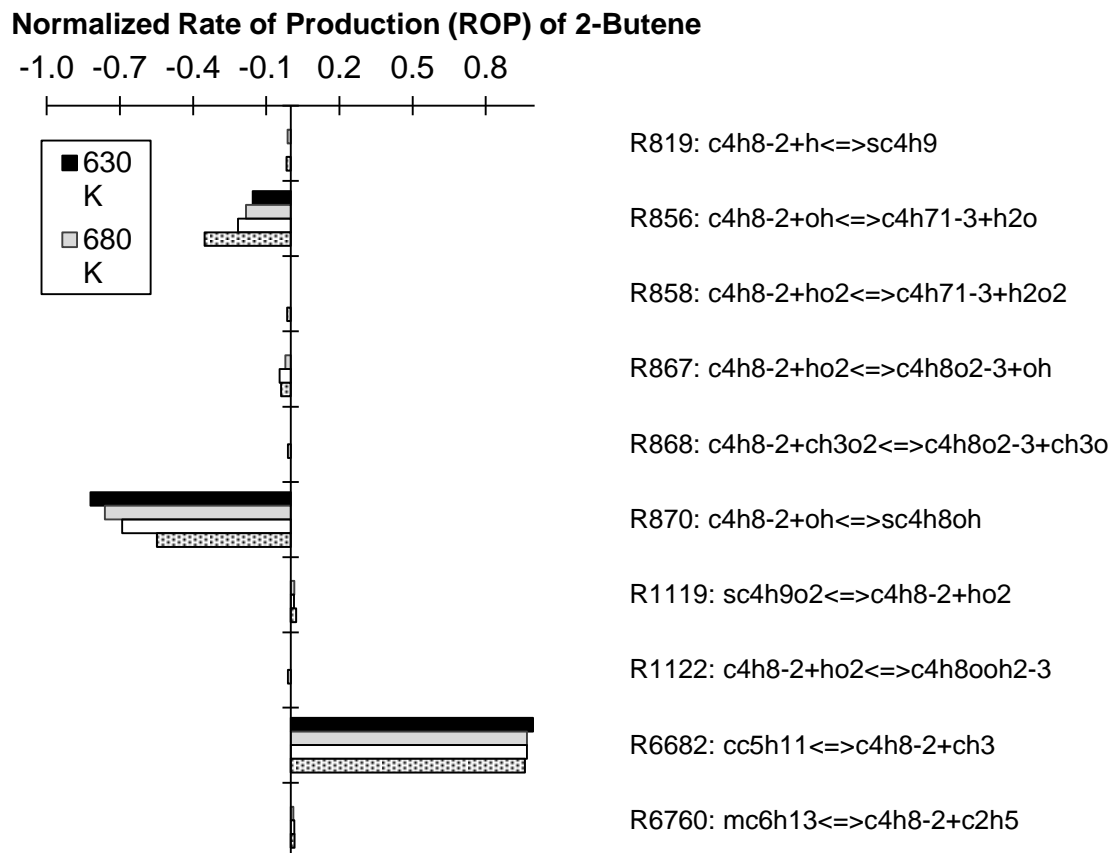


**Figure 5-20: Normalized Rates of Production for reactions affecting the molar fraction of 2-butene at selected inlet temperatures: Li *et al.* model for 2,7-DMO.**

To further investigate model's predictions for the  $C_{10}$  dimethyl alkyl radical and relative importance of key reaction pathways, e.g.  $\beta$  scission reactions and  $\cdot RO_2$  chemistry, in production of major intermediate species, a reaction flux analysis was performed at the inlet temperature of 670 K, corresponding to a sample temperature of ~686 K. This temperature is closely associated with peak production of species such as CO,  $CO_2$ , formaldehyde, acetone, ethene, and propene. The simplified diagram, with only key production pathways for CO,  $CO_2$ , formaldehyde, and acetone, are presented in Figures 5-21 and 5-22. The reaction flux analysis indicated the importance of  $RO_2$  chemistry in final yields of these species. The flux is initiated by H-abstraction reaction

from parent fuel to generate 2,7-dimethyl-octyl radicals. About 90 % of parent fuel is consumed by OH mediated H-abstraction reaction from a, b, c, and d carbon sites. Only about 6 % of fuel is predicted to convert to 2,7-dimethyl-octyl radicals via H-abstraction reactions by HO<sub>2</sub> radical. About 50% of the alkyl radical (conventionally denoted by R) follows the critical branching pathway for low temperature oxidation and will undergo molecular oxygen addition to form alkylperoxy radical, RO<sub>2</sub>. Depending on the H-abstraction site, about 10 – 21 % of alkylperoxy radical isomerizes to form the alkylhydroperoxy radical (e.g. C<sub>10</sub>OOH3-27e). Further molecular oxygen addition produces the peroxyalkylhydroperoxy radical (C<sub>10</sub>OOH3-OO5-27). Decomposition produces a hydroxyl radical and a ketohydroperoxide (e.g. C<sub>10</sub>ket3-5-27), which decomposes to produce a second hydroxyl radical and other species.

The flux analysis indicated that a major source for production of CO, CO<sub>2</sub>, formaldehyde, and acetaldehyde is the iC<sub>5</sub>H<sub>11</sub>COCH<sub>2</sub> radical which is formed through subsequent reactions of 2,7-dimethyl-1-, 2,7-dimethyl-3-, and 2,7-dimethyl-4-octyl radicals. The subsequent reactions of this radical have a significant effect of the final yield of these species. In fact, as shown in Figure 5-22 two of the most significant reactions producing each of the CO, CO<sub>2</sub>, formaldehyde, and acetaldehyde species, back track to iC<sub>5</sub>H<sub>11</sub>COCH<sub>2</sub> radical. The flux analysis also demonstrates the close coupling between the key production pathways for the major intermediate species. For example, CH<sub>3</sub>CO is the primary source for methyl radical. As seen, CH<sub>3</sub>CO is mostly produced via reactions of acetaldehyde. Methyl recombination reaction with O<sub>2</sub>, followed by addition of HO<sub>2</sub>, results in production of CH<sub>3</sub>O<sub>2</sub>H, which is in turn the primary source of formaldehyde. Formaldehyde and acetaldehyde were under-predicted and over-predicted

by Li *et al.* model, respectively. The educated adjustment of rate parameters for reactions involving the flux of acetaldehyde to formaldehyde can significantly enhance the predictions of the model. Higher flux of acetaldehyde to methyl will also translate to higher levels of CO produced, which is slightly under-predicted by the Li *et al.* model.

The key pathways for production of CO and CO<sub>2</sub> are related, but not largely affected by one another. For example, the O<sub>2</sub> addition reaction to HCCO radical which produces both CO and CO<sub>2</sub> (i.e. R293), has the highest normalized ROP value with respect to CO<sub>2</sub>. However, it only slightly contributes to production of CO. Also, the preceding reaction to R293 in the reaction flux analysis, i.e. reaction  $\text{CH}_2\text{CO} + \text{OH} \rightleftharpoons \text{HCCO} + \text{H}_2\text{O}$ , shows a significant positive normalized sensitivity with respect to CO<sub>2</sub>, as seen in Figure 5-23. For a sensitive reaction, a change in the rate coefficient will cause a significant change in the overall reaction rate. A positive sensitivity value is indicative of a reaction that enhances CO<sub>2</sub> production, while a negative value corresponds to a reaction that impedes CO<sub>2</sub> formation. In other words, increasing the rate of this reaction will enhance the production of CO<sub>2</sub>, without having a necessarily sizable effect on CO yields. Another example is reaction R43 which accounts for about 35% of CO<sub>2</sub> formed at the inlet temperature of 680 K. Only 2% of formaldehyde will be consumed in order to initiate the reactions leading to R43 and eventually the formation CO<sub>2</sub>. Therefore, tuning the rate parameters for this reaction can possibly increase the CO<sub>2</sub> yield with only consuming a small amount of formaldehyde.

Acetone is primarily produced via subsequent reactions of 2,7-dimethyl-2-octyl and 2,7-dimethyl-3-octyl radical, earlier in reaction sequence, in comparison to other major

oxygenates. Not shown in the figure, are recombination reactions with OH radical that account for key consumption pathways for acetone.

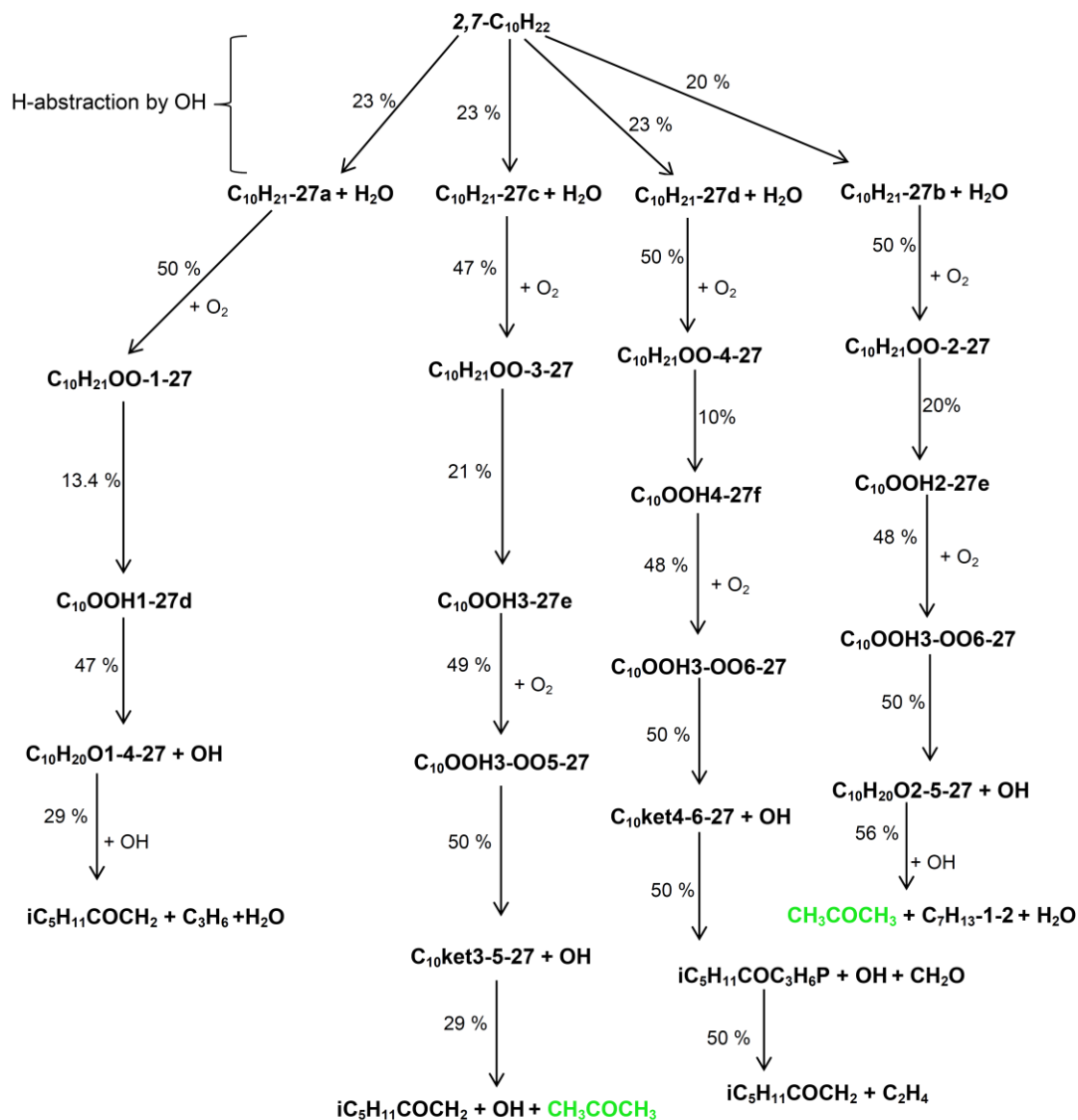


**Figure 5-21: Reaction flux analysis for 2,7-DMO oxidation with an emphasis on reactions leading to the formation of iC<sub>5</sub>H<sub>11</sub>COCH<sub>2</sub> radical and acetone; Li *et al.* model, inlet temperature 670 K, pressure 8 atm, residence time 120 ms.**

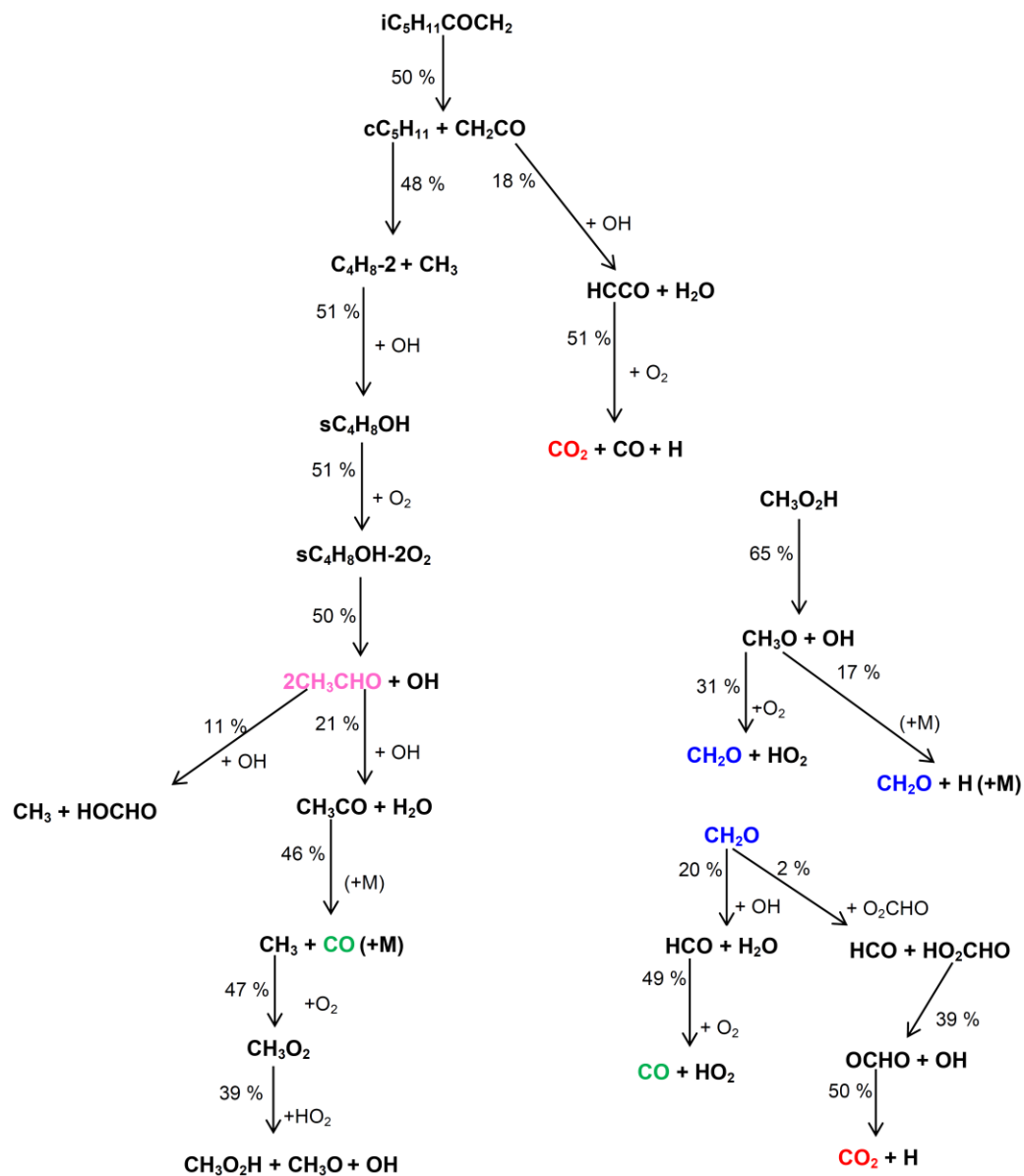


**Figure 5-22: Reaction flux during 2,7-DMO oxidation with an emphasis on reactions leading from  $iC_5H_{11}COCH_2$  to CO, CO<sub>2</sub>, formaldehyde, acetaldehyde; Li *et al.* model, inlet temperature 670 K, pressure 8 atm, residence time 120 ms.**



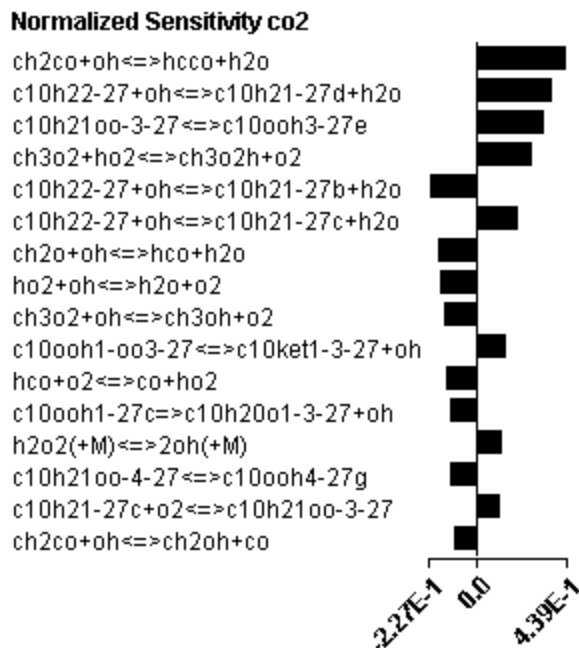


**Figure 5-23: The most sensitive reactions with respect to CO<sub>2</sub>; inlet temperature 680 K; pressure 8 atm, residence time 120 ms; Li *et al.* model.**

Figures 5-24 and 5-25 present the normalized A-factor sensitivities for the most sensitive reactions with respect to ethene and propene, respectively. The analysis was carried out for the inlet temperatures of 680 K (corresponding to a sample temperature of 696 K) and 750 K (corresponding to a sample temperature of 757 K). These two temperature points were chosen as they closely represent the calculated and measured peak temperature points, respectively. For both studied temperatures, the H-abstraction reaction from the d carbon site had the highest positive sensitivity values. This is expected for ethene, as the earlier discussed reaction flux analysis clearly demonstrated the flux of 2,7-dimethyl-4-octyl radical to ethene. For ethene, reaction  $C_2H_4 + OH \rightleftharpoons pC_2H_4OH$  was the most sensitive reaction that enhanced the consumption of ethene. The earlier ROP analysis for ethene had indicated that for both 680 K and 740 K inlet temperatures about 70 % of ethene was consumed via this reaction. At the inlet temperature of 680 K,

approximately 50 % of  $pC_2H_4OH$  combines with OH to form  $O_2C_2H_4O$ , 50 % which later decomposes to form formaldehyde. Therefore, adjustment of the rate parameters for the reaction  $C_2H_4 + OH \rightleftharpoons pC_2H_4OH$  can both lower the ethene levels and increase the formaldehyde levels, improving the calculations of the model for both species. At both temperatures, the  $\beta$  scission reaction of  $bC_6H_{13}$  radical (i.e. R6707) to generate *iso*-butene and ethyl radical exhibited a considerable negative A-factor sensitivity with respect to propene. As demonstrated, *iso*-butene and propene distributions were poorly predicted by the model. A promising means to correct the miss-calculated distribution would be fine-tune the rate parameters for this reaction. Overall, the sensitivity analysis indicated the importance of H-abstraction reactions from parent fuel via OH as well as the  $\cdot RO_2$  chemistry in final determination of ethene and propene yields. Refinement of the rate parameters for the key reactions that fall within these two categories can enhance the predictions of the model for the distribution of these species. Overall, the analysis of Li *et al.* model showed that low temperature  $RO_2$  chemistry pathways are the favored reaction pathways by the mechanism for simulation of profiles of major intermediate species under the studied conditions. The reactions of  $RO_2$  radicals resulted in formation of high yields of oxygenates, consistent with the observations from the PFR study, where aldehydes and ketones peaked before the start of NTC region. However, the  $\cdot RO_2$  chemistry appears to be insufficient for accurate simulation of profiles of alkenes during the NTC regime. This is signified by observations from the PFR study, where alkenes peaked during the NTC. In this region, the ratio of R to  $\cdot RO_2$  increases and the formed alkyl radical proceeds to produce less reactive species including  $\cdot HO_2$  radicals and alkenes. In addition to refining the rate parameters for discussed key reactions pertaining

to  $\text{RO}_2$  chemistry, therefore, there is also a need for higher accounting of the influence of reactions of R radicals.

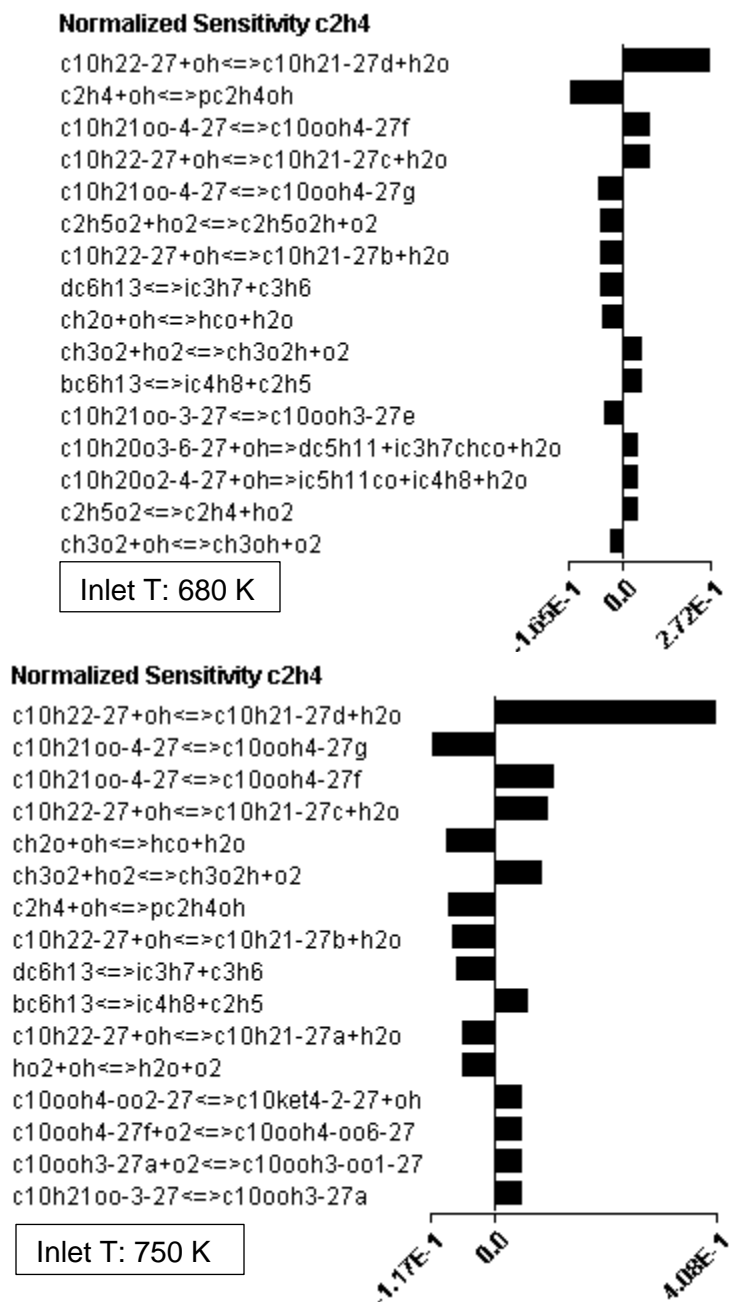


**Figure 5-24: Sensitive reactions with respect to ethene at inlet temperatures of 680 K and 750 K; pressure 8 atm, residence time 120 ms; Li *et al.* model.**

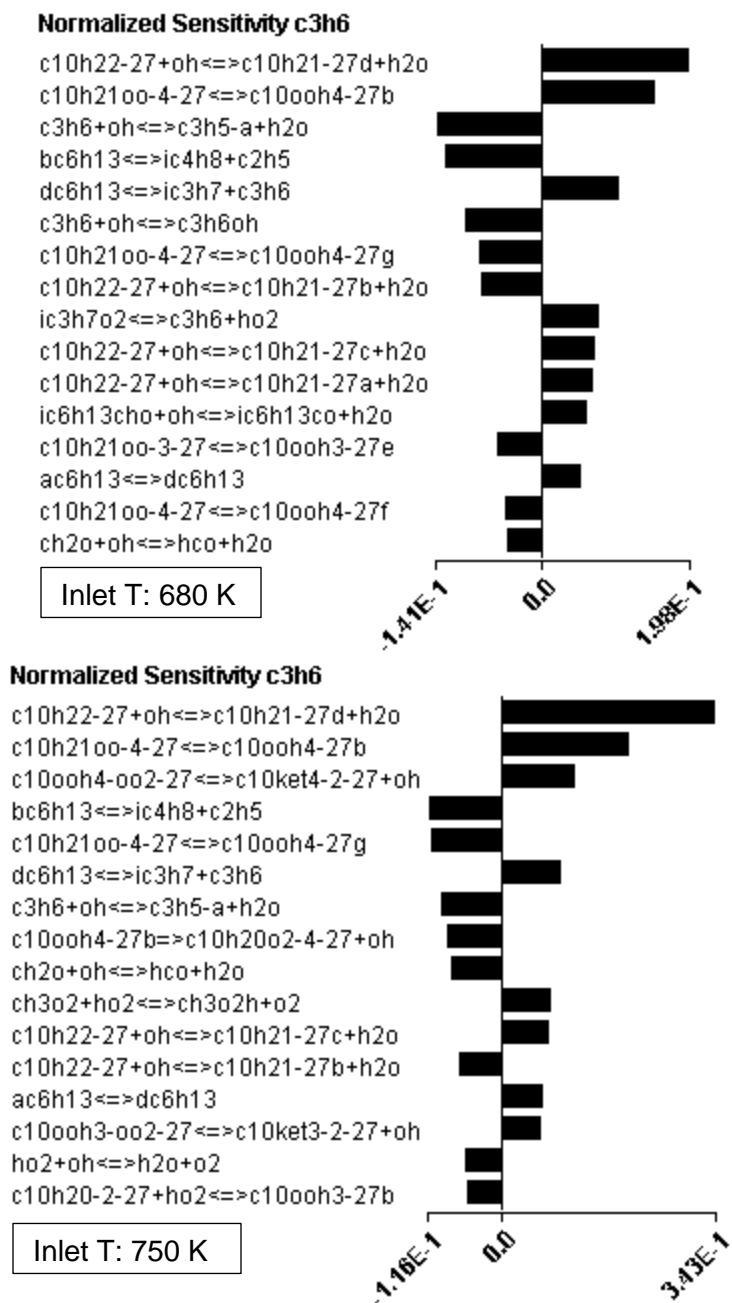


**Figure 5-25: Normalized A-factor sensitivities for the most sensitive reactions with respect to propene at inlet temperature of 680 K and 750 K; pressure 8 atm, residence time 120 ms; Li *et al.* model for 2,7-DMO.**

## 5.6 Initial Comparison of and Updated 2,7-Dimethyloctane Model with the PFR

### Data

Based on the reported experimental results and model analysis, a collaborative effort with Dr. Charles Westbrook (LLNL) was initiated to refine the model predictions in the low temperature and NTC regimes. The effort resulted in an updated version of the 2,7-DMO mechanism, denoted here as the modified Li *et al.* model. Several of the low temperature reaction classes (i.e. classes 11 – 30, listed in Section 4.2.3) were extensively modified. In particular, many rate parameters were updated based on recent publications. Also, alternative pathways for isomerization of the O<sub>2</sub>QOOH intermediate and formation of O<sub>2</sub>QOOH and formation of carbonylhydroperoxide and OH (i.e. class 27 and the added sub-classes of 27b, 27c, and 27d) were incorporated in the mechanism. These pathways required inclusion of new species and reactions. In addition, the A-factors for two sensitive reactions with respect to CO<sub>2</sub> were adjusted to increase the CO production levels, thus obtaining an improved agreement with the PFR data. The modified Li *et al.* model contains 1843 species and 7397 reactions, as opposed to 1599 species and 6833 reactions in the Li *et al.* model. The following provides a summary of the most significant changes to low temperature reaction classes:

1. The reaction rate constants for O<sub>2</sub> addition to alkyl (R) radicals (i.e. class 11, reaction  $R + O_2 = ROO$ ) were updated based on the work of Miyoshi *et al.* [64].
2. The A-factors for reactions involving the addition of alkyl radical (R) with alkylperoxy radical (RO<sub>2</sub>) to form two RO molecules (i.e. class 12, reaction  $R + RO_2 = RO + RO$ ) were changed from  $7.00 \times 10^{12} \text{ cm}^3 \text{ mol}^{-1} \text{ s}^{-1}$  to  $9.00 \times 10^{12} \text{ cm}^3 \text{ mol}^{-1} \text{ s}^{-1}$ .

3. The A-factors for reactions involving the addition of alkyl radical (R) with hydroperoxy radical ( $\text{HO}_2$ ) to form RO and OH (i.e. class 13, reaction  $\text{R} + \text{HO}_2 = \text{RO} + \text{OH}$ ) were changed from  $7.00 \times 10^{12} \text{ cm}^3 \text{ mol}^{-1} \text{ s}^{-1}$  to  $9.00 \times 10^{12} \text{ cm}^3 \text{ mol}^{-1} \text{ s}^{-1}$ .
4. The A-factors for reactions involving the addition of alkyl radical (R) with  $\text{CH}_3\text{O}_2$  to form RO and  $\text{CH}_3\text{O}$  (i.e. class 14, reaction  $\text{R} + \text{CH}_3\text{O}_2 = \text{RO} + \text{CH}_3\text{O}$ ) were changed from  $7.00 \times 10^{12} \text{ cm}^3 \text{ mol}^{-1} \text{ s}^{-1}$  to  $9.00 \times 10^{12} \text{ cm}^3 \text{ mol}^{-1} \text{ s}^{-1}$ .
5. The reaction rate constants for alkylperoxy radical ( $\text{RO}_2$ ) isomerization reactions (i.e. class 15, reaction  $\text{RO}_2 = \text{QOOH}$ ) were updated based on the work of Sharma *et al.* [65].
6. The reaction rate constants for concerted (direct) elimination of hydroperoxy radical ( $\text{HO}_2$ ) and alkene from alkylperoxy radicals ( $\text{RO}_2$ ) (i.e. class 16, reaction  $\text{RO}_2 = \text{alkene} + \text{HO}_2$ ) were updated based on the work of Villano *et al.* [66].
7. The A-factors and activation energies for the reactions belonging to class 21 (i.e.  $\text{ROOH} = \text{RO} + \text{OH}$ ) were changed.
8. The A-factors for the reactions belonging to class 22 (i.e. alkylperoxy radical (RO) decomposition) were changed.
9. The rate parameters for decomposition reactions of QOOH to form cyclic ether (QO) and OH (i.e. class 23) were updated based on the work of Villano *et al.* [67].  
In the Li *et al.* model the rate constants for this class of reactions followed the work of Meh *et al.* on iso-octane [68].
10. The work of Villano *et al.* [67] was also used to update the rate constants for decomposition of QOOH radicals with a radical site  $\beta$  to alkene and hydroperoxy

- (HO<sub>2</sub>) radical (i.e. class 24, QOOH = alkene + HO<sub>2</sub>) as well as the rate constants for decomposition of QOOH radicals with a radical site  $\gamma$  to alkene, carbonyl, and OH (i.e. class 25, QOOH = alkene + carbonyl + OH).
11. The rate parameters for addition of O<sub>2</sub> to QOOH radicals (i.e. class 26) were updated following the work of Miyoshi *et al.* [64].
  12. The reaction class 27 (isomerization of O<sub>2</sub>QOOH radical and formation of carbonylhydroperoxide and OH) was extensively modified based on the work of Sharma *et al.* [65]. Three sub-classes were added: concerted elimination of O<sub>2</sub>QOOH radicals to alkenyl hydroperoxide (class 27b, ref [66]), decomposition of dihydroperoxide (p(OOH)<sub>2</sub>) radicals (class 27c), and cyclic ether from p(OOH)<sub>2</sub> species (class 27d) (refs: Bugler *et al.* [69] and Villano *et al.* [67]).
  13. Decomposition reactions of carbonylhydroperoxide to form oxygenated radical species and OH (i.e. class 28) as well as cyclic ether reactions with OH and HO<sub>2</sub> (i.e. class 29) were updated. For example, the reaction C<sub>10</sub>H<sub>20</sub>O<sub>4</sub>-5-27 + OH = dC<sub>5</sub>H<sub>11</sub> + iC<sub>3</sub>H<sub>7</sub>CHCO + H<sub>2</sub>O was replaced with the reaction C<sub>10</sub>H<sub>20</sub>O<sub>4</sub>-5-27 + OH = iC<sub>4</sub>H<sub>9</sub> + iC<sub>4</sub>H<sub>9</sub>CHCO + H<sub>2</sub>O, virtually increasing the production of *iso*-butyl radical.
  14. The A-factor for reaction CH<sub>2</sub>CO + OH = HCCO + H<sub>2</sub>O was increased from 1.00 × 10<sup>13</sup> cm<sup>3</sup> mol<sup>-1</sup> s<sup>-1</sup> to 1.00 × 10<sup>14</sup> cm<sup>3</sup> mol<sup>-1</sup> s<sup>-1</sup> to increase CO<sub>2</sub> production. The A-factor for reaction CH<sub>2</sub>CO + OH = CH<sub>2</sub>OH + CO, which impedes CO<sub>2</sub> production, was decreased from 2.00 × 10<sup>12</sup> cm<sup>3</sup> mol<sup>-1</sup> s<sup>-1</sup> to 2.00 × 10<sup>11</sup> cm<sup>3</sup> mol<sup>-1</sup> s<sup>-1</sup>.

It should be noted that these changes to low temperature reaction classes are initial efforts by Dr. Westbrook to update the reaction rate parameters to conform to the latest. Once the effects of these initial improvements are identified by comparison with our data any remaining discrepancies can be used to make additional refinements going forward.

Figure 5-26 compares the measured CO and CO<sub>2</sub> profiles with computed profiles by the original as well as the updated models. Peak CO level is slightly under-predicted by Li *et al.* model and the start of NTC occurs around 685 K, as opposed to 695 K in the experiment. The updated 2,7-DMO model predict higher CO levels at peak reactivity in comparison to both the experiment and the predictions of Li *et al.* model. The updated mechanism predicts that the CO peaks around 660 – 670 K. Despite these discrepancies, the more symmetric CO profile in the updated model as well as over-all improved agreement with the experimental measurements is promising. As mentioned before, the calculated CO<sub>2</sub> levels by Li *et al.* model under-predicted the measured CO<sub>2</sub> levels near and at the peak reactivity. In the updated mechanism, the changes made to reaction rate parameters of two elementary reactions (described in item 4 above), resulted in higher CO<sub>2</sub> production, more consistent with the PFR data.



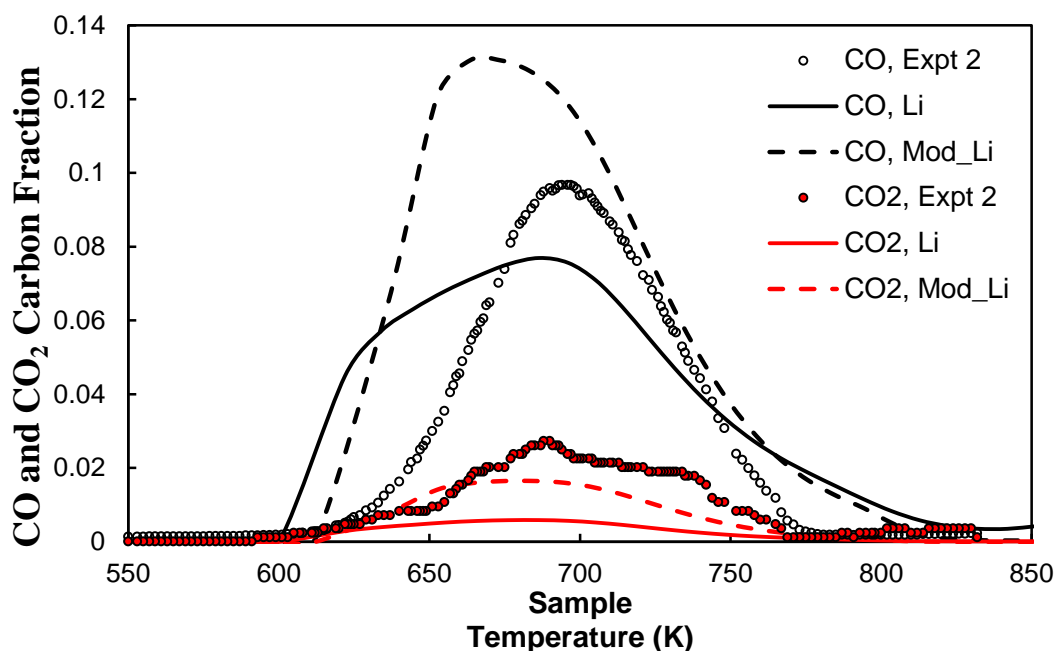


**Figure 5-26: CO and CO<sub>2</sub> profiles during the oxidation of 2,7-DMO: Experiment, Li *et al.* model, and modified Li *et al.* model.**

The updated model captures the fuel consumption profile fairly well, as shown in Figure 5-27. The new calculation for fuel molar fraction at 840 K sample temperature shows a drastic improvement, likely due to adjustment of the same pathways that resulted in sudden increase of C<sub>2</sub>-C<sub>4</sub> alkenes at temperatures above 830 K (see section 5.5, Figure 5-11). The updated model still over-predicts the fuel consumption at sample temperatures 646 K, 699 K, and 749 K.

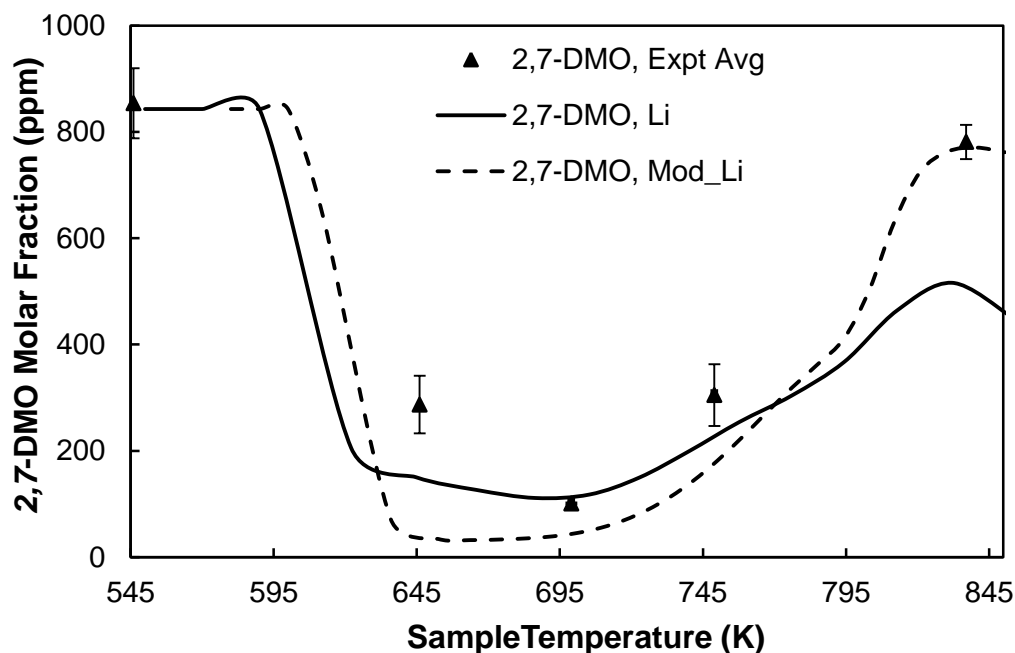


**Figure 5-27: Molar fraction of 2,7-DMO during the oxidation run: Averaged data from three replicate experiments vs. the predictions of the original as well as the modified Li *et al.* model.**

The calculated and measured  $C_2$ - $C_4$  alkenes are compared in Figure 5-28. The mechanisms predict that propene, ethene, and butene are the major olefins produced in descending order of molar fraction. This is in contrast with experimental measurements where butene was the dominant alkene produced, followed by propene and ethene. Although the deficiency of Li *et al.* in predicting the correct distribution of these species is not fully addressed in the updated model, the modified mechanism predicts a significantly higher contribution of *iso*-butene to the overall molar fraction of butene (1-, 2-, and *iso*-), more consistent with the anticipated distribution among three butene isomers. In addition, the sudden increase in ethene, propene, and 2-butene levels between 830 K and 850 K is no longer evident. Still, both mechanisms considerably over-predict

ethene and propene levels. In addition, the peak production temperatures disagree with the PFR measurements, where alkenes peaked during the NTC region.

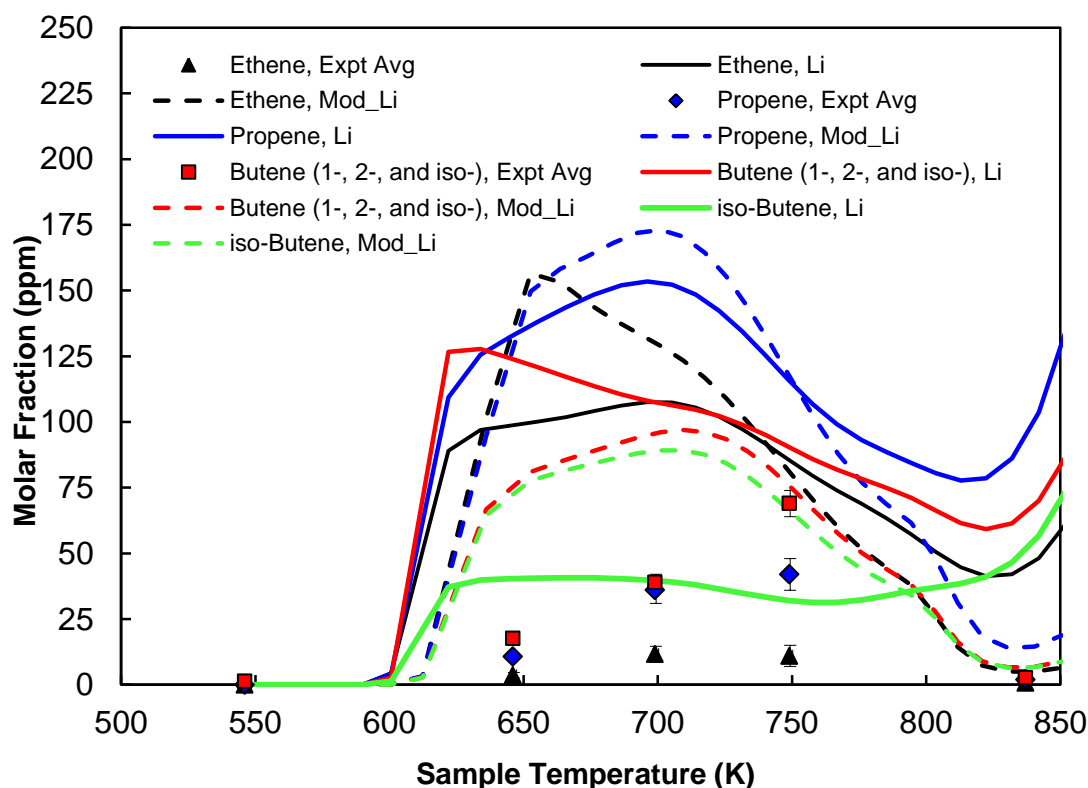


**Figure 5-28: C<sub>2</sub>-C<sub>4</sub> alkene intermediates profiles during the oxidation of 2,7-DMO: Experiment, Li *et al.* model, and modified Li *et al.* model.**

While the new mechanism shows an overall improvement in calculation of C<sub>2</sub>-C<sub>4</sub> alkene profiles, it now over-predicts the molar fraction of 3-methyl-1-butene (see Figure 5-29). An analysis of reaction pathways at the inlet temperature of 650 K (corresponding to a sample temperature of 673 K) indicated that in the updated model, about 73 % of 3-methyl-1-butene is generated through the following steps:

1. The O<sub>2</sub> addition to 2,7-dimethyl-3-octyl radical to form C<sub>10</sub>H<sub>21</sub>OO-3-27 (class 11).

2. About 20 % of  $C_{10}H_{21}OO-3-27$  goes through an internal isomerization to form  $C_{10}OOH3-27f$  (class 15).
3. Approximately 37 % of the formed QOOH radical will decompose to  $C_{10}H_{20}O3-6-27$  (class 23).
4. 3-Methyl-1-butene ( $cC_5H_{10}$ ) is formed when approximately 76 % of  $C_{10}H_{20}O3-6-27$  radical undergoes the reaction  $C_{10}H_{20}O3-6-27 + OH = H_2O + cC_5H_{10} + iC_3H_7COCH_2$  (class 29).

As mentioned, the rate coefficients for classes 15, 23, and 29 has been modified in the updated model. The newly observed deficiency of the model in predicting 3-Methyl-1-butene levels suggests that the rate coefficient(s) for reactions described in steps 2 – 4 may require an additional adjustment within the uncertainties of the estimations.

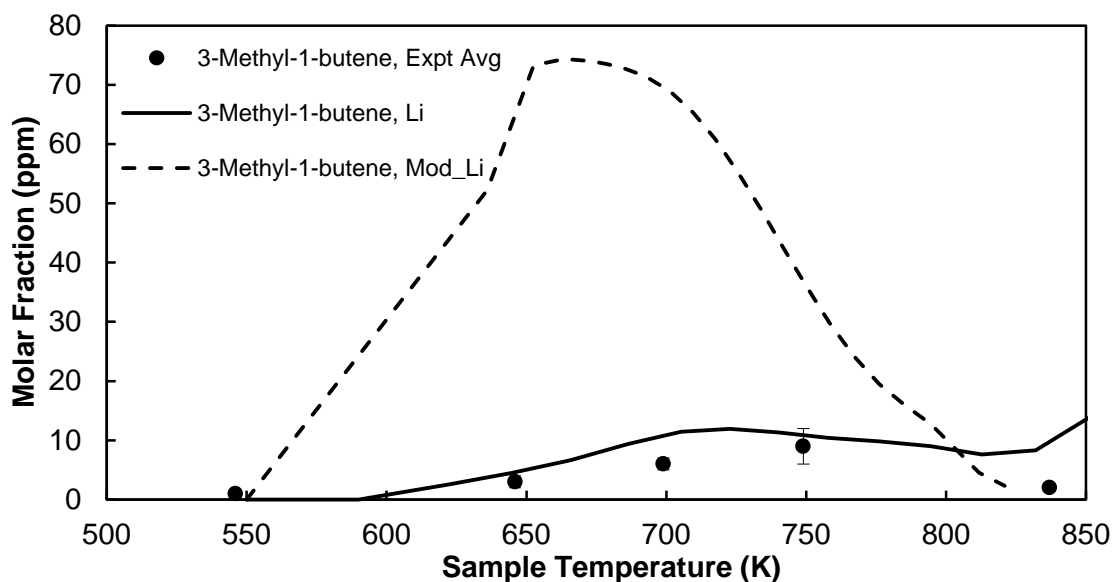


**Figure 5-29: Molar fraction of 3-methyl-1-butene produced during the oxidation of 2,7-DMO: Experiment, *Li et al.* model, and modified *Li et al.* model.**

The updated model exhibits significant improvements, as seen in Figure 5-30, when tested for calculated acetaldehyde profile. Acetaldehyde was over-predicted by a factor of  $\sim 5$  in the Li *et al.* model at peak production. In the updated model, the calculated peak level of acetaldehyde (at sample temperature of 665 K) is about  $\sim 3$  times higher than measured peak level (at sample temperature of 700 K). The formaldehyde profile has remained unchanged in the updated model, warranting the need for refinement of model to improve the predictions for formaldehyde.

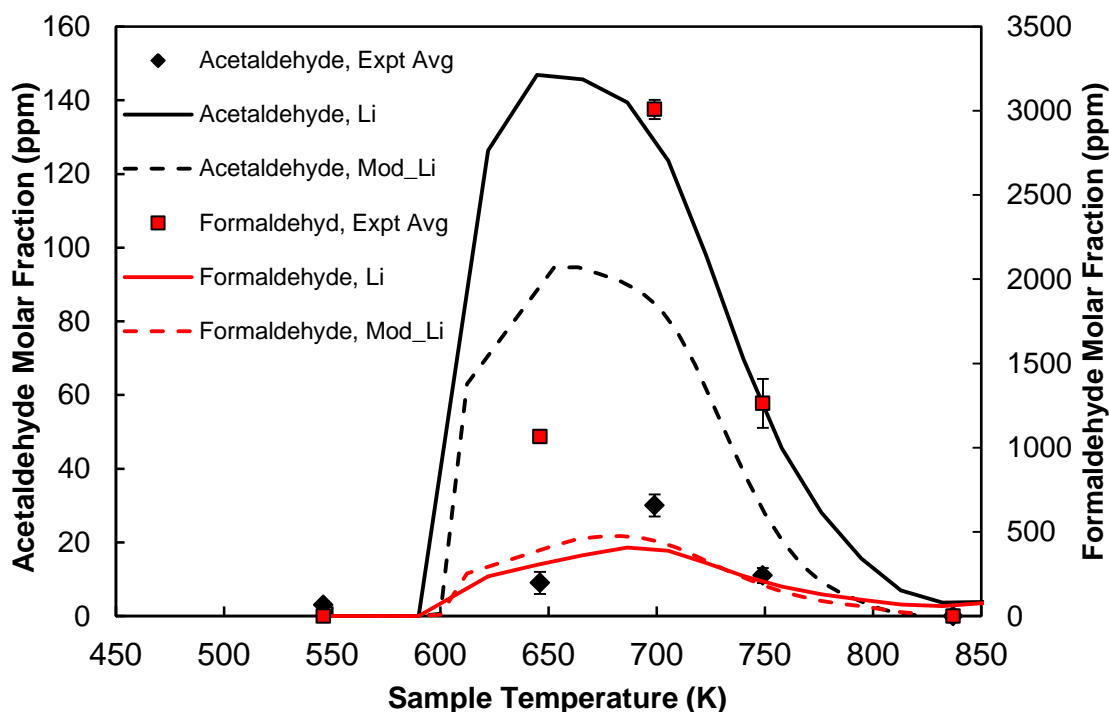


**Figure 5-30: Molar fractions of formaldehyde and acetaldehyde during the oxidation of 2,7-DMO: Experiment, Li *et al.* model, and modified Li *et al.* model.**

Figure 5-31 presents the comparison between the experimental measurements of acetone and the predicted profile by Li *et al.* model and the updated model. In general,

both mechanisms perform fairly well in their calculations of acetone profile, although the updated model exhibits a slightly improved trend.

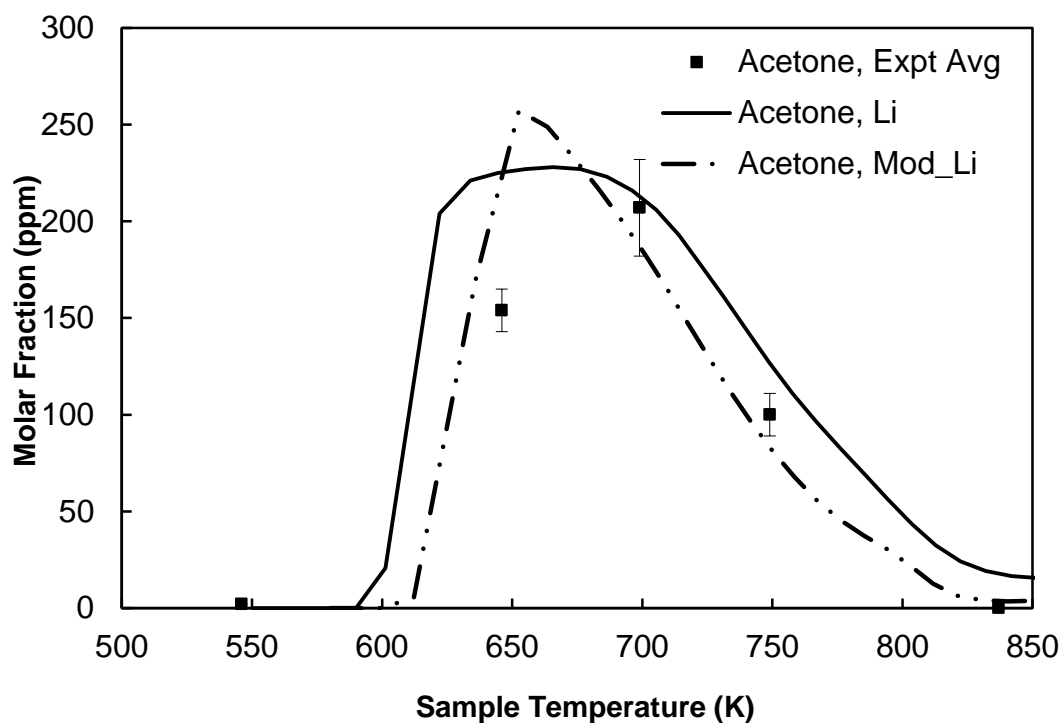


**Figure 5-31: Molar fraction of 2,7-DMO during the oxidation run: Averaged data from three replicate experiments vs. the predictions of the original as well as the modified Li *et al.* model.**

## 5.7 Closure

The oxidation of 2,7-DMO / oxygen / nitrogen was investigated in a pressurized flow reactor at temperatures of 550-850 K, a pressure of 8 atm (0.8106 MPa), lean equivalence ratio of 0.3, and a residence time of 120 ms. The reactivity of 2,7-DMO in the low temperature and Negative Temperature Coefficient (NTC) regimes was mapped with the aid of a continuous non-dispersive infrared (NDIR) carbon monoxide/carbon dioxide analyzer.

Seventy-three stable intermediate species (including the parent fuel) were identified and measured during the GC/MS/FID analysis of extracted samples at five selected temperatures. Together with CO and CO<sub>2</sub>, these measured stable intermediates accounted for 85% - 105% of total carbon input.

The reactivity of 2,7-DMO was considerably reduced from that of *n*-decane at comparable conditions. In addition, the intermediate distribution from 2,7-DMO was different from that of *n*-decane, with propene and *iso*-butene replacing ethene as the major olefins produced from 2,7-DMO and *n*-decane, respectively. In addition, the structure of 2,7-DMO resulted in the production of acetone at the start of NTC (i.e. at 699 K), a species not detected from *n*-decane. The species was also produced in considerable quantities at sample temperatures of 649 K and 749 K. The data were compared to predictions from recently published detailed chemical kinetic model [26] for 2,7-DMO. The model captured the NTC behavior and closely predicted the peak CO level at the start of NTC; however, there was a difference in small olefins levels which indicates a major need for the refinement of low-temperature reaction classes.

Based on the PFR data for 2,7-DMO, a collaborative effort was initiated with Dr. Charles Westbrook (LLNL). The effort resulted in an updated 2,7-DMO model with extensive refinements to the majority of low temperature reaction classes. In addition, the rate parameters for two sensitive reactions with respect to CO<sub>2</sub> were adjusted to reflect the higher levels of CO<sub>2</sub>, measured during the PFR experiments. The first-cut comparisons between the PFR data and the updated model indicated an overall improvement. Some remaining or reinforced discrepancies between the experiment and the model were noted,

indicating a need for additional fine-tuning of the mechanism in the low temperature regime.

The next chapter will discuss the results of preliminary pyrolysis experiments with *n*-decane in the intermediate temperature regime, 850-1000 K, performed for the first time in the PFR facility.



## CHAPTER 6 : THE PYROLYSIS OF *n*-DECANE OVER THE TEMPERATURE RANGE OF 850 – 1000 K

### 6.1 Introduction

This chapter explores the pyrolysis of *n*-decane in the PFR over the temperature range of 850 – 1000 K. Previously, the PFR facility had only been used to investigate the low temperature (typically 550 – 850 K) oxidation of hydrocarbons and jet fuels. The pyrolysis experiments with *n*-decane aimed at extending the understanding of fuel pyrolysis kinetics that become significant at higher temperatures.

The extent of fuel decomposition is a function of various parameters such as temperature, residence time, pressure, and third body effects. The onset of fuel decomposition occurs at intermediate temperatures, typically around 950 K. Too short of a residence time or too low of a pressure will affect the onset temperature for fuel decomposition. In addition, reactions that involve third-body molecules such as H<sub>2</sub>O can increase the production of radicals such as H, which in turn will accelerate the fuel decomposition rates.

In the pressure range that PFR experiments are conducted, decomposition of larger radicals (> C<sub>6</sub>) are in their high-pressure limit, i.e. independent of pressure. In other words, the operating pressure is sufficiently high that rate coefficients of the reactions will no longer change with increasing or decreasing the pressure. This was confirmed by performing simulations over a pressure range of 4 – 16 atm. Figure 6-1 presents an example simulation of *n*-dodecane (C<sub>10</sub>H<sub>26</sub>) pyrolysis using LLNL 2011 model, over the inlet temperature range of 850 – 1300 K at a residence time of 90 ms. As seen, the change

in profiles for fuel depletion and ethene formation is almost negligible at all three tested pressures, i.e. 4 atm, 8 atm, and 16 atm. This precludes the merits of operating at higher pressures to possibly enhance fuel decomposition.

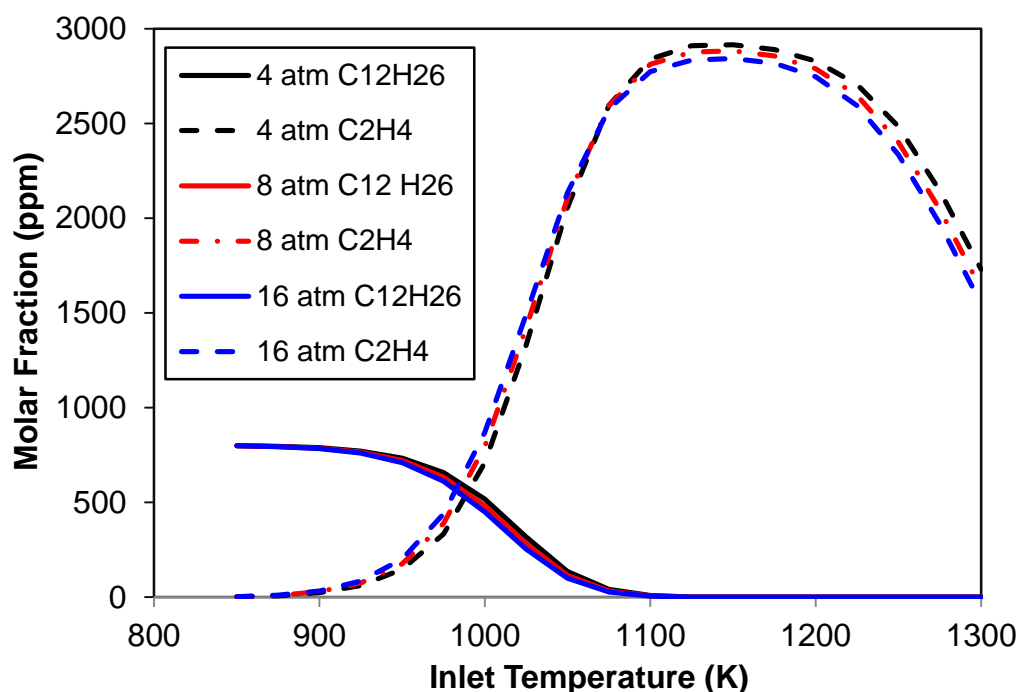


**Figure 6-1: Demonstration of high-pressure limit (i.e. no dependence on pressure) for a sample pyrolysis run with *n*-dodecane using LLNL 2011 model; plug flow reactor module; initial fuel mole fraction 800 ppm, residence time 90 ms.**

In the PFR experimental methodology, the reactant mixture is only comprised of fuel and nitrogen (as the diluent), eliminating the effect of other species such as water, known to have an increased third-body efficiency in comparison to inert gases such as nitrogen and argon. This was also confirmed via simulations with added water content to the reactants' mixture. Figure 6-2 presents an example of simulations of *n*-dodecane pyrolysis in a 0-D closed homogeneous batch reactor module at a pressure of 8 atm and a temperature of 1000 K. Using the Optimized JetSurf model, profiles of fuel depletion and

ethene formation were simulated over a residence time range of 0 – 200 ms. As seen, the addition of water to the reactants' mixture considerably enhances the rate at which fuel decomposes to smaller fragments.

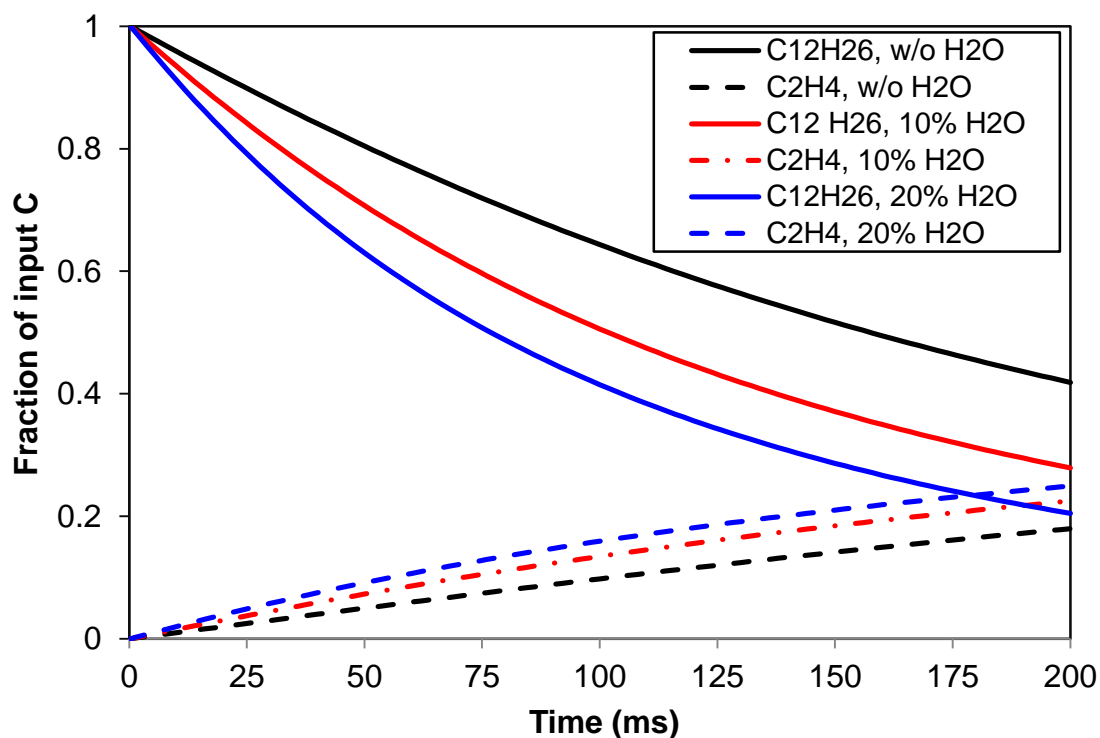


**Figure 6-2: Demonstration of the effect of water addition to reactants' mixture on enhancing the rate of fuel decomposition for an example pyrolysis run with *n*-dodecane using the Optimized JetSurf model; homogeneous batch reactor module.**

The two parameters that can be adjusted in the PFR facility so as to initiate the pyrolysis reactions are temperature and residence time. As described in Section 3.3.2, the maximum achievable temperature and residence times within the operational constraints of the PFR are 1000 K and 168 ms, respectively. The two *n*-decane pyrolysis experiments were, therefore, conducted at a pressure of 8 atm, temperature range of 850 – 1000 K and a residence time of 168 ms. The experiments were conducted at different initial *n*-decane

molar fractions and were otherwise identical. The main goal of these tests was to examine, for the first time, the extent to which *n*-decane decomposes into smaller species at the studied conditions. The experimental data was compared to three existing detailed chemical kinetic models (Jetsurf v 1.0, Optimized JetSurf, and LLNL 2011). Section 6.1 discusses the experimental conditions. The details of the model conditions are presented in Section 6.3. Section 6.4 discusses the results of the experiments as well as the comparisons of the results with computations. In addition, the possible sources of discrepancies between the experiments and the computations, as well as the sources of variations among the models, are discussed for fuel and ethene profiles at 1000 K. A closure to this chapter is presented in Section 6.5.

## 6.2 Experimental Conditions

Two pyrolysis tests, denoted as Expt 1 and Expt 2, were conducted with *n*-decane, with detailed experimental conditions provided in Table 6.1. In these tests, decomposition of *n*-decane was examined at a pressure of 8 atm, temperature range of 850 – 1000 K and a residence time of 168 ms. For experiments 1 and 2, the initial fuel molar fractions were  $856 \pm 39$  ppm and  $990 \pm 46$  ppm, respectively. Both experiments were oxygen free, with high dilution of fuel in nitrogen.

**Table 6-1: Test conditions for *n*-decane pyrolysis, residence time 168±10 ms.**

<b>Parameter</b>	<b>Expt 1</b>	<b>Expt 2</b>	<b>Uncertainty</b>
<b><i>n</i>-Decane, ppm</b>	856 ± 39	990 ± 46	-
<b>N<sub>2</sub></b>	Balance	Balance	-
<b>Equivalence Ratio (φ)</b>	∞	∞	-
<b>Temperature, K</b>	850 -1000	850 -1000	-
<b>Pressure, atm</b>	8.000	8.000	±0.025
<b>Residence Time (ms)</b>	168	168	±10

For Expt 1, a total of four samples were extracted and analyzed with GC/MS/FID; two samples at a temperature of 850 K and two samples at a temperature of 1000 K (S1 and S2). For Expt 2, a total of seven samples were extracted and analyzed; three samples at 850 K, one sample at 900 K, one sample at 950 K and two samples at 1000 K.

### 6.3 Experimental Results

Table 6-2 summarizes the results of GC/MS/FID analysis of S1 and S2, collected during Expt 1 at a temperature of 1000 K. The results are tabulated in terms of the total contribution of each measured intermediate to the overall carbon balance. The analysis indicated that on average, only about 17 % of fuel decomposed to smaller hydrocarbon fragments at 1000 K. Among the handful of intermediate species produced, ethene, propene, and 1-butene were the major intermediates produced in descending order of molar fraction with ethene contributing to about 3.9 % of total carbon input at 1000 K. The carbon balance was 93 % for S1 and 94 % for S2. The less than 100 % carbon balance is likely due to experimental uncertainties such as the uncertainty of ± 4.5 % in initial fuel molar fraction measurement (i.e. ± 39 ppm). Trace amount of 1,3-butadiene

(C<sub>4</sub>H<sub>6</sub>) and C<sub>5</sub> – C<sub>9</sub> 1-alkenes were also identified, accounting for about 4 % of total carbon input. It should be noted that the analysis of the two samples collected at 850 K, indicated no evidence of fuel decomposition at that temperature.

**Table 6-2: Speciation of the stable intermediated from *n*-decane pyrolysis at 1000 K; pressure 8 atm, residence time 168 ± 10 ms, initial fuel molar fraction 856 ± 39 ppm.**

Measured contribution to C balance (%)	S1	S2
Ethene (C <sub>2</sub> H <sub>4</sub> )	3.9	3.9
Propene (C <sub>3</sub> H <sub>6</sub> )	1.7	1.6
1-Butene (C <sub>4</sub> H <sub>8</sub> )	1.3	1.3
1,3-Butadiene (C <sub>4</sub> H <sub>6</sub> )	0.3	0.3
1-Pentene (C <sub>5</sub> H <sub>10</sub> )	0.7	0.7
1-Hexene (C <sub>6</sub> H <sub>12</sub> )	1.0	1.0
1-Heptene (C <sub>7</sub> H <sub>14</sub> )	0.8	0.8
1-Octene (C <sub>8</sub> H <sub>16</sub> )	0.7	0.8
1-Nonene (C <sub>9</sub> H <sub>18</sub> )	0.3	0.4
<i>n</i> -Decane (C <sub>10</sub> H <sub>22</sub> )	82.2	83.6
<b>Total</b>	93	94

To track the fuel decay profile over the over the temperature range of 850 – 1000 K, additional samples were collected during Expt 2 at 900 K and 950 K. Figure 6-3 plots the carbon contribution for *n*-decane as well as C<sub>2</sub> – C<sub>6</sub> 1-alkenes at the sample temperatures. As seen, the distribution of alkenes for Expt 2 was similar to that of Expt 1. The initial stages of fuel decay were evident at 950 K. At this temperature, about 6 % of *n*-decane was decomposed. At 1000 K, where transition to intermediate temperature starts, ethene

reached an averaged molar fraction of about  $165 \pm 23$  ppm. Propene, 1-butene and 1-hexene were the other major intermediates in descending order of molar fraction. The carbon balance at 1000 K sample points was 98 % and 95% for the two extracted samples at this temperature. Similar to Expt 1, 1,3-butadiene and  $C_7 - C_9$  1-alkenes were measured at smaller quantities.

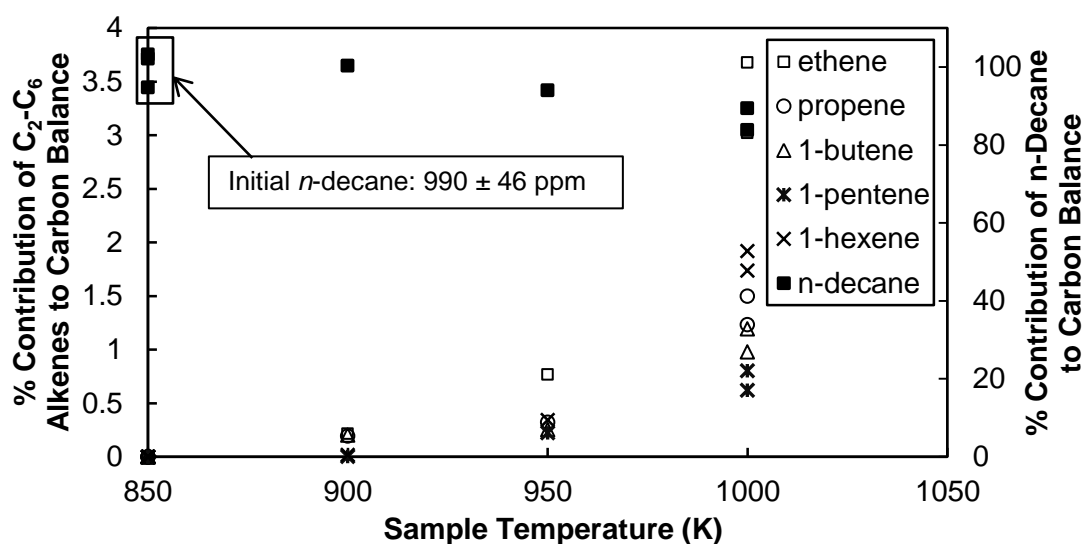


**Figure 6-3: Major species from *n*-decane pyrolysis over the temperature range of 850 – 1000 K; pressure 8 atm, residence time  $168 \pm 10$  ms, initial fuel mole fraction  $990 \pm 46$  ppm.**

#### 6.4 Details of the Model Calculations

The experimental data for Expt 2 were compared against the computations of three detailed chemical kinetic models: the JetSurf v 1.0 model, the Optimized JetSurf model, and the LLNL 2011 Mechanism. Additional details on these mechanisms can be found in Section 4.2. Simulations were run at 10 K intervals over the inlet temperature range of 850 – 1100 K. The models were exercised in CHEMKIN-PRO using the plug flow reactor module.

The ROP analysis was performed for ethene and n-Decane at inlet temperatures of 1000 K and 1050 K. Intermediate species were measured in only small quantities at sample temperatures below 1000 K. Therefore, no ROP analysis was conducted at lower temperatures. Although the PFR was not operated at temperatures above 1000 K, the ROP analysis at the inlet temperature of 1050 K was conducted to examine the significant fuel depletion and ethene formation pathways at higher temperatures. Normalized ROP's of at least  $\pm 0.01$  were considered significant for this analysis. The reaction numbers refer to the sequence in the input files and can be looked up in the "gas-phase kinetics output" file. In addition to a numbered list of species and reactions, the file will contain the pre-exponential factor ( $A$ ), temperature exponent ( $\beta$ ), and activation energy ( $E$ ) values for each Arrhenius equation.

The sensitivity analysis was performed for the inlet temperature of 1000 K and residence time of 168 ms. For sensitivity analysis figures in Section 6.4, the "maximum sensitivities" number under the "preferences" tab in reaction path analyzer was set to 16, meaning that only the reactions with the 16 largest normalized A-factor sensitivities will be displayed. Additional details on input parameters for simulations in CHEMKIN-PRO can be found in Section 4.3.

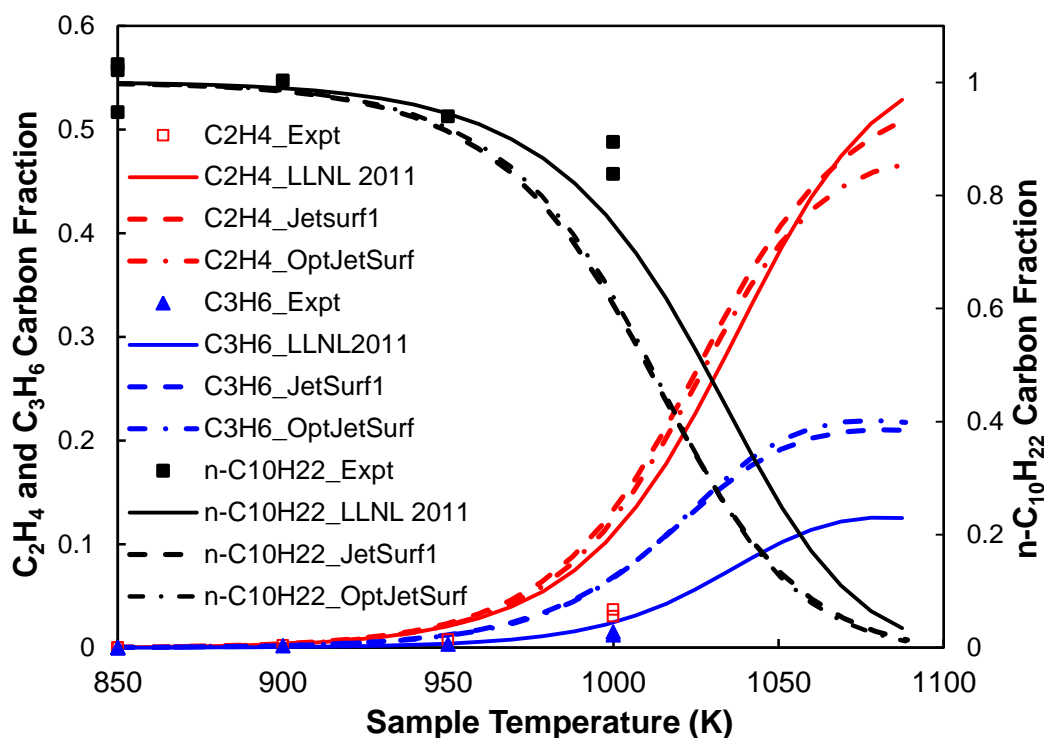
## 6.4 Modeling Results, Comparisons with Experiments, and Discussion

Figure 6-4 provides a comparison of experimental data with predictions of LLNL 2011, JetSurf v 1.0, and Optimized JetSurf mechanisms. The  $x$ -axis represents the calculated endpoint temperatures, denoted as "sample temperature". As pyrolysis reactions are endothermic, the endpoint temperature can be lower than its corresponding input temperature, denoted as "inlet temperature", depending on the fuel decomposition



stage. For inlet temperature of 1000 K, the calculated endpoint temperatures were 2 – 3 K lower, depending on the model examined. The largest calculated  $\Delta T$  was 11 – 13 K, corresponding to the inlet temperature of 1000 K. The y- axis represents the carbon fractions for ethene, propene, and *n*-decane.

The JetSurf v 1.0 and Optimized Jetsurf mechanisms performed almost identical by terms of their predictions for major species profiles. According to simulations, the fuel decay started around the inlet temperature of 950 K and progressed with increasing the temperature. At 1000 K inlet temperature, the molar fractions of ethene and propene were 5 – 6 times higher than that of 950 K inlet temperature. At this temperature, *n*-decane molar fraction was under-predicted by a factor of  $\sim 1.3$  with JetSurf mechanisms and 1.1 with LLNL 2011 model, where the JetSurf mechanisms and LLNL 2011 model predicted 35 % and 24 % fuel conversion, respectively. The molar fractions of ethene and propene at 1000 K were over-predicted by JetSurf mechanisms by factors of  $\sim 3.5$  and 4.5, respectively. The LLNL 2011 model had a slightly better performance, over-predicting ethene molar fraction by a factor of 3 and propene molar fraction by a factor of  $\sim 1.5$ . At inlet temperature of 1100 K, the fuel was almost entirely decomposed to smaller hydrocarbon fragments, with ethene and propene summing up for 65 – 72 % of total carbon input depending on the model examined. The observations from the experiments and the simulations signify the importance of extending the experimental investigation of fuel pyrolysis to higher temperatures, ideally covering the temperature range of 950 – 1100 K; thereby, highlighting the need for future upgrades to the PFR facility to increase the upper operational temperature limit.



**Figure 6-4: Carbon fractions for major species measured during the pyrolysis of *n*-decane: experiment vs. models; temperature range 850 – 1000 K; pressure 8 atm, residence time 168 ms, initial fuel molar fraction 990 ppm.**

Figures 6-5 through 6-7 present the models' calculations of normalized rate of production *n*-decane at inlet temperatures of 1000 K and 1050 K. The y-axis presents the significant reactions that produce or consume *n*-decane. The x-axis shows the normalized ROP values for these reactions. For a reaction that produces *n*-decane, the normalized ROP value is calculated by dividing the rate of production (in mol/cm<sup>3</sup>.s) by the total rate of production (also in mol/cm<sup>3</sup>.s). Likewise, for a reaction that consumes *n*-decane, the normalized ROP value is calculated by dividing the rate of consumption by the total rate of production. Therefore, the normalized ROP values range from -1 to 1.

In all three mechanisms, the fuel is primarily consumed by hydrogen abstraction from secondary carbon atoms of *n*-decane via H radicals. The total relative ROP for these

reactions is about 60 %. The reaction rates associated with flux of *n*-decane to 2-, 3-, 4-, and 5-decyl radicals are assumed identical. Therefore, the calculated yields for these radicals are equally dominant. The H-abstraction from primary carbon atom of *n*-decane via H radicals and H-abstraction reactions from the secondary carbon atoms via CH<sub>3</sub> radicals are less significant, with total relative ROPs of ~ 6 % and ~ 20 % (~ 5 % for each of the four pathways to 2-, 3-, 4-, 5-decyl radicals), respectively. Also, a comparison of absolute rates of production at 1000 K indicated that the forward rate of progress for hydrogen-mediated H-abstraction reactions to produce 2-, 3-, 4-, and 5-decyl radicals is ~ 1.5 times higher in JetSurf mechanisms than it was in LLNL 2011 model (e.g.  $2.2 \times 10^{-8}$  mol/cm<sup>3</sup>.s in JetSurf v 1.0 versus  $1.5 \times 10^{-8}$  mol/cm<sup>3</sup>.s in LLNL 2011), consistent with the observation that the JetSurf mechanisms predict higher fuel conversion levels at 1000 K.

### Normalized Rate of Production (ROP) of *n*-Decane

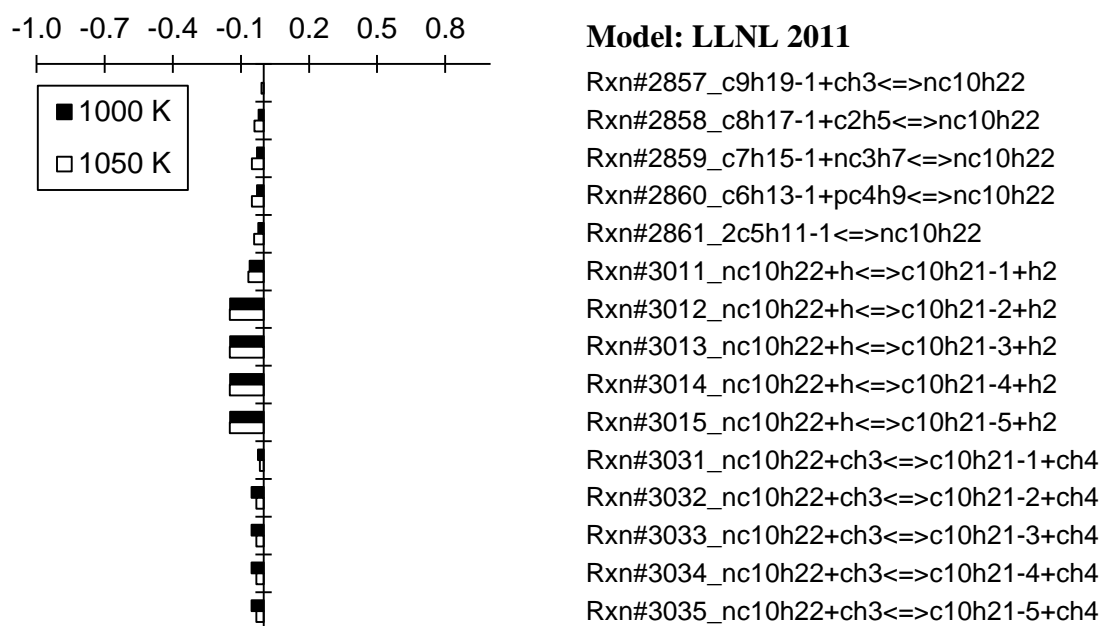


**Figure 6-5: ROP of *n*-decane at select inlet temperatures under pyrolysis conditions; pressure 8 atm, residence time 168 ms, initial fuel molar fraction 990 ppm, LLNL 2011.**

### Normalized Rate of Production (ROP) of *n*-Decane

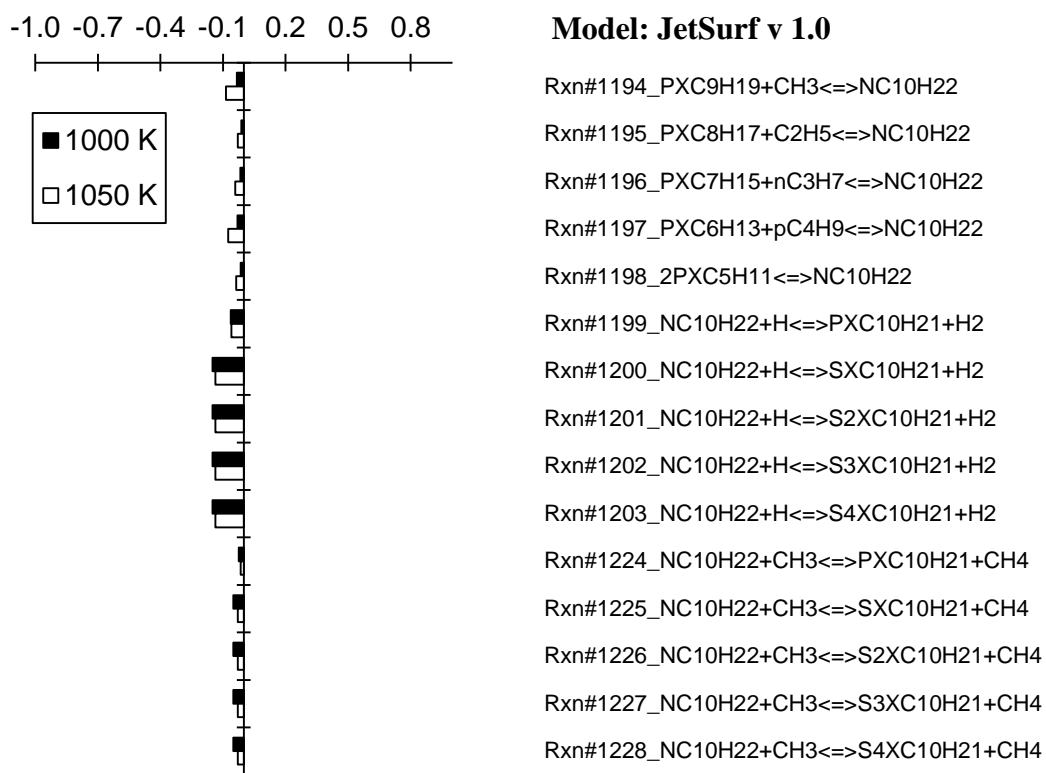


**Figure 6-6: ROP of *n*-decane at select inlet temperatures under pyrolysis conditions; pressure 8 atm, residence time 168 ms, initial fuel molar fraction 990 ppm, JetSurf v 1.0.**

### Normalized Rate of Production (ROP) of *n*-Decane

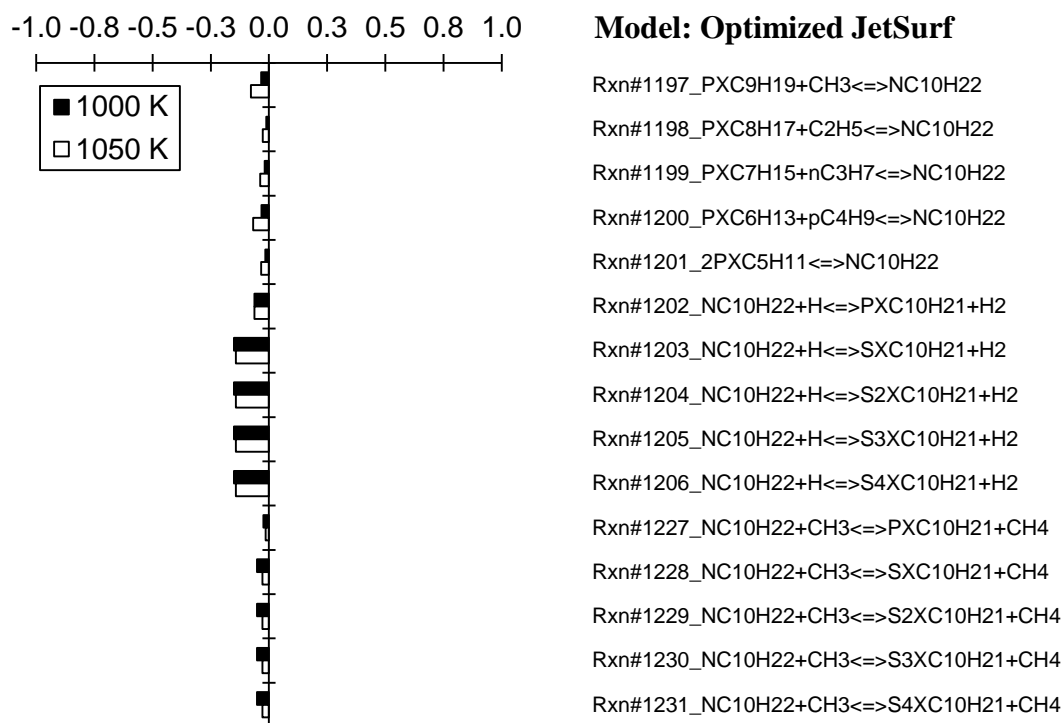


**Figure 6-7: ROP of *n*-decane at select inlet temperatures under pyrolysis conditions; pressure 8 atm, residence time 168 ms, initial fuel molar fraction 990 ppm, Optimized JetSurf.**

At 1050 K, similar reactions to those for 1000 K dominate the fuel depletion pathways, indicating that the key reaction pathways for fuel consumption remain unchanged when moving to the higher temperature. The relative ROP values of these reaction pathways, however, are slightly different than those of 1000 K. Figure 6-8 presents the logarithmic change of rate coefficient,  $k$ , with respect to temperature for H-abstraction from *n*-decane via hydrogen to produce 2-decyl radical, as obtained from gas-phase kinetics output file of JetSurf v 1.0. An identical plot would be obtained for 3-, 4-, and 5-decyl radicals. As seen, the rate coefficient displays a considerable dependence on temperature over the range of 300 – 2000 K. In the range of 1000 – 1100 K, however, the

change of rate coefficient with temperature does not appear to be a controlling factor. This suggests that some other parameters such as alternative reaction pathways and increased availability of hydrogen atoms start becoming more significant in terms of controlling the extent of fuel decomposition at temperature of 1050 K and higher.

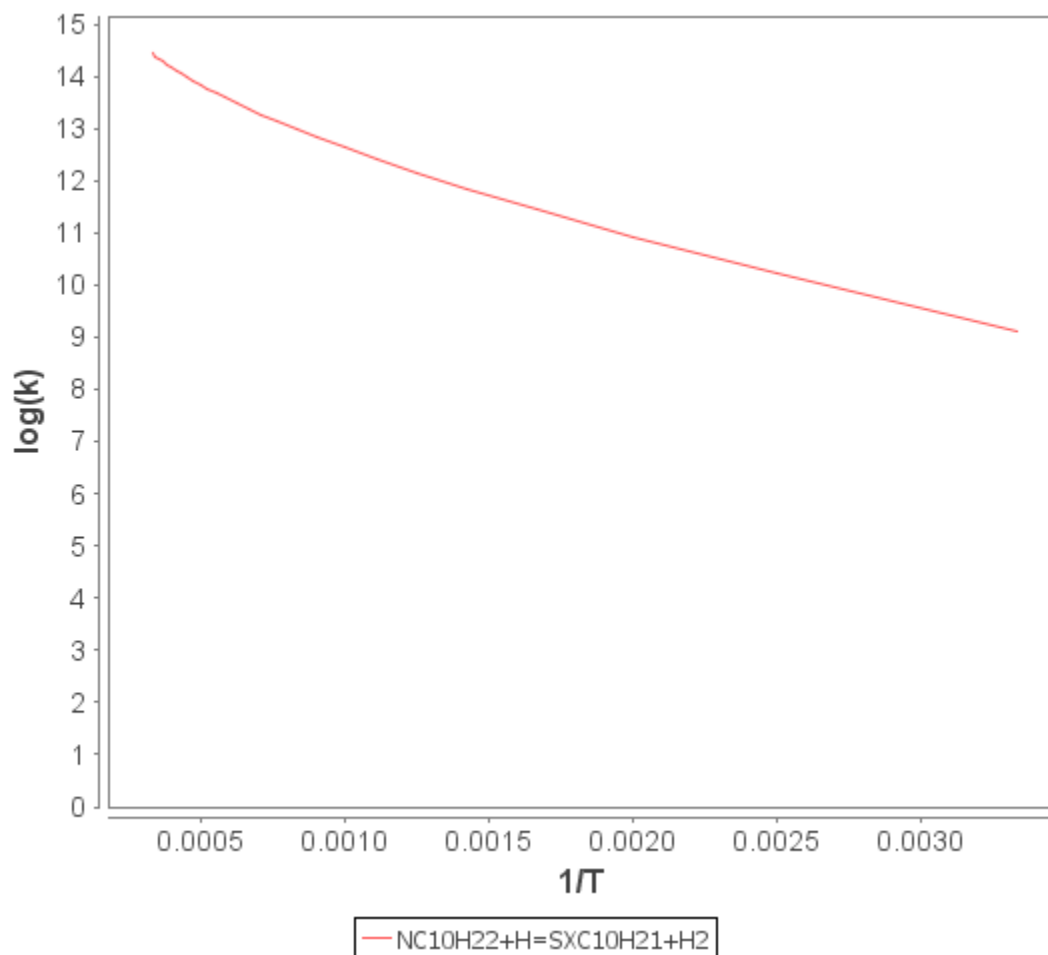


**Figure 6-8: The change of  $\log(K)$  with temperature for hydrogen mediated H-abstraction from *n*-decane to produce 2-decyl radical. Model: JetSurf v 1.0.**

In fact, moving toward higher temperatures, e.g. 1100 K, the uni-molecular *n*-decane decomposition (C-C fission) reaction to produce smaller alkyl radicals appear to become considerably more significant. For example, at inlet temperature of 1100 K, the JetSurf v 1.0 model predicts that only about 32% of *n*-decane will be consumed via H-abstraction reactions from secondary carbons atoms of the parent fuel molecule. About 21 % of *n*-decane will go through a C-C bond fission reaction to produce CH<sub>3</sub> and C<sub>9</sub>H<sub>19</sub> radicals. Also, another 18% of *n*-decane is predicted to convert directly to C<sub>4</sub> and C<sub>6</sub> alkyl radicals. For LLNL 2011 the relative ROP values for these reactions are only 2.3 % and 10.8 %, respectively. In both JetSurf and LLNL mechanisms, the relative ROP value of *n*-decane decomposition to ethyl and octyl radicals is considerably high, about 7 % and 8 %, respectively. Still, in LLNL 2011, about 53 % of *n*-decane is consumed via H-abstraction reactions from secondary carbon atoms of *n*-decane. Although C-C fission reactions also become important, the fuel is still primarily consumed by H-abstraction reactions to produce decyl radicals. As it will be seen later in this section, the C-C fission reactions of *n*-decane are also among the sensitive reactions that increase fuel depletion at 1000 K. This observation suggests that the differences between the predictions of JetSurf and LLNL mechanisms for fuel decay profile at temperatures higher than 1000 K can be at least partly attributed to the JetSurf mechanisms favoring the C-C fission pathways over the H-abstraction pathways at higher temperatures.

Figures 6-9 through 6-11 show normalized pre-exponential factor (i.e. A-factor) sensitivities for the 16 most sensitive reactions at 1000 K with respect to *n*-decane. For a sensitive reaction, a change in the rate coefficient will cause a significant change in the overall reaction rate. A positive sensitivity value is indicative of a reaction that impedes

fuel decomposition, while a negative value corresponds to a reaction that favors fuel decay pathways. In all three mechanisms, the recombination reaction of methyl ( $\text{CH}_3$ ) radical (i.e.  $2\text{CH}_3 (+\text{M}) \rightleftharpoons \text{C}_2\text{H}_6 + (\text{M})$ ) reaction has the highest positive sensitivity. The calculated rate coefficients for this reaction (based on the associated  $A$ ,  $\beta$ , and  $E_a$  parameters) in JetSurf v 1.0, Optimized JetSurf, and LLNL 2011 mechanisms is  $2.42 \times 10^{13}$ ,  $2.77 \times 10^{13}$ , and  $2.63 \times 10^{13}$ , respectively. In all three mechanisms, the C-C fission reactions of *n*-decane to produce alkyl radicals have significant negative sensitivities. For example, decomposition of *n*-decane to produce a  $\text{C}_6$  and a  $\text{C}_4$  alkyl radical has the highest negative sensitivity in both JetSurf mechanisms and the LLNL 2011 mechanism. In JetSurf mechanisms, C-C fission reaction of *n*-decane to produce methyl and a  $\text{C}_9$  alkyl radical is the second most sensitive reaction that enhances the fuel decay.

The reactions of H-abstraction from *n*-decane via hydrogen and methyl radicals are also among the most sensitive reactions that enhance fuel decomposition. The high sensitivity of H-abstraction reactions from *n*-decane, confirms the significance of availability of hydrogen and methyl radicals on the extent of fuel decomposition. An ROP analysis for hydrogen at 1000 K indicated that in all three mechanisms, the reaction  $\text{C}_2\text{H}_4 + \text{H} + (\text{M}) \rightleftharpoons \text{C}_2\text{H}_5 (+\text{M})$  is the primary source of hydrogen in the system. The reaction also produces ethene, the most dominant product of fuel decomposition. At 1000 K, the absolute rate of production of hydrogen from  $\text{C}_2\text{H}_5$  in JetSurf v 1.0, Optimized JetSurf, and LLNL 2011 is  $1.22 \times 10^{-7}$  mol/cm<sup>3</sup>.s,  $1.17 \times 10^{-7}$ , and  $7.14 \times 10^{-8}$ , respectively. Lower calculated absolute production levels for hydrogen in LLNL 2011 in comparison to JetSurf, is consistent with the lower fuel depletion rates in the LLNL model.



The general conclusion from the performed comparisons between LLNL and JetSurf mechanisms is that the mechanisms are similar in terms of their predictions of dominant pathways for fuel decay and hydrogen production. The deviations most likely arise from the specification of pre-exponential factor ( $A$ ), the temperature exponent ( $\beta$ ), and the activation energy ( $E_a$ ) that will in turn affect the overall rate coefficient of the key reactions. An example of this is the reaction  $C_2H_4 + H + (M) \rightleftharpoons C_2H_5 (+M)$  which was shown to be a significant source of hydrogen in the system. In LLNL 2011 mechanism, the  $A$ ,  $\beta$ , and  $E_a$  parameters assigned to this reaction are  $1.081 \times 10^{12}$ , 0.454, and 1855, respectively. This corresponds to a rate coefficient of  $1.99 \times 10^{13}$  mol/cm<sup>3</sup>.sec. For JetSurf v 1.0, these parameters are  $1.367 \times 10^9$ , 1.463, and 1355, respectively, corresponding to a rate coefficient of  $2.84 \times 10^{13}$  mol/cm<sup>3</sup>.sec. The Optimized JetSurf uses the same  $\beta$  and  $E_a$  values as in JetSurf v 1.0, although it uses a different  $A$  factor of  $2.238 \times 10^9$ , resulting in a rate coefficient of  $2.57 \times 10^{13}$  mol/cm<sup>3</sup>.sec. The rate coefficient of this reaction in JetSurf mechanisms is 1.3 – 1.4 times higher than that that of LLNL 2011, consistent with the discrepancies observed among the mechanisms in terms of computed fuel decay profiles. This signifies the need for closer investigation of the employed rate rules to address the discrepancies among the mechanisms as well as the difference between the experimentally measured and computed species profiles. In addition, the shift in relative contribution of dominant reaction pathways at temperatures higher than 1000 K, suggests the importance of extending the PFR experiments to higher temperatures so as to capture the entire fuel decay profile, therefore, enabling educated changes to reaction rate parameters and readily observing the implementation of those changes over a wider range of conditions.

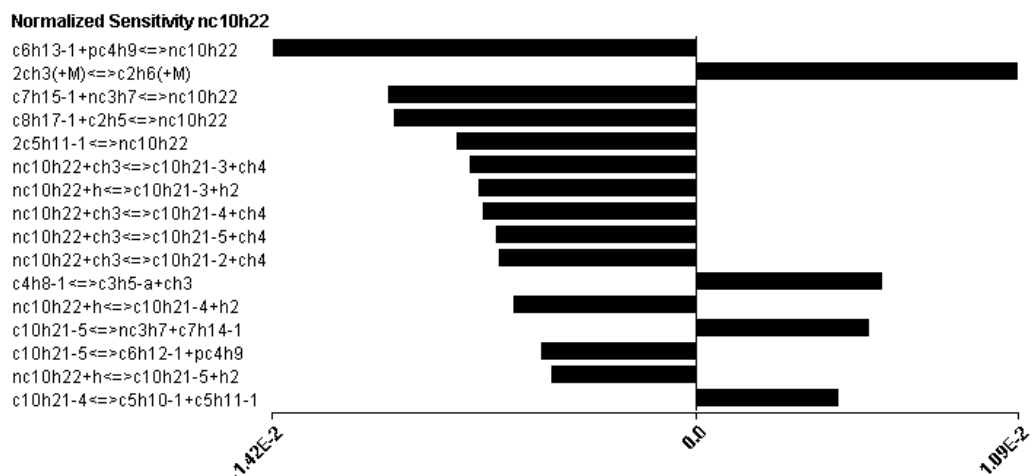


**Figure 6-9: Normalized A-factor sensitivities for significant reactions affecting the molar fraction of *n*-decane at inlet temperature of 1000 K; pressure 8 atm, residence time 168 ms, and initial fuel molar fraction 990 ppm. Model: LLNL 2011.**

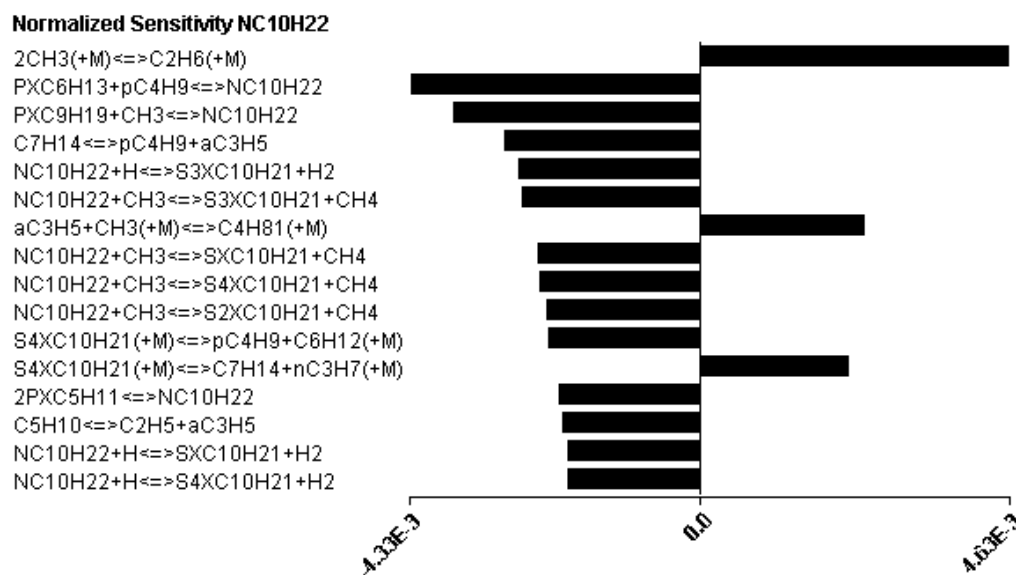


**Figure 6-10: Normalized A-factor sensitivities for significant reactions affecting the molar fraction of *n*-decane at inlet temperature of 1000 K; pressure 8 atm, residence time 168 ms, and initial fuel molar fraction 990 ppm. Model: JetSurf v1.0.**

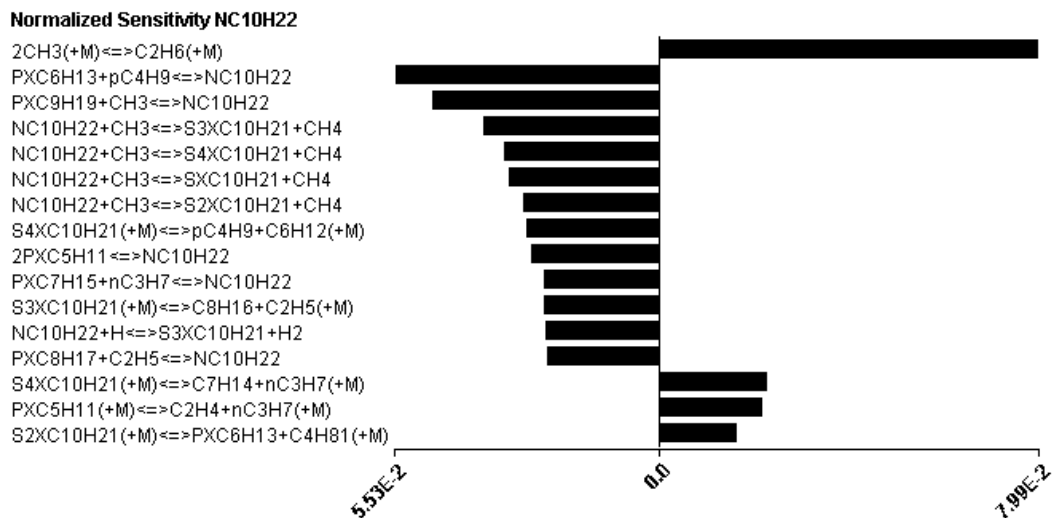


**Figure 6-11: Normalized A- factor sensitivities for significant reactions affecting the molar fraction of *n*-decane at inlet temperature of 1000 K; pressure 8 atm, residence time 168 ms, and initial fuel molar fraction 990 ppm. Model: Optimized JetSurf.**

Figures 6-12 through 6-14 show the result of ROP analysis for ethene at inlet temperatures of 1000 K and 1050 K. At both temperatures, the reaction  $C_2H_4 + H + (M) \rightleftharpoons C_2H_5 + (M)$  is the primary source of ethene, with normalized ROP values of 0.4 and 0.3 in the JetSurf Mechanisms and LLNL 2011, respectively. The formation of ethene and methyl radical from an *n*-propyl radical, i.e. reaction  $C_2H_4 + CH_3 \rightleftharpoons nC_3H_7$  is significant in all three mechanisms, with a normalized ROP value of 0.3. Another key reaction is  $\beta$  scission reaction of butyl radical to produce ethyl and ethene, i.e. reaction  $C_2H_4 + C_2H_5 \rightleftharpoons pC_4H_9$ . An analysis of the flux of *n*-decane to ethene for LLNL 2011 model is presented in Figure 6-15. This is a simplified flux analysis, with “maximum species count” set to 16 in the reaction path analyzer of CHEMKIN-PRO. It only shows the most dominant pathways to ethene production. The 2-, 3-, 4-, and 5- decyl radicals that are primarily formed by H-abstraction from *n*-decane via H atoms, go through  $\beta$  scission reactions to produce an alkene and an alky radical. The smaller alkyl radicals can

go through additional scission reactions, eventually producing ethene, propene, ethyl, n-propyl, butyl radicals. The mechanism predicts about 50% of the formed C<sub>2</sub>-C<sub>4</sub> alkyl radicals will convert to ethene. The reaction flux analysis of JetSurf mechanisms revealed very similar pathways and flux percentage values for formation of ethene from smaller alkyl radical as well as β scission reactions of decyl radicals. Some discrepancies were observed in conversion of decyl radicals to C<sub>6</sub> – C<sub>8</sub> alkyl radicals. For example, in LLNL 2011, 33 % of 1-heptyl radicals undergo a scission reaction to produce ethene and 1-pentyl. In JetSurf v 1.0, only about 5% of 1-hetyl radical go through this reaction pathway.

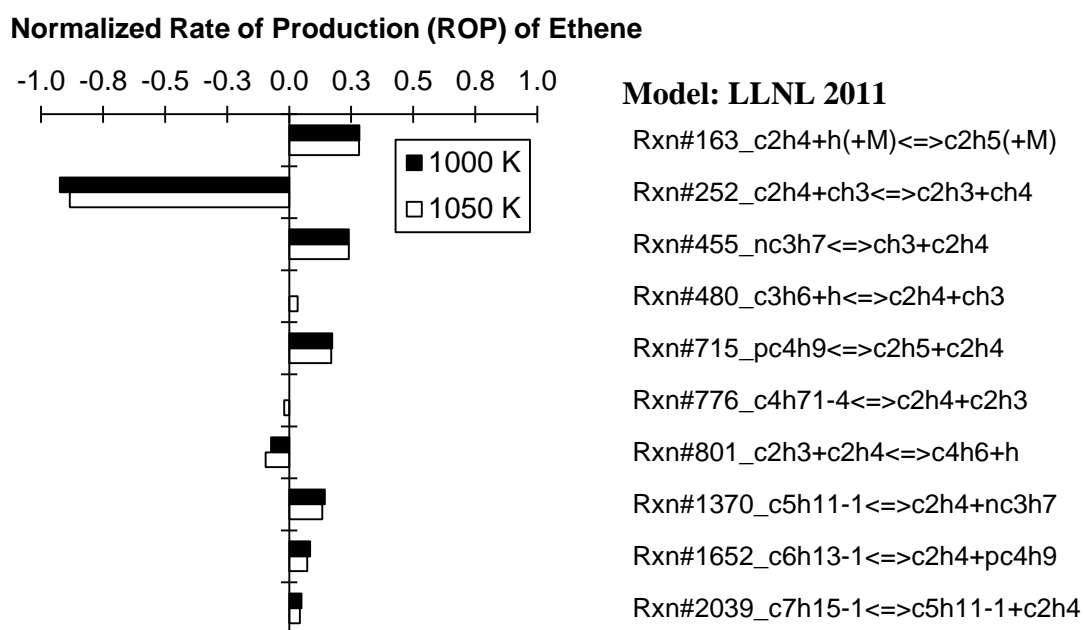
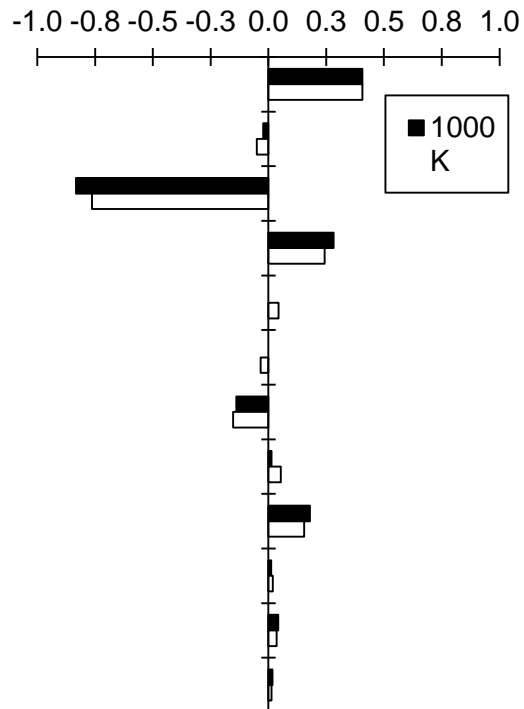


**Figure 6-12: ROP of ethene at select inlet temperatures under pyrolysis conditions; pressure 8 atm, residence time 168 ms, initial *n*-decane molar fraction 990 ppm, LLNL 2011 model.**

### Normalized Rate of Production (ROP) of Ethene



### Model: JetSurf v

- Rxn#249\_  $C_2H_4 + H(+M) \rightleftharpoons C_2H_5(+M)$
- Rxn#250\_  $C_2H_4 + H \rightleftharpoons C_2H_3 + H_2$
- Rxn#261\_  $C_2H_4 + CH_3 \rightleftharpoons C_2H_3 + CH_4$
- Rxn#262\_  $C_2H_4 + CH_3 \rightleftharpoons nC_3H_7$
- Rxn#359\_  $C_3H_6 + H \rightleftharpoons C_2H_4 + CH_3$
- Rxn#475\_  $C_4H_5-2 + C_2H_4 \rightleftharpoons C_5H_6 + CH_3$
- Rxn#481\_  $C_4H_6 + H \rightleftharpoons C_2H_4 + C_2H_3$
- Rxn#552\_  $C_4H_8 + H \rightleftharpoons C_2H_4 + C_2H_5$
- Rxn#579\_  $C_2H_4 + C_2H_5 \rightleftharpoons pC_4H_9$
- Rxn#\_799\_  $C_5H_{10} \rightleftharpoons C_3H_6 + C_2H_4$
- Rxn#812\_  $PXC_5H_{11}(+M) \rightleftharpoons C_2H_4 + nC_3H_7(+M)$
- Rxn#887\_  $PXC_6H_{13}(+M) \rightleftharpoons C_2H_4 + pC_4H_9(+M)$

**Figure 6-13: ROP of ethene at select inlet temperatures under pyrolysis conditions; pressure 8 atm, residence time 168 ms, initial *n*-decane molar fraction 990 ppm, JetSurf v 1.0 model.**

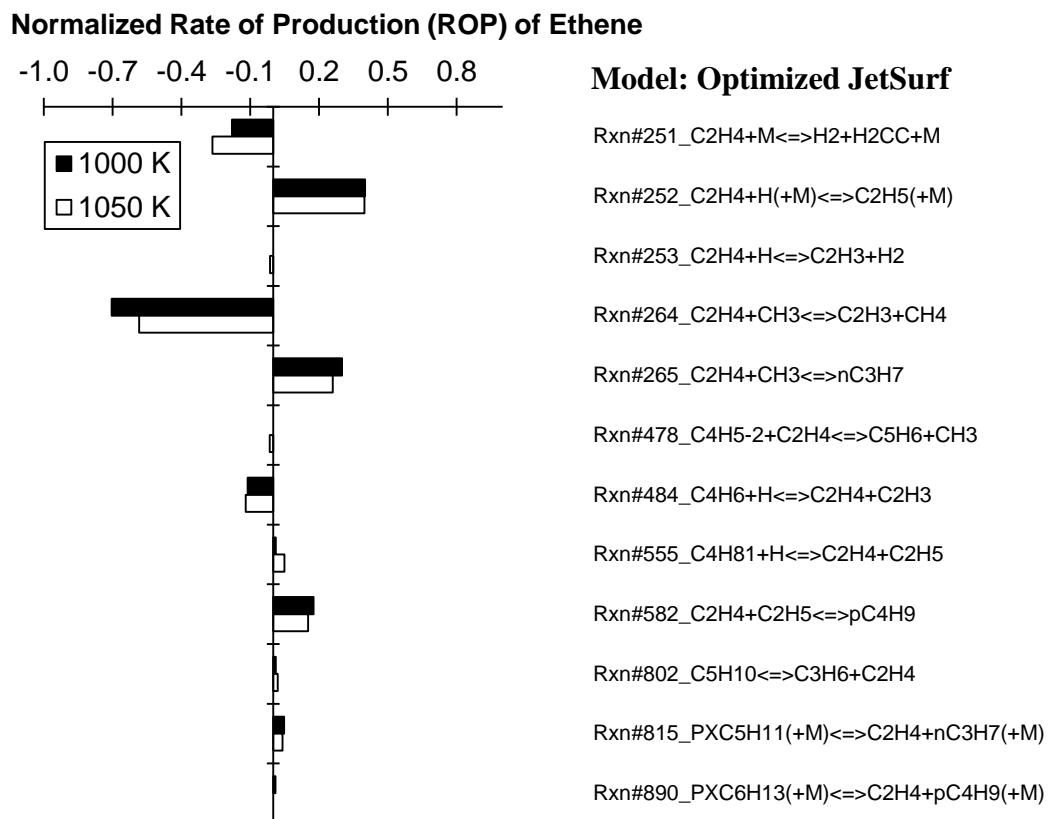


**Figure 6-14: ROP of ethene at select inlet temperatures under pyrolysis conditions; pressure 8 atm, residence time 168 ms, initial *n*-decane molar fraction 990 ppm, Optimized JetSurf model.**

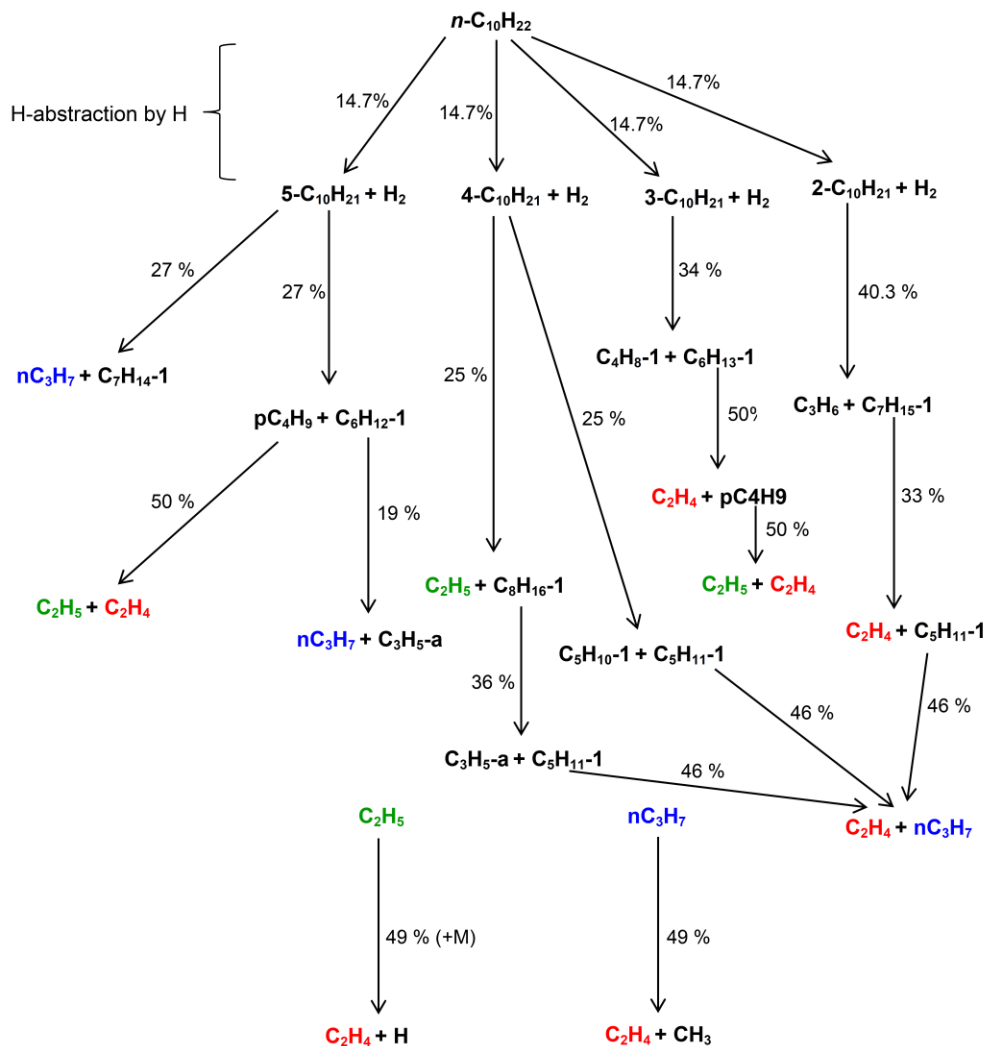


**Figure 6-15: Reaction flux analysis for *n*-decane pyrolysis at 1000 K with an emphasis on reactions leading to the formation of ethene; LLNL 2011 model, pressure 8 atm, residence time 168 ms.**

The results of sensitivity analysis with respect to ethene at 1000 K are presented in Figures 6-16 through 6-18. For LLNL 2011, the most sensitive reactions are the ones in which *n*-decane undergoes C-C fission reactions to produce ethyl, propyl, and butyl radicals. The recombination reaction of  $\text{CH}_3$  to form propene is also among the sensitive reactions with a negative sensitivity value. This reaction was also highly sensitive with

respect to *n*-decane, indicating the close dependence of computed *n*-decane and ethene profiles to the rate of this reaction. In JetSurf v 1.0, the most sensitive reaction that enhances the production of ethene is decomposition of 1-heptene to produce propyl and butyl radicals. This reaction is not recognized among the sensitive reactions in the other two mechanisms and it has considerably high activation energy (p 75 kcal/mol in all the three mechanisms). It is therefore, not an important pathway for production of propyl and butyl radicals. In Jetsurf mechanisms, similar to LLNL model, the recombination reaction of methyl radicals to form propene is among the most sensitive reactions that enhance the production of ethene. Unlike LLNL 2011, direct unimolecular decomposition reactions of *n*-decane to produce ethyl and propyl radicals are not among the most sensitive reactions in JetSurf mechanisms. Instead,  $\beta$  scission reactions of 5-decyl radicals to form propyl and butyl radical have high positive sensitivity values. In all three mechanisms, the  $\beta$  scission reactions of decyl radicals as well as smaller alkyl radicals and the H-abstraction reactions from *n*-decane via methyl and hydrogen radicals have significant positive sensitivities. Overall, the three mechanisms agree in their predictions for dominant reaction pathways for production of ethene. The differences appear to arise from the calculated relative contribution of some key pathways as well as the rate parameters assigned to some key reactions discussed.



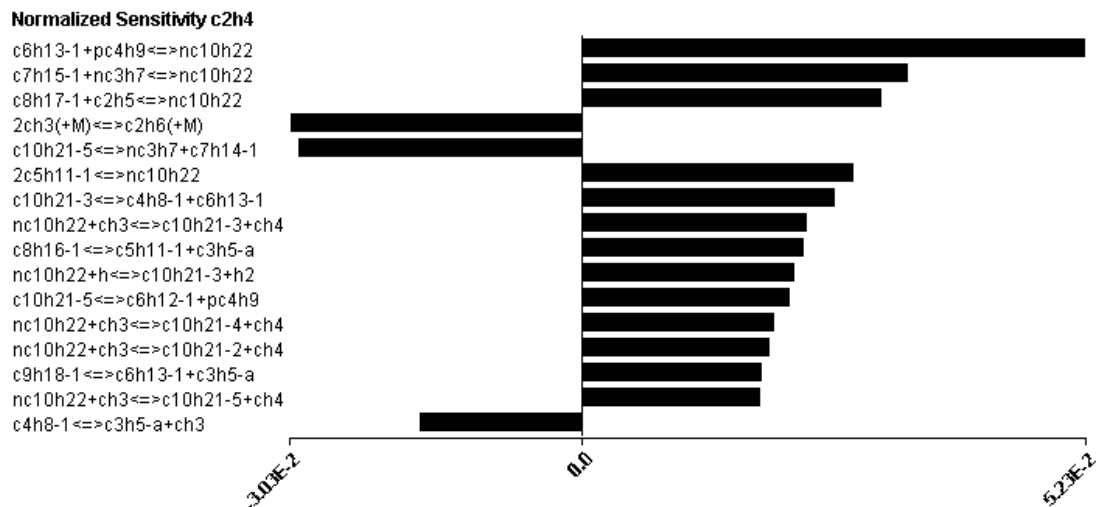


**Figure 6-16: Normalized A-factor sensitivities for significant reactions affecting the molar fraction of ethene at inlet temperature of 1000 K; pressure 8 atm, residence time 168 ms, and initial *n*-decane molar fraction 990 ppm. Model: LLNL 2011.**

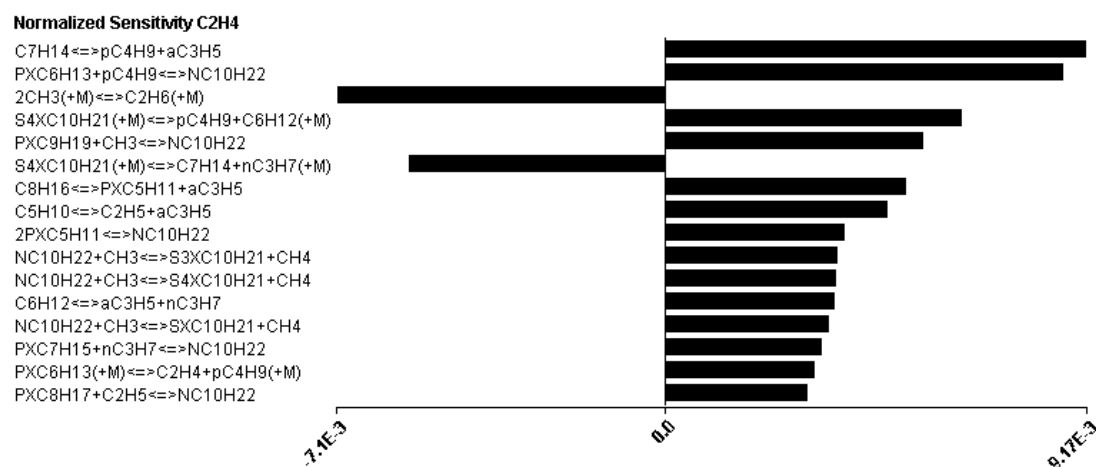


**Figure 6-17: Normalized A-factor sensitivities for significant reactions affecting the molar fraction of ethene at inlet temperature of 1000 K; pressure 8 atm, residence time 168 ms, and initial *n*-decane molar fraction 990 ppm. Model: JetSurf v1.0.**

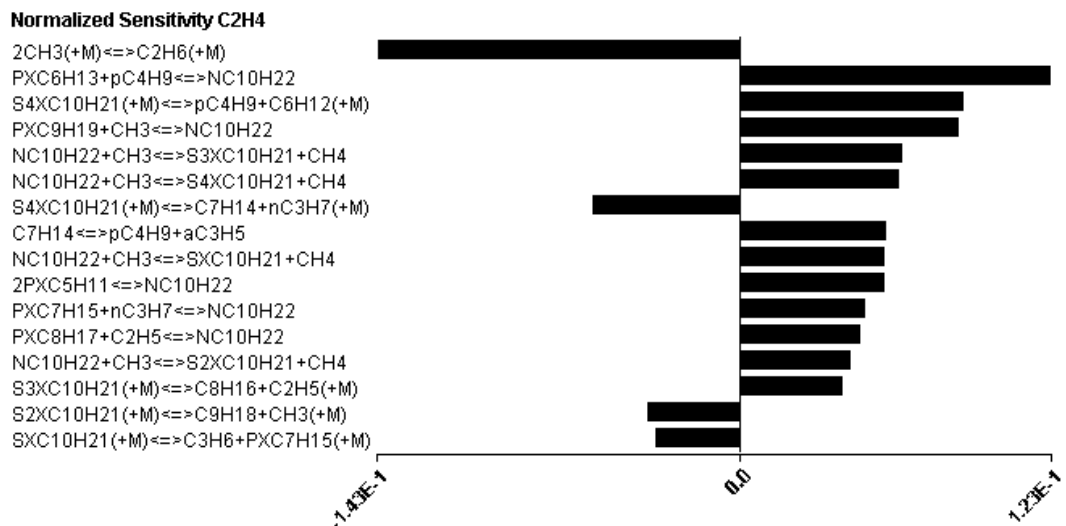


**Figure 6-18: Normalized A-factor sensitivities for significant reactions affecting the molar fraction of ethene at inlet temperature of 1000 K; pressure 8 atm, residence time 168 ms, and initial *n*-decane molar fraction 990 ppm.**

## 6.5 Closure

The Drexel University PFR was used for the first time to investigate the pyrolysis of *n*-decane, a component of a candidate surrogate for JP-8. Specifically, the pyrolysis of *n*-decane was investigated over the temperature range of 850 – 1000 K, at a pressure of 8 atm, and a residence time of 168 ms. Under these conditions, the onset of fuel decomposition occurred around 950 K. At 1000 K, ~ 15 % of *n*-decane was decomposed to smaller hydrocarbon fragments. The speciation of samples collected at 1000 K indicated that ethene and propene are the major pyrolysis products in descending order of molar fraction. C<sub>4</sub>-C<sub>9</sub> 1-alkenes were measured at considerably smaller quantities. The experimental measurements were compared against the predictions of three chemical kinetic mechanisms: JetSurf v 1.0, Optimized JetSurf, and LLNL 2011. All three mechanisms over-predicted ethene levels as well as the extent of fuel decomposition at 1000 K. The JetSurf mechanisms predicted higher fuel conversion and propene levels at

1000 in comparison to LLNL mechanism. In both Jetsurf mechanisms and in the LLNL 2011 model, the reaction  $C_2H_4 + H + (M) \rightleftharpoons C_2H_5 (+M)$  was the major source of hydrogen, availability of which is a key factor in depletion of fuel at 1000 K. The absolute rate of production of hydrogen from  $C_2H_5$  was about 1.7 times higher in JetSurf mechanism than in LLNL 2011, consistent with the lower calculated percentage of fuel decomposition by LLNL model. The differences between the predictions of JetSurf mechanisms and LLNL 2011 became more significant over the temperature range of 1000 – 1100 K, which is currently beyond the operational capabilities of the PFR. Moving toward temperatures higher than 1000 K, it was evident that the JetSurf mechanism differed from the LLNL 2011 mechanism in terms of favoring C-C fission reactions of *n*-decane to produce smaller alkyl radicals over H-abstraction reactions from *n*-decane to produce decyl radicals.

The three mechanisms were similar in their pathways for formation of ethene, the major product of pyrolysis, at 1000 K. Although these dominant pathways were similar, the rate parameters and therefore, the rate coefficient, *k*, for some key reactions differed between the JetSurf mechanisms and the LLNL mechanism. The sensitive reactions at 1000 K with respect to ethene were analyzed for all three mechanisms. Together with the methyl recombination reaction to produce propene, the C-C fission reactions of parent fuel to produce ethyl, *n*-propyl, and butyl were among the most sensitive, impeding and enhancing ethene formation, respectively.

Deviation of the models from the experimental measurement of *n*-decane and ethene molar fractions at 1000 K suggests the need for re-evaluation of relative contribution of key pathways for fuel depletion and ethene production as well as a re-evaluation of rate

parameters such as A-factors and activation energies for the identified sensitive reactions. On the experimental side of the study, given the demonstrated effect of temperature on fuel depletion pathways at 1000 K and higher, future efforts to upgrade the PFR facility to increase the higher temperature limit of PFR operations to cover the 1000 – 1100 K temperature range are strongly recommended.

## CHAPTER 7 : CONCLUDING REMARKS AND RECOMMENFATIONS FOR FUTURE WORK

In this study, the pressurized flow reactor (PFR) at Drexel University was used to examine the oxidation of 2,7-DMO over the temperature range of 550-850 K, at a pressure of 8 atm and a lean equivalence ratio of 0.3 in 4.2% oxygen/nitrogen. Fuel reactivity was mapped by continuous monitoring of carbon monoxide (CO), carbon dioxide (CO<sub>2</sub>) and oxygen (O<sub>2</sub>). Detailed speciation of collected samples was performed at selected temperatures. Furthermore, oxidation data for *n*-decane in the same flow reactor facility at a comparable experimental condition was used to identify the unique effects of branching on fuel reactivity, the onset of NTC region, and distribution of some key stable intermediates. Fuel pyrolysis in the intermediate temperature regime, 850 – 1000 K, also was investigated for the first time in the PFR facility. The experimental results were compared with several existing models for hydrocarbon oxidation and pyrolysis. A summary of main tasks and major findings of this study follows:

1. 2,7-DMO exhibited classical NTC behavior over the studied range of temperature. The Peak reactivity and the low temperature limit of the NTC regime, characterized by maximum O<sub>2</sub> consumption and CO production, was near 695 K. This corresponded to a measured CO molar fraction of approximately 800 ppm, accounting for approximately 10% of total carbon in the unreacted mixture. No reactivity was observed at temperatures above ~ 780 K. The lowest fuel molar fraction was measured at 699 K sample point, with over 90% of 2,7-DMO being converted to intermediate species at this temperature.

2. For detailed speciation, five samples were extracted at sample temperatures representing points near peak reactivity, points near the start and end of reactivity, and points where no reactivity was observed. Seventy-three stable intermediate species (including the parent fuel) were identified and measured. Together with CO and CO<sub>2</sub>, the measured stable intermediates accounted for 85% - 105% of total carbon in the reactants. Also, the major C<sub>2</sub> – C<sub>4</sub> alkenes in descending order of molar fraction at peak production, i.e. at 749 K sample temperature, were: *iso*-butene, propene, 3-methyl-1-butene, and ethene. Acetone was measured at significant quantities and followed the NTC trends.
3. To examine the effect of isomerization on fuel reactivity, the straight-chain analog of 2,7-DMO, *n*-decane, was oxidized in the PFR at comparable conditions. The study revealed that *n*-decane is clearly more reactive than 2,7-DMO at tested conditions. The measurements indicated that during the oxidation of *n*-decane, CO peaked near 698 K, where it accounted for ~18% of total carbon input. It was concluded that the branching does in fact inhibit the fuel reactivity to a considerable extent. Nevertheless, the start of reactivity and the onset of NTC for both isomers of decane occurred at almost identical temperatures.
4. The GC-MS-FID analysis of a sample collected at 715 K during the oxidation of *n*-decane indicated that ~ 94 % of fuel was consumed at this temperature. At this temperature, ethene was the most abundant alkene with a molar fraction of 68 ppm. Propene and butene levels were considerably lower at 23 ppm and 10 ppm, respectively. The observation confirmed that isomerization reverses the distribution of C<sub>2</sub>-C<sub>4</sub> alkenes.

5. The findings from PFR oxidation experiments with 2,7-DMO were compared with the calculations of Li *et al.* model [26] and the possible sources of variations were investigated.
6. Based on the PFR data for 2,7-DMO, a collaborative effort was initiated with Dr. Charles Westbrook (LLNL). The effort resulted in an updated 2,7-DMO model with extensive refinements to the majority of low temperature reaction classes. In addition, the rate parameters for two sensitive reactions with respect to CO<sub>2</sub> were adjusted to reflect the higher levels of CO<sub>2</sub>, measured during the PFR experiments. The first-cut comparisons between the PFR data and the updated model indicated an overall improvement.
7. The Drexel University PFR was used for the first time to investigate the pyrolysis of *n*-decane over the temperature range of 850 – 1000 K, at a pressure of 8 atm, and a residence time of 168 ms. Under these conditions, the onset of fuel decomposition occurred around 950 K. At 1000 K, ~ 15 % of *n*-decane was decomposed to smaller hydrocarbon fragments. The speciation of samples collected at 1000 K indicated that ethene and propene are the major pyrolysis products in descending order of molar fraction. C<sub>4</sub>-C<sub>9</sub> 1-alkenes were measured at considerably smaller quantities.
8. The experimental measurements were compared against the predictions of three detailed chemical kinetic models, i.e. LLNL 2011 model and two variations of JetSurf mechanism. All mechanisms over-predicted the extent of fuel decomposition as well as ethene levels at 1000 K sample temperature.

Overall, this work provides one of the very first experimental studies on oxidation of a C<sub>10</sub> di-methylated alkane, particularly in the low temperature and NTC regimes. The present work also provides opportunities for future modeling work. The initial results of comparisons between the experimental data and the updated Li *et al.* model for 2,7-DMO have shown an overall improvement. Additional refinement can be performed within the estimated uncertainties. In addition, the detailed speciation of reaction intermediates provides an opportunity to evaluate the model for features other than reactivity, such as the formation pathways for cyclic ethers. On the pyrolysis experiments side of the study, given the demonstrated effect of temperature on fuel depletion pathways at 1000 K and higher, future efforts to upgrade the PFR facility to increase the higher temperature limit of PFR operations to cover the 1000 – 1100 K temperature range are strongly recommended.



## LIST OF REFERENCES

1. Department of Defense Directive 4140.25, *DoD Management Policy for Energy Commodities and Related Services*, Retrieved October 2015 from <http://www.dtic.mil/whs/directives/corres/pdf/414025p.pdf>.
2. E. Corporan, T. Edwards, L. Shafer, M. J. Dewitt, C. Klingshirn, S. Zabarnick, Z. West, R. Striebich, J. Graham, J. Klein. (2011). Chemical, Thermal Stability, Seal Swell, and Emissions Studies of Alternative Jet Fuels. *Energy & Fuels*, Vol. 25, No. 3, 955-966.
3. X. Hui, K. Kumar, C. Sung, T. Edwards, D. Gardner. (2012). Experimental Studies on The Combustion Characteristics of Alternative Jet Fuels. *Fuel*, Vol. 98, 176-182.
4. H. Wang, M. A. Oehlschlaeger. (2012). Autoignition Studies of Conventional and Fischer–Tropsch Jet Fuels. *Fuel*, Vol. 98, 249-258.
5. C. Allen, D. Valco, E. Toulson, J. H. Yoo, T. Lee. (2013). JP-5 and HRJ-5 Autoignition Characteristics and Surrogate Modeling. *Energy and Fuels*, Vol. 27, No. 12, 7790–7799.
6. D. Valco, G. Gentz, C. Allen, M. Colket, T. Edwards, S. Gowdagiri, M. A. Oehlschlaeger, E. Toulson, T. Lee. (2014). Autoignition Behavior of Synthetic Alternative Jet Fuels: An Examination of Chemical Composition Effects on Ignition Delays at Low to Intermediate Temperatures. *Proceedings of the Combustion Institute*.
7. K. Blakeley. (2012). *DoD Alternative Fuels: Policy, Initiatives and Legislative Activity*. Retrieved October 2015 from: <http://fas.org/sgp/crs/natsec/R42859.pdf>.
8. S. Saxena, I. D. Bedoya. (2013). Fundamental Phenomena Affecting Low Temperature Combustion and HCCI Engines, High Load Limits and Strategies for Extending These Limits. *Progress in Energy and Combustion Science*, Vol. 39, No. 5, 457-488.
9. S. Imtenan, M. Varman, H. H. Masjuki, M. A. Kalam, H. Sajjad, M. I. Arbab, I. M. Rizwanul Fattah. (2014). Impact of Low Temperature Combustion Attaining Strategies on Diesel Engine Emissions for Diesel and Biodiesels: A Review. *Energy Conversion and Management*, Vol. 80, 329-356.

10. W. J. Pitz, N. P. Cernansky, F. L. Dryer, F. N. Egolfopoulos, J. T. Farrell, D. G. Friend, H. Pitsch. (2007). Development of an Experimental Database and Chemical Kinetic Models for Surrogate Gasoline Fuels. *SAE Paper No. 2007-01-0175*.
11. M. Colket, T. Edwards, S. Williams, N. P. Cernansky, D. L. Miller, F. N. Egolfopoulos, P. Lindstedt, K. Seshadri, F. L. Dryer, C. K. Law, D. Friend, D. B. Lenhart, H. Pitsch, A. Sarofim, M. Smooke, W. Tsang. (2007). Development of an Experimental Database and Kinetic Models for Surrogate Jet Fuels. *AIAA Paper No. 2007-0770*, Reno, NV.
12. J. T. Farrell, N. P. Cernansky, F. L. Dryer, D. G. Friend, C. A. Hergart, C. K. Law, R. M. McDavid, C. J. Mueller, A. K. Patel, H. Pitsch. (2007). Development of an Experimental Database and Kinetic Models for Surrogate Diesel Fuels. *SAE Paper No. 2007-01-0201*.
13. N. Donato, C. Aul, E. Peterson, C. Zinner, H. Curran, G. Bourque. (2010). Ignition and Oxidation of 50/50 Butane Isomer Blends. *Journal of Engineering for Gas Turbines and Power*, Vol. 132, No. 5, 051502-051502-9.
14. T. Ogura, Y. Nagumo, A. Miyoshi, M. Koshi. (2007). Chemical Kinetic Mechanism for High Temperature Oxidation of Butane Isomers. *Energy & Fuels*, Vol. 21, No. 1, 130-135.
15. D. Healy, N. S. Donato, C. J. Aul, E. L. Petersen, C. M. Zinner, G. Bourque, H. J. Curran. (2010). Isobutane Ignition Delay Time Measurements at High Pressure and Detailed Chemical Kinetic Simulations. *Combustion and Flame*, Vol. 157, No. 8, 1540-1551.
16. M. Ribaucour, R. Minetti, L. R. Sochet, H. J. Curran, W. J. Pitz, C. K. Westbrook. (2000). Ignition of Isomers of Pentane: An Experimental and Kinetic Modeling Study. *Proceedings of the Combustion Institute*, Vol. 28, No. 2, 1671-1678.
17. H. J. Curran, P. Gaffuri, W. J. Pitz, C. K. Westbrook, W. R. Leppard. (1995). Autoignition Chemistry of the Hexane Isomers: An Experimental and Kinetic Modeling Study. *SAE Technical Paper CONF-9510144-1*.
18. E.J. Silke, H.J. Curran, J.M. Simmie. (2005). The Influence of Fuel Structure on Combustion as Demonstrated by the Isomers of Heptane: a Rapid Compression Machine Study. *Proceedings of the Combustion Institute*, 2005. Vol. 30, No. 2, 2639-2647.
19. C. K. Westbrook, W. J. Pitz, J. E. Boercker, H. J. Curran, J. F. Griffiths, C. Mohamed, M. Ribaucour. (2002). Detailed Chemical Kinetic Reaction Mechanisms for Autoignition of Isomers of Heptane Under Rapid Compression. *Proceedings of the Combustion Institute*, Vol. 29, No. 1, 1311-1318.

20. Z. Wang, O. Herbinet, Z. Cheng, B. Husson, R. Fournet, F. Qi, F. Battin-Leclerc (2014). Experimental Investigation of the Low Temperature Oxidation of the Five Isomers of Hexane. *The Journal of Physical Chemistry A*, Vol. 118, No. 30, 5573-5594.
21. S. M. Sarathy, C. K. Westbrook, M. Mehl, W. J. Pitz, C. Togbe, P. Dagaut, H. Wang, M. A. Oehlschlaeger, U. Niemann, K. Seshadri, P. S. Veloo, C. Ji, F. N. Egolfopoulos, T. Lu. (2011). Comprehensive Chemical Kinetic Modeling of the Oxidation of 2-Methylalkanes From C7 to C20. *Combustion and Flame*, Vol. 158, No. 12, 2338-2357.
22. C. Ji, S. M. Sarathy, P. S. Veloo, C. K. Westbrook, F. N. Egolfopoulos. (2012). Effects of Fuel Branching on the Propagation of Octane Isomers Flames. *Combustion and Flame*, Vol. 159, No. 4, 1426-1436.
23. S. M. Sarathy, U. Niemann, C. Yeung, R. Gheorghiu, C. K. Westbrook, M. Plomer, Z. Luo, M. Mehl, W. J. Pitz, K. Seshadri, M. J. Thomson, T. Lu. (2013). A Counterflow Diffusion Flame Study of Branched Octane Isomers. *Proceedings of the Combustion Institute*, Vol. 34, No. 1, 1015-1023.
24. S. M. Sarathy, T. Javed, F. Karsenty, A. Heufer, W. Wang, S. Park, A. Elwardany, A. Farooq, C. K. Westbrook, W. J. Pitz, M. A. Oehlschlaeger, G. Dayma, H. J. Curran, P. Dagaut. (2014). A Comprehensive Combustion Chemistry Study of 2,5-Dimethylhexane. *Combustion and Flame*, Vol. 161, No. 6, 1444-1459.
25. W. J. Pitz, C. J. Mueller. (2011). Recent Progress in the Development of Diesel Surrogate Fuels. *Progress in Energy and Combustion Science*, Vol. 37, No. 3, 330-350.
26. S. Li, S. M. Sarathy, D. F. Davidson, R. K. Hanson, C. K. Westbrook. (2015). Shock Tube and Modeling Study of 2,7-Dimethyloctane Pyrolysis and Oxidation. *Combustion and Flame*, Vol. 162, No. 5, 2296-2306.
27. B. Sirjean, E. Dames, D. A. Sheen, X. You, C. Sung, A. T. Holley, F. N. Egolfopoulos, H. Wang, S. S. Vasu, D. F. Davidson, R. K. Hanson, H. Pitsch, C. T. Bowman, A. Kelley, C. K. Law, W. Tsang, N. P. Cernansky, D. L. Miller, A. Violi, R. P. Lindstedt. A High-Temperature Chemical Kinetic Model of n-Alkane Oxidation, JetSurf version 1.0, September 15 2009. URL: <http://www.stanford.edu/group/haiwanglab/JetSurf/JetSurF1.0/>.
28. S. Banerjee, R. Tangko, D. A. Sheen, H. Wang, C. T. Bowman. (2015). An Experimental and Kinetic Modeling Study of n-Dodecane Pyrolysis and Oxidation. *Combustion and Flame*, in press.

29. M. J. Pilling (Ed.). (1997). *Low-Temperature Combustion and Autoignition, Volume 35 (Comprehensive Chemical Kinetics)*, Vol. 35: Elsevier Science.
30. J.F. Griffiths. (1995). Reduced Kinetic Models and Their Application to Practical Combustion Systems. *Progress in Energy and Combustion Science*, Vol. 21, 25-107.
31. J. M. Simmie. (2003). Detailed Chemical Kinetic Models for the Combustion of Hydrocarbon Fuels. *Progress in Energy and Combustion Science*, Vol. 29, 599-634.
32. J. A. Miller, M. J. Pilling, J. Troe. (2005). Unravelling Combustion Mechanisms Through a Quantitative Understanding of Elementary Reactions. *Proceedings of the Combustion Institute*, Vol. 30, 43-88.
33. P. Dagaut, A. El Bakali, A. Ristori. (2006). The combustion of kerosene: experimental results and kinetic modelling using 1- to 3-component surrogate model fuels. *Fuel*, Vol. 85, 944-956.
34. F. Battin-Leclerc. (2008). Detailed Chemical Kinetic Models for the Low-Temperature Combustion of Hydrocarbons with Application to Gasoline and Diesel Fuel Surrogates. *Progress in Energy and Combustion Science*. Vol. 34, 440-498.
35. J. T. Edwards, T. J. Bruno. (2006). The Properties of S-8. *Technical Report MIPR F4BEY6237G001*. Physical and Chemical Properties Division, National Institute of Standards and Technology: Boulder, CO.
36. H. J. Curran, P. Gaffuri, W. J. Pitz, C. K. Westbrook. (2002). A Comprehensive Modeling Study of iso-Octane Oxidation. *Combustion and Flame*, Vol. 129, No. 3, 253-280.
37. A. Comandini, T. Malewicki, K. Brezinsky. (2013). Experimental and Modeling Study on the Pyrolysis and Oxidation of iso-Octane. *Proceedings of the Combustion Institute*, Vol. 34, No. 1, 353-360.
38. H. Machrafi, K. Lombaert, S. Cavadias, P. Guibert, J. Amouroux. (2005). Reduced Chemical Reaction Mechanisms: Experimental and HCCI Modeling Investigations of Autoignition Processes of iso-Octane in Internal Combustion Engines. *Fuel*, Vol. 84, No. 18, 2330-2340.
39. M. Jia, M. Xie. (2006). A Chemical Kinetics Model of iso-Octane Oxidation for HCCI Engines. *Fuel*, Vol. 85, No. 17-18, 2593-2604.

40. T. S. Tanaka, F. Ayala, J. C. Keck. (2003). A Reduced Chemical Kinetic Model for HCCI Combustion of Primary Reference Fuels in a Rapid Compression Machine. *Combustion and Flame*, Vol. 133, No. 4, 467-481.
41. Y. Ra, R.D. Reitz. (2008). A Reduced Chemical Kinetic Model for IC Engine Combustion Simulations with Primary Reference Fuels. *Combustion and Flame*, Vol. 155, No. 4, 713-738.
42. S. Dooley, S. H. Won, S. Jahangirian, Y. Ju, F. L. Dryer, H. Wang, M. A. Oehlschlaeger. (2012). The Combustion Kinetics of a Synthetic Paraffinic Jet Aviation Fuel and a Fundamentally Formulated, Experimentally Validated Surrogate Fuel. *Combustion and Flame*, Vol. 159, No. 10, 3014-3020.
43. L. Sileghem, V. A. Alekseev, J. Vancoillie, K. M. Van Geem, E. J. K. Nilsson, S. Verhelst, A. A. Konnov. (2013). Laminar Burning Velocity of Gasoline and the Gasoline Surrogate Components iso-Octane, n-Heptane and Toluene. *Fuel*, Vol. 112, 355-365.
44. M. A. Oehlschlaeger, J. Steinberg, C. K. Westbrook, W. J. Pitz. (2009). The Autoignition of iso-Cetane at High to Moderate Temperatures and Elevated Pressures: Shock Tube Experiments and Kinetic Modeling. *Combustion and Flame*, Vol. 156, No. 11, 2165-2172.
45. C. K. Westbrook, W. J. Pitz, M. Mehl, H. J. Curran. (2011). Detailed Chemical Kinetic Reaction Mechanisms for Primary Reference Fuels for Diesel Cetane Number and Spark-Ignition Octane Number. *Proceedings of the Combustion Institute*, Vol. 33, No. 1, 185-192.
46. P. Dagaut, K. Hadj-Ali. (2009). Chemical Kinetic Study of the Oxidation of Isocetane (2,2,4,4,6,8,8-Heptamethylnonane) in a Jet-Stirred Reactor: Experimental and Modeling. *Energy and Fuels*, Vol. 23, No. 5, 2389-2395.
47. N. Liu, S. M. Sarathy, C. K. Westbrook, F. N. Egolfopoulos. (2013). Ignition of Non-Premixed Counterflow Flames of Octane and Decane Isomers. *Proceedings of the Combustion Institute*, Vol. 34, No. 1, 903-910.
48. C. J. Mueller, W. J. Cannella, T. J. Bruno, B. Bunting, H. D. Dettman, J. A. Franz, M. L. Huber, M. Natarajan, W. J. Pitz, M. A. Ratcliff, K. Wright. (2012). Methodology for Formulating Diesel Surrogate Fuels with Accurate Compositional, Ignition-Quality, and Volatility Characteristics. *Energy & Fuels*, Vol. 26, No. 6, 3284-3303.
49. C. Allen, D. Valco, E. Toulson, T. Edwards, T. Lee. (2013). Ignition Behavior and Surrogate Modeling of JP-8 and of Camelina and Tallow Hydrotreated Renewable Jet Fuels at Low Temperatures. *Combustion and Flame*, Vol. 160, No. 2, 232-239.

50. M. L. Huber, B. L. Smith, L. S. Ott, T. J. Bruno. (2008). Surrogate Mixture Model for the Thermophysical Properties of Synthetic Aviation Fuel S-8: Explicit Application of the Advanced Distillation Curve. *Energy and Fuels*, Vol. 22, No. 2, 1104-1114.
51. S. Li, A. Campos, D. F. Davidson, R. K. Hanson. (2014). Shock Tube Measurements of Branched Alkane Ignition Delay Times. *Fuel*, Vol. 118, 398-405.
52. W. Wang, Z. Li, M. A. Oehlschlaeger, D. Healy, H. J. Curran, S. M. Sarathy, M. Mehl, W. J. Pitz, C. K. Westbrook. (2013). An Experimental and Modeling Study of the Autoignition of 3-Methylheptane. *Proceedings of the Combustion Institute*, Vol. 34, No. 1, 335-343.
53. N. Slavinskaya, U. Riedel, E. Saibov, J. Herzler, C. Naumann, M. Saffaripour, L. Thomas. (2014). Kinetic Surrogate Model for GTL Kerosene. *52nd Aerospace Sciences Meeting, American Institute of Aeronautics and Astronautics*: National Harbor, MD.
54. D. N. Koert, N. P. Cernansky. (1992). A Flow Reactor for the Study of Homogeneous Gas-Phase Oxidation of Hydrocarbons at Pressures up to 20 atm (2 MPa). *Measurement Science and Technology*, Vol. 3, No. 6, 607-613.
55. D. N. Koert. (1990). Effects of Pressure on Hydrocarbon Oxidation Chemistry. Ph.D. Thesis, Drexel University, Philadelphia, PA.
56. R. H. Natelson, M. S. Kurman, N. P. Cernansky, D. L. Miller. (2011). Low Temperature Oxidation of n-Butylcyclohexane. *Combustion and Flame*, Vol. 158, No. 12, 2325-2337.
57. K. Schofield. (2008). The Enigmatic Mechanism of the Flame Ionization Detector: Its Overlooked Implications for Fossil Fuel Combustion Modeling. *Progress in Energy and Combustion Science*, Vol. 34, No. 3, 330-350.
58. M. S. Kurman, R. H. Natelson, N. P. Cernansky, D. L. Miller. (2011). Speciation of the Reaction Intermediates from n-Dodecane Oxidation in the Low Temperature Regime. *Proceedings of the Combustion Institute*, Vol. 33, No. 1, 159-166.
59. H. J. Curran, P. Gaffuri, W. J. Pitz, C. K. Westbrook. (1998). A Comprehensive Modeling Study of n-Heptane Oxidation. *Combustion and Flame*, Vol. 114, No. 1-2, 149-177.

60. C. K. Westbrook, W. J. Pitz, O. Herbinet, H. J. Curran, E. J. Silke. (2009). A Comprehensive Detailed Chemical Kinetic Reaction Mechanism for Combustion of n-Alkane Hydrocarbons from n-Octane to n-Hexadecane. *Combustion and Flame*, Vol. 156, No. 1, 181-199.
61. G. Bikas, N. Peters. (2001). Kinetic Modeling of n-Decane Combustion and Autoignition. *Combustion and Flame*, Vol. 126, No. 1-2, 1456-1475.
62. K. Brezinsky, F. L. Dryer. (1986). A Flow Reactor Study of the Oxidation of iso-Butylene and an iso-Butylene/n-Octane Mixture. *Combustion Science and Technology*, Vol. 45, No. 225.
63. E. J. Silke, H. J. Curran, J. M. Simmie. (2005). The Influence of Fuel structure on Combustion as Demonstrated by the Isomers of Heptane: a Rapid Compression Machine Study. *Proceedings of the Combustion Institute*, Vol. 30, 2639–2647.
64. A. Miyoshi. (2012). Molecular Size Dependent Falloff Rate Constants for the Recombination Reactions of Alkyl Radicals with O<sub>2</sub> and Implications for Simplified Kinetics of Alkylperoxy Radicals. *International Journal of Chemical Kinetics*, Vol. 44, No. 1, 59-74.
65. S. Sharma, S. Raman, W. H. Green. (2010). Intramolecular Hydrogen Migration in Alkylperoxy and Hydroperoxyalkylperoxy Radicals: Accurate Treatment of Hindered Rotors. *The Journal of Physical Chemistry A*, Vol. 114, No. 18, 5689-5701.
66. S. M. Villano, L. K. Huynh, H. H. Carstensen, A. M. Dean. (2011). High-Pressure Rate Rules for Alkyl + O<sub>2</sub> Reactions. 1. The Dissociation, Concerted Elimination, and Isomerization Channels of the Alkyl Peroxy Radical. *The Journal of Physical Chemistry A*, Vol. 115, No. 46, 13425-13442.
67. S. M. Villano, L. K. Huynh, H. H. Carstensen, A. M. Dean. (2012). High-Pressure Rate Rules for Alkyl + O<sub>2</sub> Reactions. 2. The Isomerization, Cyclic Ether Formation, and  $\beta$ -Scission Reactions of Hydroperoxy Alkyl Radicals. *The Journal of Physical Chemistry A*, Vol. 116, No. 21, 5068-5089.
68. M. Mehl, W. J. Pitz, C. K. Westbrook, H. J. Curran. (2011). Kinetic Modeling of Gasoline Surrogate Components and Mixtures Under Engine Conditions. *Proceedings of the Combustion Institute*, Vol. 33, No. 1, 193-200.
69. J. Bugler, K. P. Somers, E. J. Silke, H. J. Curran. (2015). Revisiting the Kinetics and Thermodynamics of the Low-Temperature Oxidation Pathways of Alkanes: A Case Study of the Three Pentane Isomers. *The Journal of Physical Chemistry A*, Vol. 119, No. 28, 7510-7527.

## **APPENDIX A: PFR FACILITY UPGRADES, MAINTENANCE, AND TROUBLESHOOTING**

Throughout the course of this research, several facility upgrades, replacement of parts, and repairs were performed. These upgrades, replacement of parts, and repairs are described for the GC/MS/FID, Ultramat 23 gas analyser, and the modeling computer in the following three sections. In the section that concerns the gas analyzer, i.e. in Appendix A.2., a modified calibration procedure is also included. In Appendix A.3, which mainly describes the upgrade of the modeling computer, several main encountered errors when setting up certain problems in CHEMKIN-PRO environment as well as their solutions are described.

### **Appendix A.1 MS Operating Parameters, GC Method Temperature Program, Maintenance and Replacement of Parts for the GC/MS/FID System and Associated Equipment**

Figure A-1 shows the MS operating parameters as indicated by a tune report generated in July 2015. The MS is operated under Electron Ionization mode. The shown tune report was generated a few hours after re-starting the MS, following a routine maintenance work. Consequently, the vacuum pressure was still high, around 79 mTorr. Given enough time after starting up the system, i.e. at least 5 hours, the vacuum pressure should stabilize at 25 – 30 mTorr. All other parameters on the tune report are at their desired values.

Table A-1 shows the temperature ramping profile used for both oxidation and pyrolysis studies. It also includes the carrier gas (i.e. helium) flow rate through the GC column.



**Table A- 1: GC temperature ramping profile and column carrier gas flow**

<b>Gas Chromatograph</b>	
Initial Temperature	-20 °C
Initial Time	5 min
Ramp 1 Rate	10 °C/min
Ramp 1 Temperature	120 °C
Ramp 1 Hold Time	0 min
Ramp 2 Rate	5 °C/min
Ramp 2 Temperature	225 °C
Ramp 2 Hold Time	0 min
Ramp 3 Rate	2 °C/min
Ramp 3 Temperature	245 °C
Ramp 3 Hold Time	0 min
Ramp 4 Rate	3 °C/min
Ramp 4 Temperature	270 °C
Ramp 4 Hold Time	0 min
Post Analysis Temp.	275 °C
Post Anal. Pressure	517 kPa
Post Analysis Time	10 min
Column Flow	1.7 mL/min

The routine maintenance procedures, e.g. cleaning the ion source assembly, are described in details in the service and operating manual for each unit. In addition to normal maintenance procedures, several problems were encountered that were not readily solved by contacting Thermo Scientific customer support line (1-800-532-4752). Resolving these issues required field service visits and in some occasions, replacement of some parts. Table A-2 provides a list of these encountered problems, the actions taken during the field service appointment, and the parts replaced.

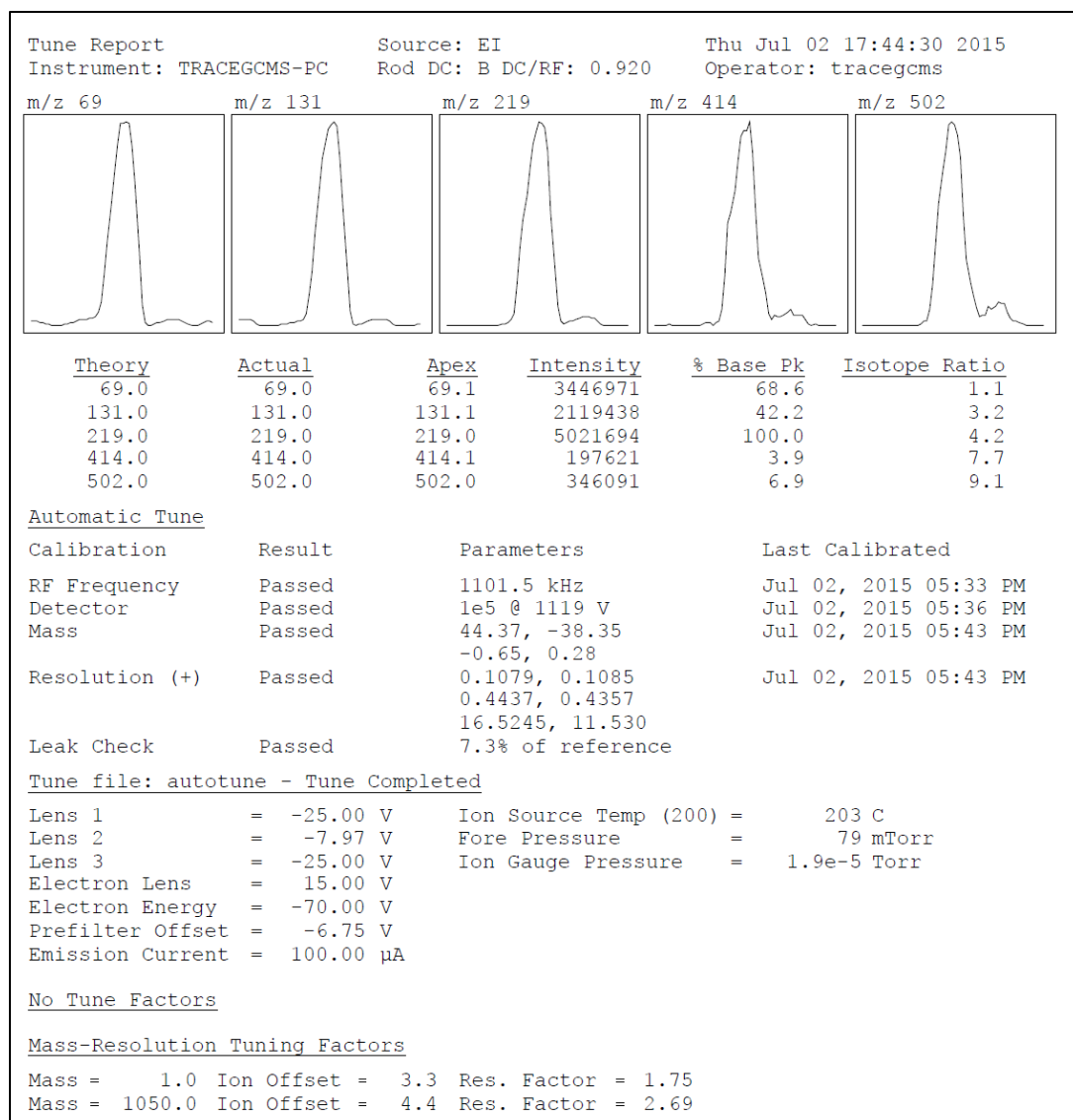


**Figure A- 1: MS operating parameters according to a sample tune report.**

**Table A- 2: GC/MS/FID field service visits from November 2010 to November 2015.**

<b>Problem Reported</b>	<b>Actions Taken by Field Service Representative (Dennis Beauchamp)</b>	<b>Parts Replaced</b>
<ul style="list-style-type: none"> <li>- System did not pass auto-tune after Xcalibur software upgrade</li> <li>- Electron multiplier (EM) voltage was near maximum</li> </ul>	<p><i>Service Date: 11/23/2010 – 11/28/2010</i></p> <ul style="list-style-type: none"> <li>- Cleaned ion source and pre-filter (Note: routine maintenance procedure, also performed on a regular basis).</li> <li>- Replaced filament and spacer.</li> <li>- Changed pump oil (also a routine task)</li> <li>- Installed a new EM.</li> <li>- Allowed system to pump overnight, then performed hardware resolution adjustments, full auto-tune was run.</li> <li>- EM voltage was set to 1150v.</li> <li>- All tests passed, all diagnostics passed, column bleed and noise was minimum.</li> </ul>	<ul style="list-style-type: none"> <li>- Insulator filament ion trap /DSQ (MN: 119650-0235, price: \$148.55).</li> <li>- Filament assembly ion trap (MN: 119701-60287, price: \$255.29).</li> <li>- Electron multiplier (used a brand-new item available in the lab).</li> </ul>
<ul style="list-style-type: none"> <li>- Extensive baseline noise on the MS spectra was observed. No peaks were detected during a GC/MS gas sample run.</li> <li>- Auto-tune failed.</li> </ul>	<p><i>Service Date: 09/02/2011</i></p> <ul style="list-style-type: none"> <li>- Re-aligned the ion source pre-filter in the baffle wall.</li> <li>- Wrong versions of Xcalibur were Installed (not related to the initially reported issue). Installed Xcalibur 1.4.</li> <li>- Performed hardware resolution, tuned and calibrated system. Issues resolved.</li> </ul>	N/A
<ul style="list-style-type: none"> <li>- MS did not have a signal</li> <li>- GC fan was noisy, indicating a failure.</li> <li>- The Xcalibur Software Crashed frequently.</li> </ul>	<p><i>Service Date: 10/25/2012 – 12/19/2012 (Several field service visits were required to address all the issues)</i></p> <ul style="list-style-type: none"> <li>- Found RF coil assembly and Rod Driver PS to be defective. Replaced both.</li> <li>- Replaced GC cooling fan.</li> <li>- Reloaded software tuned and calibrated.</li> <li>- System function restored.</li> </ul>	<ul style="list-style-type: none"> <li>- RF module DSQ assembly (MN: 119668-1000, price: \$3430.00)</li> <li>- Rod driver DSQ assembly (MN: 120152-1000, price: \$1340.00)</li> <li>- GC rear fan 230 V-24170-0016 (MN: 40600705, price: \$264.10)</li> </ul>
<ul style="list-style-type: none"> <li>- The GC/MS/FID system Was kept shutdown for months following relocation of PFR facility. The system was turned on in October 2014. All diagnostic tests passed. However, the ion gauge pressure and MS fore pressure were unstable and high.</li> </ul>	<p><i>Service Date: 12/04/2014</i></p> <ul style="list-style-type: none"> <li>- Found main fore line loose, cut back line and reattached.</li> <li>- Filled Fc43 (MS calibration fluid) vial and adjusted.</li> <li>- Still, system did not pump down. Recommended the installation of a new SGE restrictor set (see item 6 on page 121).</li> </ul>	N/A

In addition to the maintenance and repair activities that required a field service by a Thermo Fisher representative, activities were performed to maintain the proper and up-to-date and operation of the system and associated equipment. These activities included the upgrade of GC/MS/FID computer, the upgrade of the Xcalibur data system to a Windows 7 compatible version, the upgrade of NIST MS library, Replacement of the 4-port switching valve and repair of the 6-port switching inside of the GC auxiliary box, and replacement of the SGE column splitter restrictor set inside of the GC oven. The following provides a numbered list of these activities, organized by date:

1. A NIST 08 MS Library upgrade (Material NO: 120338-UPGR, price: \$980) was purchased in *October 2010*.
2. Following a failure, the vacuum pump for GC auxiliary box was replaced with an Edwards RV8 PFPE vacuum pump (ADVACO, price: \$3606.00) in *February 2011*.
3. The GC/MS/FID computer was replaced with a Dell OptiPlex 990 desktop (Dell, price: \$840.00) in *October 2011*. The computer has an Intel Core i3, 3.1 GHz Processor, 4 GB of RAM (Non-ECC,1333MHz DDR3,2X2GB), and a 500 GB Hard Drive (500GB SATA 6.0Gb/s and 16MB Data Burst Cache).
4. The operating software for the purchased Dell OptiPlex 990 computer was 32-bit windows 7, requiring an upgrade of Xcalibur data system, i.e. Xcalibur 2.1.0 (SP1/Foundation 1.0.2 SP2). The Xcalibur software upgrade was performed in *December 2011*. The proper operation of the DSQ (i.e. the mass spectrometer) also required the back up and transfer of auto-tune and DSQ registry files from the previous computer. This should always be done for a working DSQ because the calibration is stored in the registry. If a hard drive fails, a simple reload of Xcalibur

- may not be sufficient to get the DSQ working again. In an event that re-installation of Xcalibur software is required, attention must be given to ensure the re-storing of previous parameters such as instrument configuration settings, DC/RF gain value, EM gain voltage, and ion source temperature.
5. In *January 2015*, following the relocation of PFR lab and the restarting the GC/MS/FID, it was observed that the GC sample loop did not maintain a vacuum when needed. Following evaluations, it was determined that the 4-port switching valve inside of the GC auxiliary hot box (normally maintained at 215 °C) was defective. The micro-electronic actuator functioned properly. The 4-port valve (VICI, Part NO: DC4UWE, price: \$470.00, for use with the existing actuator) was replaced. The leak issue persisted and additional investigations determined that the ports 1 and 2 of the 6-port switching valve (also located inside of the GC auxiliary box) were defective and did not seal properly, even though new tubing and ferrules had been installed. The 6-port valve was sent to VICI, where it was inspected and the ports' failure was confirmed. VICI replaced the defective valve with a refurbished one at a fixed cost of \$165.00. Installation of the provided valve resolved the issue.
  6. During the field service visit by Dennis Beauchamp in December 2014 to address the high fore line pressure issue, it was determined a new SGE restrictor set had to be installed. The restrictor set is a part of GC column splitter assembly which is used to split the column flow between the FID and the MS. A new fused silica restrictor set for use with 0.25mm ID columns, denoted as the vendor by Restrictor Set A (Trajan Scientific Americas Inc., Part No: 123711, price: \$67.00), was purchased and installed in *April 2015*. In addition, the ferrules that connected the fused silica tubing

to the low dead volume tee were replaced (Trajan Scientific Americas Inc., Part No: 073224, price: \$64.00). This resolved the unstable fore line pressure issue.

## **Appendix A.2 Calibration and Replacement of Parts for the Ultramat 23 Gas Analyzer**

Prior to every PFR oxidation experiment, the Ultramat 23 gas analyzer is to be calibrated. The overall calibration procedure consists of two steps:

1. The autocal, i.e. zero-calibration of IR channels and spanning of O<sub>2</sub>
2. The IR channel calibration, i.e. zero-calibration of O<sub>2</sub> sensor and spanning of CO / CO<sub>2</sub>

For the autocal step, a certified Airgas mixture of 20.95% O<sub>2</sub> in N<sub>2</sub> is used. For calibration of CO and CO<sub>2</sub> channels (i.e. the IR channels), Airgas mixtures of 1000 ppm CO in N<sub>2</sub> and 1000 ppm CO<sub>2</sub> in N<sub>2</sub> are used. The calibration procedure for the gas analyzer was modified in 2011 following the recommendation of technical support at Siemens to optimize the accuracy of the readings. The following provides a step by step procedure. In general, every time that the analyzer is turned back on, the autocal step of the calibration procedure needs to be repeated. Although the calibration of IR channels can be performed less frequently according to the operating manual, it was decided that it would be performed together with the autocal process prior to each oxidation experiment, ensuring the accuracy of the readings within the detector uncertainties. The calibration procedure is to be performed after the initial 45 minute warm-up mode that automatically starts when the analyzer is turned on and during which, the analyzer will automatically go through two autocal processes. Once the initial 45 minute warm-up is passed, the analyzer should be manually calibrated by following the steps below:

1. Connect the 20.95% O<sub>2</sub> in N<sub>2</sub> to port #3. Make sure the pump is turned off.

2. Press CAL on analyzer and adjust air flow to 1.5 L/min by using the pressure regulator on the gas cylinder.
3. After about two minutes, the analyzer will automatically switch to port #1 and the pump turns on. During this part of the autocal process, ambient air will flow through the port. Note that port #1 is the measuring port to which the sample line connects during an experiment for measurements of CO, CO<sub>2</sub>, and O<sub>2</sub>.
4. Once the second part of autocal step is completed, connect one of the IR channel calibration bottles to port #1. Make sure the pump is turned off. Set the flow rate to ~ 1.5 L/min.
5. Follow the procedure in section 5.8.2.2 of the Ultramat 23 operating manual, page 5-22, to zero O<sub>2</sub> channel. Note: Level 1 code is 111 and level 2 code is 222.
6. While the bottle is still connected, calibrate the corresponding IR channel by following the procedure in section 5.8.1.2 on page 5-21.
7. Disconnect the line from port #1. Do not turn of the calibration bottle before closing the cylinder, as it may cause an excess pressure and subsequent blow-off of the filter cup and / or damage to the instrument.
8. Connect the other IR channel calibration bottle and repeat steps 6 and 7 for the channel corresponding to the connected bottle.
9. Calibration is complete. To make measurements, connect the sample line to port #1, make sure that the pump is turned off, and set the flow to ~ 1.5 L/min.

During the course of this research, two of the main parts of the gas analyzer were replaced. First, the electrochemical oxygen sensor (Siemens, MN: 1901067-001, price: \$770.00) was replaced once in *September 2010* and once in *July 2012*. The

electrochemical sensor is depletable based on the frequency of usage and the years in service. The only evidence of the need for replacement is generally a low reading of oxygen. A brand new oxygen sensor is currently available in the lab for possible future need. Second, the pump (Siemens, MN: 1901159-001, price: \$1,134.00) was replaced in *August 2015* following the failure of the original pump of the unit.

### **Appendix A.3 The Modeling Computer Upgrade and Troubleshooting of Several Common CHEMKIN-PRO Errors**

To increase the computing capabilities when implanting reactor models in CHEMKIN-PRO and analyzing the simulation results, a Dell Precision T3610 workstation was purchased in May 2014 (Dell, price: \$2744.79). The following are some of the key specification of the workstation:

1. Operating software: Windows 7 Professional, 64bit (includes Windows 8.1 Pro 64bit License and Media)
2. Processor: Intel Xeon Processor E5-1650 v 2 (Six Core HT, 3.5 GHz Turbo, 12 MB)
3. Hard Drive: a 2TB 3.5inch Serial ATA (7,200 Rpm) hard drive and 256 GB 2.5inch SATA Solid State Drive
4. Memory: 16GB (4x4GB) 1866MHz DDR3 ECC RDIMM

The CHEMKIN-PRO software can take up a large amount of Java memory, particularly when running projects with large and complex diagrams and parameter studies or when analyzing large mechanisms in the reaction path analyzer. The user may receive an error message indicating that the program has run out of Java memory. For java memory, the specified size has to be large enough to handle the needs, but at least 512 MB must be left for other processes and the operating system on the computer. The



java memory is assigned under an environment variable called CKJAVAMEMRY. The default value for Windows operating system is 1 GB. For the modeling workstation, the maximum memory is currently specified as 12 GB.

Another error that may be encountered with larger mechanisms is the following message:

“TASK INTERRUPTED: TROUBLE IN THE TRANSIENT SOLVER DDASPK”. This error was specifically encountered when trying to run sensitivity analysis for the LLNL 2011 mechanism for  $C_7 - C_{20}$  2-methylalkanes and  $C_8 - C_{16}$  *n*-alkanes with 7171 species and 31669 reactions. When a reaction mechanism is large enough and the sensitivity analysis is turned on, the number of equations solved for is larger than the value that can be represented by default “integer” type used by CHEMKIN-PRO. The default integer type will go to +/-2.1 billion (2,147,483,647). For the aforementioned mechanism, the number of needed integers to perform the sensitivity analysis was 2,274,222,750, over the default number for integer type. This does not mean that the problem cannot be solved. But an integer-type that supports bigger integers needs to be used. There is however, currently no permission for the CHEMKIN-PRO user to increase the default integer type. As mentioned in Chapter 5, to address this issue, a sub-mechanism of LLNL 2011 for *n*-alkanes and 2-methylalkanes up to *C12*, also available on LLNL website, was used.

## VITA

Farinaz Farid was born on September 3<sup>rd</sup>, 1987 in Tehran, Iran. Upon graduation from high school in 2004, she attended Eastern Mediterranean University in Cyprus and graduated in 2008 with a BSc degree in Mechanical Engineering. After graduation, she moved to United States and in 2009, she started her PhD studies at Drexel University. As a member of Combustion Chemistry group at Drexel University, she focused her research on oxidation and pyrolysis of large hydrocarbons. During her graduate studies, she also worked as a teaching assistant for several undergraduate courses and mentored undergraduate researchers. After completing her PhD studies, she plans to develop a career in industry.

